National Library
of Canada

Bibliothèque nationale
du Canada

Canadian Theses Service

Service des thèses canadiennes

Ottawa, Canada
K1A 0N4

## NOTICE

The quality of this microform is heavily dependent upon the quality of the original thesis submitted for microfilming. Every effort has been made to ensure the highest quality of reproduction possible.

If pages are missing, contact the university which granted the degree.

Some pages may have indistinct print especially if the original pages were typed with a poor typewriter ribbon or if the university sent us an inferior photocopy.

Reproduction in full or in part of this microform is governed by the Canadian Copyright Act, R.S.C. 1970, c. C-30, and subsequent amendments.

## AVIS

La qualité de cette microforme dépend grandement de la qualité de la thèse soumise au microfilmage. Nous avons tout fait pour assurer une qualité supérieure de reproduction.

S'il manque des pages, veuillez communiquer avec l'université qui a conféré le grade.

La qualité d'impression de certaines pages peut laisser à désirer, surtout si les pages originales ont été dactylographiées à l'aide d'un ruban usé ou si l'université nous a fait parvenir une photocopie de qualité inférieure.

La reproduction, même partielle, de cette microforme est soumise à la Loi canadienne sur le droit d'auteur, SRC 1970, c. C-30, et ses amendements subséquents.

NL-339 (r. 88/04) c

Canada

THE UNIVERSITY OF ALBERTA

# MULTIDIMENSIONAL SPECTRAL ANALYSIS OF THE ELECTROENCEPHALOGRAM

BY

R. B. PARANJAPE

A THESIS

SUBMITTED TO THE FACULTY OF GRADUATE STUDIES AND RESEARCH

IN PARTIAL FULFILLMENT OF THE REQUIREMENTS FOR THE DEGREE

OF DOCTOR OF PHILOSOPHY.

DEPARTMENT OF ELECTRICAL ENGINEERING.

EDMONTON, ALBERTA

SPRING 1990

National Library of Canada
Canadian Theses Service
Ottawa, Canada
K1A 0N4

Bibliothèque nationale du Canada
Service des thèses canadiennes

## NOTICE

The quality of this microform is heavily dependent upon the quality of the original thesis submitted for microfilming. Every effort has been made to ensure the highest quality of reproduction possible.

If pages are missing, contact the university which granted the degree.

Some pages may have indistinct print especially if the original pages were typed with a poor typewriter ribbon or if the university sent us an inferior photocopy.

Reproduction in full or in part of this microform is governed by the Canadian Copyright Act, R.S.C. 1970, c. C-30, and subsequent amendments.

## AVIS

La qualité de cette microforme dépend grandement de la qualité de la thèse soumise au microfilmage. Nous avons tout fait pour assurer une qualité supérieure de reproduction.

S'il manque des pages, veuillez communiquer avec l'université qui a conféré le grade.

La qualité d'impression de certaines pages peut laisser à désirer, surtout si les pages originales ont été dactylographiées à l'aide d'un ruban usé ou si l'université nous a fait parvenir une photocopie de qualité inférieure.

La reproduction, même partielle, de cette microforme est soumise à la Loi canadienne sur le droit d'auteur, SRC 1970, c. C-30, et ses amendements subséquents.

ISBN 0-315-60380-1

NL-339 (r. 88/04) c

Canada

UNIVERSITY OF ALBERTA

RELEASE FORM

|  |  |
|---|---|
| NAME OF AUTHOR: | R. B. PARANJAPE |
| TITLE OF THESIS: | MULTIDIMENSIONAL SPECTRAL ANALYSIS OF THE ELECTROENCEPHALOGRAM |
| DEGREE: | DOCTOR OF PHILOSOPHY |

YEAR THIS DEGREE GRANTED: 1990

Permission is hereby granted to THE UNIVERSITY OF ALBERTA LIBRARY to reproduce single copies of this thesis and to lend or sell such copies for private, scholarly or scientific research purposes only.

The author reserves other publication rights, and neither the thesis nor extensive extracts from it may be printed or otherwise reproduced without the author's written permission.

Raman Paranjape

8907-120 st., Edmonton,
Alberta, Canada. T6G 1X6

Date: 20 Nov. 1989

THE UNIVERSITY OF ALBERTA

FACULTY OF GRADUATE STUDIES AND RESEARCH

The undersigned certify that they have read, and recommend to the Faculty of Graduate Studies and Research for acceptance, a thesis entitled MULTIDIMENSIONAL SPECTRAL ANALYSIS OF THE ELECTROENCEPHALOGRAM submitted by R. B. PARANJAPE in partial fulfillment of the requirements for the degree of DOCTOR OF PHILOSOPHY.

Z. J. Koles
.....................................................
(supervisor) Z.J. Koles

E. J. Shwedyk
.....................................................
E. Shwedyk

R. E. Rink
.....................................................
R.E. Rink

.....................................................
J. Kingma

H. Richard Hooper
.....................................................
H.R. Hooper

.....................................................

Date: 20 Nov. 1989.

# Abstract

This thesis investigates the hypothesis that specific brain states can be identified from spatial patterns on EEG topographic maps. Preliminary work showed that topographic maps of rms EEG data are representative of the actual potential distribution on the scalp and that errors in maps are not significantly affected by the method of interpolation used in their construction. Spatial patterns on the maps were subsequently investigated using spectral analysis. With simulated EEG data, results indicated that maximum entropy (ME) power spectrum estimates (PSEs) are consistently superior to Bartlett and Blackman-Tukey PSEs in terms of error in peak-position and the minimum separation in frequency required to identify two sinusoids. The ME PS analysis of sinusoids in white noise showed that acceptable PSEs could be obtained if the SNR was ≥0 dB. PS analysis of actual EEG data demonstrated that the energy of spatial waves was generally larger in EC (eyes closed) data than in EO (eyes open) data. The mean energy of sagittal waves ( wavelength 18.67 cm) was significantly larger ($p < 0.01$) in EC data than in EO data. The mean value of the entropy was significantly larger ($p < 0.01$) for EO PSEs than for EC PSEs indicating greater uniformity in EO PSEs. Discriminant analysis was used to classify features from EC and EO PSEs. The classification rule correctly identified 91% of PSEs in training data and 96% of PSEs in test data indicating that a stable classification rule was obtained. Analysis of normalized PSEs features (total power in PSE a constant) indicated that EC maps primarily contained waves along the sagittal line while EO maps contained waves in all directions. The discriminant analysis of normalized PSEs correctly classified 86% of PSEs in training data and 92% of PSEs in test data. This work demonstrates that spatial patterns on EEG topographic map can be used to identify specific brain states. It suggests that changes in cerebral organization associated with the EC and EO states are manifested in spatial patterns on EEG topographic maps.

# ACKNOWLEDGEMENTS

I thank my supervisor, Dr. Z.J. Koles, for his support throughout this project.

I thank Bob Morse and Honey Chan for advice and guidance. There are few people in this world for whom I have greater respect or admiration.

I thank my fellow students in Applied Sciences in Medicine – Bob Arthur, David D'Amico, Karim Damji, Abdulhakim Kasmia, Mike Lazar, Satyapal Rathee and Anthony Soong – for many stimulating discussions.

I thank all the staff in Applied Sciences in Medicine. In particular, I thank Ion Buicliu, Bob Heath and Narc Ouellete for help in data collection and in data processing.

I thank Dr. John Lind and Dr. Brendan McLean for their advice in the writing of this thesis.

Finally, I thank my family, my father, my mother, my sister and my brother for the confidence they have shown in me.

I acknowledge the financial support of the Alberta Heritage Foundation for Medical Research in the form of a studentship and research allowance.

## Table of Contents

Chapter 1

The Electroencephalogram ........ 1
1.0 Introduction ........ 1
1.1 The Biological Basis of the EEG ........ 3
1.2 Preliminaries to Spatial Processing of the EEG ........ 6
1.3 Topographical Analysis of the EEG ........ 8

Chapter 2

Topographic Mapping of the Electroencephalogram ........ 11
2.0 Introduction ........ 11
2.1 The Projection of Electric Potentials from the Scalp ........ 11
2.2 Interpolation Methods ........ 13
2.3 A Pilot-Study ........ 21
2.3.1 Methods ........ 21
2.3.2 Results ........ 25
2.3.2.1 Analysis of Instantaneous EEG Data ........ 31
2.3.2.2 Analysis of rms EEG Data ........ 32
2.3.4 Conclusions ........ 36

Chapter 3

Power Spectrum Estimation ........ 37
3.0 Introduction ........ 37
3.1 Time Series ........ 37
3.2 The Autocorrelation Function ........ 38
3.3 Power Spectrum Estimation ........ 39
3.3.1 Classical Methods ........ 40
3.4 Modern Methods of Power Spectrum Estimation ........ 46
3.5 AR Parameter Estimation - The Wiener Filter and the Prediction-error Filter ........ 51
3.5.1 Wiener Filtering ........ 51
3.5.2 The Prediction-error Filter ........ 55
3.6 Maximum Entropy Spectrum Estimation ........ 58
3.7 Equivalence of the Prediction-error and Maximum Entropy Power Spectrum Estimates ........ 64
3.8 A Description of the Lim and Malik Algorithm for Two dimensional Maximum Entropy Power Spectrum Estimation ........ 68
3.9 Statistical Properties ........ 82
3.10 Conclusions ........ 82

Chapter 4

Bartlett, Blackman-Tukey and Maximum Entropy Power Spectrum Estimates of Simulated Data ........ 84
4.0 Introduction ........ 84
4.1 Methods ........ 84
4.2 Results ........ 86
4.2.1 BA, BT and ME PSEs ........ 86
4.2.2 Effects of Frequency ........ 92
4.2.3 Identification of Two Sinusoids ........ 95
4.2.4 ME PSEs of Data with Noise ........ 97
4.3 Conclusions ........ 100

Chapter 5

Spatial Spectral Analysis of the EEG ........ 101
- 5.0 Introduction ........ 101
- 5.1 Methods ........ 101
  - 5.1.1 Recording Conditions ........ 101
  - 5.1.2 Signal Processing and Topographic Mapping ........ 104
  - 5.1.3 Maximum Entropy Spectral Estimation ........ 107
  - 5.1.4 Data Reduction ........ 111
  - 5.1.5 Methods of Data Analysis ........ 113
    - 5.1.5.1 Overview of Discriminant Analysis ........ 113
  - 5.1.6 Summary ........ 114
- 5.2 Results ........ 115
  - 5.2.1 PSEs of Topographic Maps ........ 115
  - 5.2.2 Comparison of Feature Means ........ 119
  - 5.2.3 Correlation Analysis ........ 121
  - 5.2.4 Discriminant Analysis ........ 123
    - 5.2.4.1 Discriminant Analysis of PSEs ........ 123
    - 5.2.4.2 Discriminant Analysis of Normalized PSEs ........ 127
- 5.3 Discussion and Conclusions ........ 130

Chapter 6

Discussion and Conclusions ........ 132
- 6.1 Discussion ........ 132
- 6.2 Further Investigations ........ 137
- 6.3 Some Observations on Topographic Mapping ........ 139
- 6.4 Conclusions and Limitations ........ 140

References ........ 142

APPENDIX 'A' ........ 147

APPENDIX 'B' ........ 151

# List of Tables

Table page

2.1 Parameters of instantaneous EEG maps .......... 34
2.2 Parameters of rms EEG maps .......... 35

3.1 Symbols used in Lim and Malik Algorithm .......... 72

4.1 Comparison of BA, BT and ME PSEs (one sinusoid) .......... 93
4.2 Comparison of BA, BT and ME PSEs (two sinusoids) .......... 96
4.3 ME PSEs of sinusoids and noise .......... 99

5.1 31 Electrode system .......... 103
5.2 Equivalent waves .......... 113
5.3 Comparisons of PSE features .......... 120
5.4 Comparisons of normalized PSE features .......... 120
5.5 Correlations of PSE features .......... 122
5.6 Correlations of normalized PSE features .......... 122
5.7 Discriminant analysis of PSE features .......... 125
5.8 Standardized coefficients of PSE features .......... 125
5.9 Discriminant analysis of normalized PSE features .......... 128
5.10 Standardized coefficients of normalized PSE features .......... 128

# List of Figures

Figure page

1.1 Typical nerve cell ..... 5

2.1 International 10-20 System ..... 14
2.2 Triangle interpolation (wireframe) ..... 18
2.3 Bilinear interpolation (wireframe) ..... 19
2.4. Bicubic Spline interpolation (wireframe) ..... 20
2.5 International 10-20 System and test electrodes ..... 23
2.6 Actual and interpolated EEG ..... 27
2.7 Regression of actual and interpolated EEG ..... 28
2.8 Error in interpolated EEG ..... 29
2.9 Error in interpolated EEG ..... 30

3.1 Flowchart of Lim and Malik Algorithm ..... 63
3.2 Detailed flowchart of Lim and Malik Algorithm ..... 73

4.1 Greylevel view of BA, BT and ME PSEs ..... 88
4.2 Wireframe view of BA PSEs ..... 89
4.3 Wireframe view of BT PSEs ..... 90
4.4 Wireframe view of ME PSEs ..... 91
4.5 Special regions of PSEs ..... 94

5.1 31 Electrode system ..... 102
5.2 Mercator projection of 31 Electrode system ..... 106
5.3 Resampled sited on topographic maps ..... 108
5.4 Normalized ACF error ..... 110
5.5 Regions of the PSEs ..... 112
5.6 Topographic maps of rms EEG ..... 116
5.7 Wireframe PSE of rms EEG ..... 117
5.8 Greylevel PSE of rms EEG ..... 118
5.9 Topographic maps of PSE features ..... 126
5.10 Topographic maps of normalized PSE features ..... 129

B.1 Non-linear mapping of ME method ..... 154

# Chapter 1

# The Electroencephalogram

## 1.0 Introduction

The human brain is one of the most complex systems known to man. The functioning brain normally develops low-amplitude electrical signals that are measurable on the scalp. A record of these signals is called the electroencephalogram (EEG) and the study of these signals has developed into the neurophysiological speciality known as electroencephalography.

The analysis of the EEG is of great importance in the study of both information processing in the brain and brain pathology. Attempts have been made to correlate EEG patterns to various mental tasks such as solving arithmetic problems (Vogel *et al.*, 1968), auditory and visual discrimination (Walter *et al.*, 1967), reading and writing (Gevins *et al.*, 1979), meditation (Doyle *et al.*, 1974), etc. To date however, no clear understanding of the relationship between the EEG and these higher brain functions has developed. In the study of brain pathology, on the other hand, significant progress has been made. The EEG is now used to follow various brain disorders such as epilepsy (Gibbs *et al.*, 1935), vascular disease (Remond, 1972a), mental retardation (Remond, 1972b), brain damage and stroke (Kooi, 1971). It is used in locating brain tumors (Walter, 1936), for determining brain death (Harvard Committee on Brain Death, 1968), for determining the depth of anaesthesia in surgery (Clark and Rosner, 1973) and in psychiatry to study behavioral disorders (Gibbs and Gibbs, 1964).

The EEG is traditionally presented as a set of traces of voltage versus time on a strip chart. As a result, its analysis has primarily focused on temporal patterns in these traces. For example, correlations between power in the alpha band (8 to 13 Hz) and subjects in a relaxed, resting-state have been established (Berger, 1929). Drugs such as halothane have been shown to induce almost purely sinusoidal oscillations (Nunez, 1981) and the EEG of epileptic patients in seizure has been described as a series of spike or spike-dome waves (Gibbs *et al.*, 1935).

Recent interest in the neurophysiological community has focused on the spatial distribution of the EEG. It is believed that if an accurate and precise representation of the potential distribution on the scalp is available, a clearer assessment of correlations both between regions of the scalp and also between anatomy and electrical activity is possible. The potential distribution on the scalp may be represented by a topographic map constructed by projecting a number of scalp potentials onto a flat plane and then interpolating between the projected potentials.

Topographic mapping has provided a new tool for the analysis of the EEG, however, its utility is still controversial (Duffy, 1986). While topographic mapping of the EEG provides a qualitative picture of the gross spatial distribution of scalp potentials, there are a number of practical limitations to its use. For example, topographic maps are inherently an inefficient means of communicating data since only a few points in a topographic map are actual recorded data, the remainder of the map being produced through interpolation. Another limitation with topographic mapping is that quantitative information about the spatial distribution is not directly available. It is difficult to make anything other than a superficial comparison of recorded data when using topographic maps. Finally, it is necessary to observe hundreds, perhaps thousands, of topographic maps and it is difficult to recognize patterns in this number of images.

A more fundamental description of the potential distribution may be obtained through a spatial spectral analysis of the topographic maps where spatial signals on the map are decomposed into sinusoidal waves. Spectral analysis of spatially distributed data is carried out in a number of disciplines, such as for example geophysics and radio astronomy where spectral analysis is used to describe, characterize and summarize data.

The spatial spectral analysis of the EEG has several advantages. (1) It is a means of describing the spatial distribution in terms of spatial waves on the scalp. (2) It provides a method for characterization and representation of the distribution in terms of a small number of waves. (3) Quantitative parameters such as spatial frequency and energy density are provided. (4) The effect of an active reference electrode is confined to only one spatial frequency and the remainder of the spectrum is independent of the reference.

This thesis is a quantitative examination of the potential distribution on the scalp. The analysis is based on topographic maps. The relationship between the actual potential distribution and topographic maps is first investigated. It is shown that maps can be considered as representative of the actual potential distribution. It is proposed that spatial spectral estimation provides a useful tool for the identification of patterns in topographic maps that are unique to, or indicative of the brain state of subjects. Various methods of spectral analysis (periodogram, Blackman-Tukey, autoregressive, maximum entropy, moving average, autoregressive-moving average) are therefore studied. The maximum entropy (ME) method is shown to be most appropriate for the spectral analysis of topographic maps. To further investigate this approach, spectral estimates of the topographic maps from a population of normal volunteers are analyzed. Various analyses are performed with features from the spectral estimates to determine if statistically significant variations between brain states are observed.

A summary of the biological basis of the EEG is first presented. Some preliminaries to spatial processing of brain potentials are then discussed followed by a review of recent advances in EEG analysis through the use of topographic maps.

## 1.1 The Biological Basis of the EEG

The human brain is primarily composed of a large number of nerve cells (called neurons). Two features that distinguish neurons from other cells in the body are: (1) their extraordinary physical shape, and (2) their capability to transmit and receive electrical signals through fluctuations in membrane potential (Alberts *et al.*, p. 1015, 1983). Figure 1.1 presents a schematic diagram of a neuron. Three major parts of the neuron are distinguishable: the cell body, the dendritic branches and the axon. The cell body is the metabolic center of the neuron and contains the cell nucleus. The dendritic branches are typically extensions from the cell body which facilitate the reception of signals from other nerve cells through intercellular junctions called synapses. The largest process extending from the cell body is the axon which conducts signals away from the cell body to other nerve cells. The axon commonly divides at its distal end and makes thousands of synaptic connections with the cell bodies and dendrites of other nerve cells.

The resting neuron normally maintains a constant potential across its membrane. However neurons are rarely at rest and the membrane potential over the cell body and dendrites is altered continuously by synaptic signals of other nerve cells (called pre-synaptic neurons). A pre-synaptic neuron can depolarize or hyperpolarize the membrane of a post-synaptic neuron momentarily. Depolarizations to a threshold level causes an impulse, called an action potential, to propagate down the axon which in turn alters the potential of other synaptically connected neurons.

The human brain may be anatomically divided into a number of structures such as the cerebrum, the cerebellum, the brainstem etc. The cerebrum, the largest of these structures, forms the top-most portion of the brain. The cerebrum in turn is divided into two major regions. The outer 3 to 5 millimeters of the cerebrum, called the cerebral cortex or the grey matter, is composed of mostly dendritic branches and nerve cell bodies. The majority of the neurons (70%) in the cerebral cortex are pyramidal cells, so called because of their peculiar cell body shape (Katznelson, 1981, p. 403). The pyramidal cells are organized into parallel configurations of vertical columnar units in which the electrical activity is highly correlated. Below the grey matter is the second major region of the cerebrum, the white matter. The pyramidal cells of the grey matter usually project axons into the white matter. The axons extend through the white matter to functionally associated regions of the grey matter.

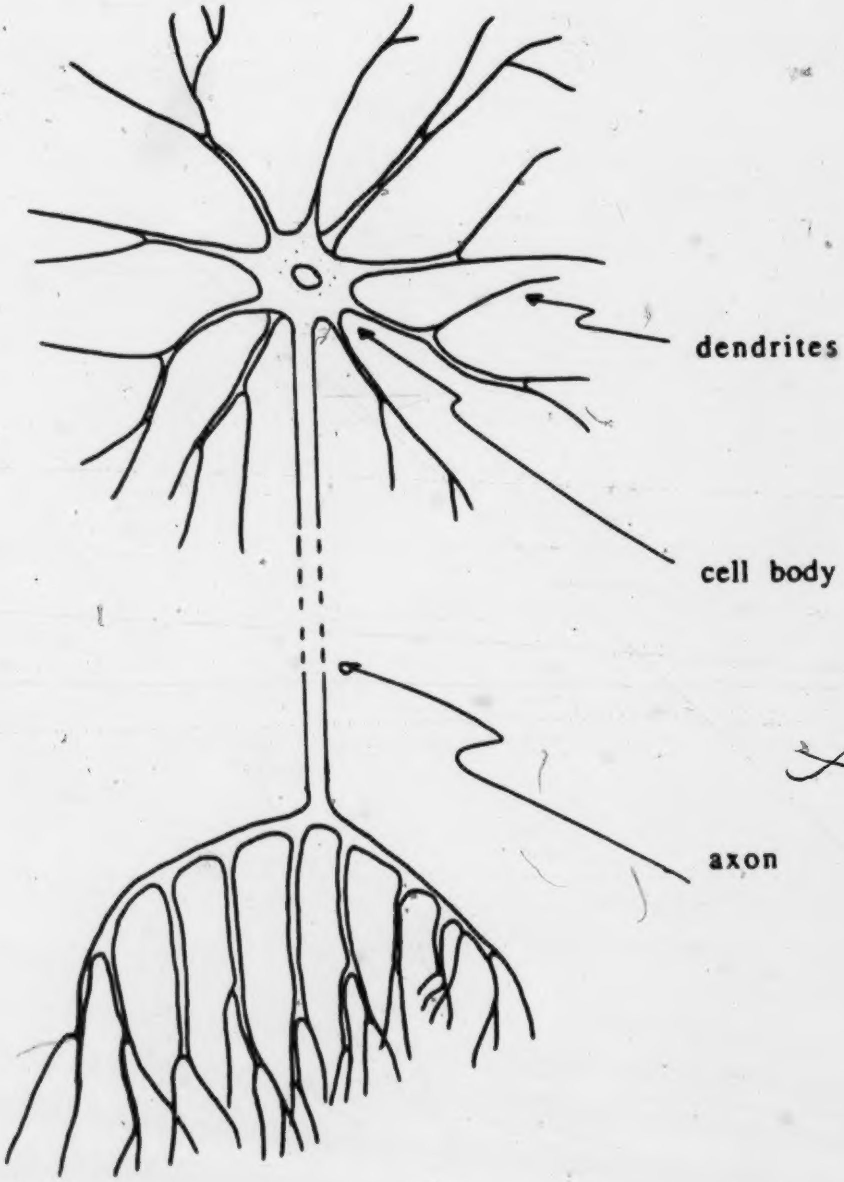
dendrites
cell body
axon

Figure 1.1 A schematic diagram of a typical nerve cell. The dendrites, body and axon of the nerve cell are indicated.

The post-synaptic potential that is developed over the cell body of the pyramidal cell may be approximated by a dipole. As these cells are arranged in a parallel configuration, the potential distribution over regions of electrically correlated pyramidal cells can be modelled as a dipole sheet. It is currently postulated (Gevins and Schafer, 1980; Gloor, 1985) that the electric signals (EEG) that are observed on the scalp may be attributed to the electrical activity of these correlated pyramidal cells.

### 1.2 Preliminaries to Spatial Processing of the EEG

Three major issues must be addressed before considering spatial processing of the EEG. They are: (1) spatial sampling, (2) interpolation and (3) recording reference. Each of these issues is now discussed briefly.

(1) Spatial sampling

In the analysis of the spatial distribution of the EEG it is assumed that a smooth and continuous function of the spatial coordinates on the scalp may be used to describe the surface potential. This interpolating function is adequately described by a discrete number of recorded potentials if the spatial variation of the function is within certain well defined limits. These limits define the highest spatial frequency that may be present in the interpolation function (Dudgeon and Mersereau, 1984). Thus the recording electrode density introduces an upper limit on the spatial frequency that can be detected. There is some controversy about the density of the sampling electrodes required in order to analyze the spatial distribution of the EEG. It has been suggested (Gevins, 1984) that for the human head, the point spread function of a generator on the surface of the cerebral cortex is about 2.5 $cm^2$ so that more than 250 sample sites (electrodes) are required to cover an average-sized head (radius 10 cm). The question remains whether EEG sources are in fact point sources or more extensive dipole sheets. Far fewer recording electrodes (16 to 32) are used in most topographic mapping systems that are available today. However the issue of adequate sampling is presently not resolved and is investigated further in this work.

(2) Interpolation

Some form of interpolation must be used if a continuous distribution of the surface potential is to be retrieved from samples recorded by an electrode montage on the scalp. This issue is fundamentally linked to the issue of electrode sampling density. If the electrode density is adequate, then in theory at least, the surface is completely recoverable by use of the ideal interpolating function. However, in practice, the application of this method on a finite extent data grid is not satisfactory. Other interpolation methods that are often used are not affected as much by boundary conditions. Examples of such methods are: bilinear (Naitoh and Walter, 1969), triangular (Duffy, 1982), bicubic-spline (Paranjape and Koles, 1986) and natural splines (Perrin *et al.*, 1986).

(3) Recording reference

The variation of potential at any test point on the scalp is by definition relative to some reference point and the actual potential that is recorded depends equally on the electrical activity at the reference and at the test point. It is commonly assumed that the reference point is far away from all electrical sources so that the potential recorded is indicative of only the sources near the test point. However, because of limitations imposed by the instrumentation, in a recording of the EEG the reference point must be taken on the body. It has been shown that it is not possible to find an inactive reference point on the body since proof of inactivity requires the existence of yet another inactive site (Nunez, 1981, p. 23; Lehmann, 1987, p. 313). This problem can be emphasized further by considering N electrodes attached to the body. For each electrode, N-1 different voltages can be measured. Therefore Nx(N-1) different voltage-polarity combinations may be recorded at any one moment in time.

The potentials that are recorded in the EEG include the activity of the reference point. Most often the reference point is taken on the ears or nose although these locations have been criticized because they are over holes in the skull and hence regions where electric current flow will tend to be focused (Nunez, 1981, p. 24).

Presently EEG data is recorded using either a bipolar or unipolar electrode format. In the bipolar format, electrodes are paired and the potential differences between various locations on the scalp are recorded. Since neither electrode is assumed to be a reference, this approach circumvents the difficulty of finding an inactive reference site on the body.

In the unipolar format a single electrode is used as the common reference for all other recording electrodes and therefore all recorded potentials have a contribution from the same reference. A simple procedure can be used to remove the effect of this reference if it is assumed that the total charge on the scalp is always zero. It has been suggested that the average value of the potentials recorded on the scalp at one instant in time be used as an estimate of the potential at the reference point (Lehmann, 1987). If this spatial average is subtracted from the recorded potentials, a reference independent measure of the potential distribution is made. This approach is adopted in this thesis.

### 1.3 Topographical Analysis of the EEG

Topographic displays of the potential distribution on the scalp were first attempted by Walter and Shipton in 1951. However, it was not until 1971 when Lehmann mapped the distribution of alpha activity that real interest in EEG topography developed. In 1978 Duffy produced the first commercially available topographic mapping system called the BEAM (for Brain Electrical Activity Mapping) system. Recent advances in topographic mapping systems have been primarily related to hardware, with increased flexibility in the types of maps that can be constructed and the storage of large volumes of EEG data.

Topographic mapping is now available in many EEG laboratories and analysis using these systems has been directed towards study of both brain function and brain pathology. The functional state of the brain determines how information received by the brain is processed. The functional state is constrained by several gross factors such as maturation, wakefulness, disease, etc. (Koukkou *et al.*, 1980; Katadou *et al.*, 1981), however, within these constraints the functional state is always changing and readjusting over short intervals. These short-term fluctuations, called micro-states, are thought to be observable in topographic maps (Lehmann *et al.*, 1987). Lehmann *et al.*, through an assessment of maps on the basis of location of maxima and minima (1971), 'hilliness' (1980), global field power (1986), and global dissimilarity criterion (1987) have attempted to identify these micro-states.

Lehmann *et al.* (1987) have also described the general characteristics of EEG topographic maps for subjects in a resting state. Maps generally contain a single area of maximal value and a single area of minimal value. The potential distribution between the extrema usually appears as lines of isopotentials. Characteristically, maps tend to be stable in one distribution for a short period (about 10 msec) and then make jump-like changes to a different configuration.

In a recent set of review papers Nuwar (1988a, b) showed that quantitative EEG analysis based on frequency analysis and topographic mapping of scalp potentials is useful in the detection and identification of various brain disorders. Patients with cerebrovascular disease have, for example, been observed to have abnormality in over 80% of cases in topographic analysis after being read as normal in routine visual assessments of EEG traces (Jonkman *et al.*, 1985).

Topographic methods have been used to describe the phenomenology of 'spike activity' in the assessment of epilepsy. For example, the bi-frontal spike wave phenomenon of generalized epilepsy has a negative spike component that begins and is most prominent over the anterior regions of the head (Harris and Bickford, 1968; Takahashi *et al*. 1985). The succeeding slow wave, in contrast, may begin in either the frontal or posterior scalp regions (Lehmann, 1972; Rodin and Acheta, 1986). Wong *et al.*, (1986) studied Rolandic spikes in children with benign Rolandic epilepsy. Significant differences were observed in topographic distributions of spike activity in subjects classified as having either typical or atypical clinical features suggesting that the spread in electrical activity can also be used to differentiate between groups.

The electrical activity associated with mass lesion and brain tumor is observable from topographic maps (Nuwar, 1988b). The scalp field gradients on the maps from focal spikes can be helpful in differentiating between superficial and deep sources (Matsua and Gastin, 1986). Slow waves have been used for localization of deep, white-matter tumors (Pier *et al.*, 1986).

While topographic mapping clearly has a use in the clinical setting, results are not always consistent. Clear-cut diagnosis based on topographic mapping alone are not possible at present and further work is required in order to fully determine the benefits and the limitations of this methodology.

# Chapter 2

# Topographic Mapping of the Electroencephalogram

## 2.0 Introduction

This chapter discusses various methods for constructing EEG topographic maps. In order to construct EEG topographic maps, electric potentials measured on the scalp must first be projected onto a flat plane and then interpolated to form a continuous surface.

In this chapter the Mercator method of projection is discussed first. Three common methods of interpolation that may be used to construct topographic maps are then reviewed. Finally, a pilot study is presented in which the relationship between topographic maps and the actual distribution of potential is assessed when using various types of EEG data.

## 2.1 The Projection of Electric Potentials from the Scalp

Topographic maps are constructed from electric potentials projected onto a flat surface. Regardless of the method of projection that is employed, it is impossible to construct these topographic maps and maintain all of the geometrical relationships that exist on the scalp (such as: duplication of angles, areas, distances, and directions). This difficulty is similar to that faced by cartographers when projecting from the earth onto a flat map.

In cartography, a projection is defined as an orderly system of transforming parallel and meridian lines, into which a spherical surface can naturally be divided, onto a map. Projections are usually classified as cylindrical, conical or azimuthal according to their derivation as geometrical projections from a sphere onto a cylinder, a cone or a plane respectively (Raisz, 1948).

The Mercator method of projection is classified as a cylindrical projection. It has a number of attributes that make it useful when projecting potentials from the scalp onto a flat topographic map. The Mercator projection is conformal, this means that the relationship between length on the map and length on the scalp is the same in all directions at each point on the map. This results in the important property that directions on the spherical surface are maintained after transformation onto a Mercator map.

In Mercator mapping, parallels are projected as horizontal lines and meridians as vertical lines. The meridians are placed on the Mercator map so that their spacing is true to scale at the equator of the sphere. The parallels are then spaced so that the scale on the meridians and on the parallels is the same at each point. The parallels on a sphere however, are shorter near the poles than near the equator, that is, their length is proportional to the cosine of the angle ($\phi$) between the parallel and the equator (where $\phi=0°$ at the equator and $\phi=\pm 90°$ at the poles). Because all the parallels are shown with equal length on a Mercator map, the scale of the parallels is increased by $1/\cos(\phi)$. In order to maintain this scale on the meridians, the scale of the meridians is also increased by $1/\cos(\phi)$. This results in the space between parallels increasing on the Mercator map as $\phi$ approaches 90°.

A difficulty with Mercator mapping is that as $\phi$ approaches ±90° the size of objects becomes large. It is in fact not possible to include a object located on either pole in a Mercator map.

The Mercator method of projection was adopted in this thesis over other methods of projection because it has the very useful property of preserving orientation over the transformation. This means that the shape of the distribution of electrical activity is preserved after transformation (for example a square region on a sphere will remain in the form of a square on a Mercator map). In addition, because EEG activity is sometimes characterized by orientation (for example left-right asymmetry) it is useful to maintain angles through the transformation. The difficulty of distortion of size that occurs in the regions near the poles is avoided by not projecting to the topographic map from these regions.

When using the Mercator method of projection to transform potentials from the scalp onto a flat plane it is assumed that the geometrical shape of the scalp can be approximated by a hemisphere. In addition, it is convenient if the potentials on the scalp are recorded at points that fall on a set of meridian and parallel lines. In the EEG electrode montage that was used for the work of this chapter (International 10-20 System) this was approximately true. By assigning pole locations to the nasion (forehead) and the inion (back of the head), electrode locations fall upon 5 meridian lines at parallels ($\phi$) of 72°, 36°, 0°, -36°, -72° with an average electrode placement error of 2.08% and a maximum electrode placement error of 9.38%.

The electrode locations of the 10-20 system are presented in figure 2.1 in an azimuthal projection. The azimuthal projection does not preserve scale or direction but it is helpful in visualizing the position of the electrodes on the scalp because landmarks such as the nose and ears can be included.

### 2.2 Interpolation Methods

After projecting measured potentials onto a flat plane, topographic maps of the EEG are constructed. There are a number of interpolation techniques that may be used to construct the topographic maps. Three methods of interpolation are discussed in this section: triangular, bilinear, and bicubic-spline respectively.

The triangular method of interpolation is the most commonly used in topographic mapping (Duffy, 1978). The topographic map is partitioned into triangular regions with recording electrodes at the corners of each triangular region. The potential within each region is then interpolated as a linear combination of the potential at the corner electrodes scaled by the distance to each electrode. The potential, V, at any off-electrode site is determined by the equation for a plane.

a

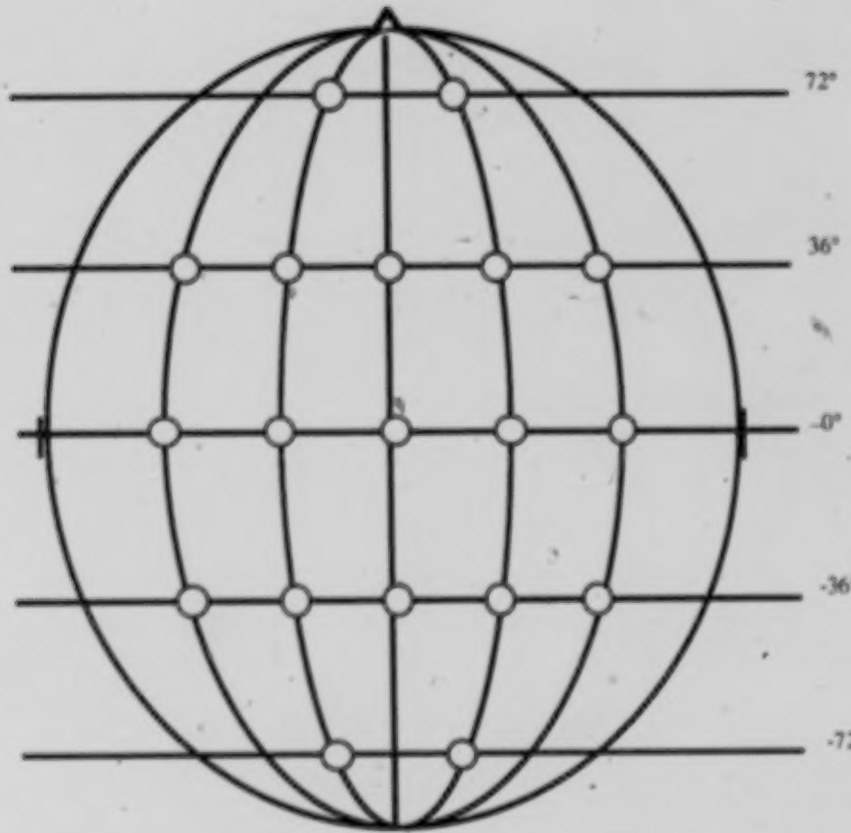

Figure 2.1 Stylized diagram of the International 10-20 Electrode System. The head is projected as a circle onto a plane with the nose and the ears indicated. Electrode sites are indicated by small rings on meridian and parallel lines.

(2.2:1)

$$V(x, y) = a(x-x_i) + b(y-y_j) + c$$

where

$x, y$ are orthogonal spatial variables on the map,

$i, j$ are used to identify a triangular region on the map,

$x_i, y_j$ identify the origin of the triangular region $i, j$,

$V$ is the potential at $(x, y)$ on the map.

The coefficients a, b, c are determined by solving a system of equations using the values of x, y and V at the 3 corner electrode sites.

A triangularly interpolated topographic map is continuous but is not smooth. In the view of many researchers however: "there is little evidence from classic EEG to suggest that electrodes more distant than the nearest 3 known points have additional influence upon intermediate locations." (Duffy, 1978).

In contrast, the bilinear method of interpolation is applied over a set of rectangular regions on the topographic map. The potential inside the rectangular region is estimated as the linear combination of the potential at the four corners of the region. The potential V(x, y) is defined as:

(2.2:2)

$$V(x, y) = \sum_{m,n=1}^{2} a_{ijmn} (x-x_i)^{m-1} (y-y_j)^{n-1}$$

where

$a_{ijmn}$ are coefficients determined by continuity conditions,

$i, j$ are used to identify a rectangular region on the map,

$x_i, y_j$ identify the origin of the rectangular region $i, j$.

For each rectangular region (i, j) there are 4 coefficients ($a_{m,n}$) which must be determined. They are determined by solving the system of equations formed by applying equation (2.2:2) at each of four corner electrode sites of the rectangular region.

The bicubic-spline method of interpolation, the last method of interpolation to be presented in this chapter, has not been extensively used in topographic mapping. It is applied over a set of rectangular regions of the topographic map. The potential V(x, y) in these rectangular regions is determined with a set of bicubic interpolating polynomials. The form of each polynomial is:

(2.2:3)

$$V(x, y) = \sum_{m,\, n=1}^{4} a_{i\,j\,m\,n}\, (x-x_i)^{m-1}\, (y-y_j)^{n-1}$$

There are 16 coefficients ($a_{m,\,n}$) that must be determined for each rectangular region (i, j). By application of the following continuity conditions at the 4 corners of each rectangular region these coefficients are determined: continuity of — (1) magnitude, (2) first partial derivative in x and y, (3) second partial derivative in x and y, and (4) cross partial derivative in both x and y. In addition, determination of the bicubic-spline surface requires assumptions to be made about the surface at the boundaries. For example, it may be assumed that the slope of the surface in the direction perpendicular to the boundary is zero everywhere and that the cross partial derivatives are zero at the corners. This is called the clamped boundary condition or the clamped spline and is used in this chapter. A detailed description of spline methods of interpolation can be found in Spath (1974).

An interpolated surface formed by a set cubic polynomials has curvature, unlike the surfaces formed by the other methods of interpolation. It has been postulated that the curvature of the potential distribution on the scalp is proportional to the flow of radial current from the brain (Nunez, p. 196, 1981). Thus, estimates of radial current flow from the brain can be made from topographic maps constructed with the bicubic-spline method (Koles *et al.*, 1989).

Three-dimensional wireframe views of the potential distribution using the triangular, bilinear and bicubic-spline methods of interpolation are presented in figures 2.2, 2.3, 2.4 respectively. Actual EEG data was used for these figures. The wireframe view is useful for visualizing characteristics of the interpolation techniques. The triangularly interpolated surface is formed with a set of intersecting triangular planes that are easy to identify in the figure. The bilinearly interpolated surface is somewhat smoother than the triangularly interpolated surface. The bicubic-spline surface is very smooth and it is not possible to visually identify the rectangular regions over which the interpolating polynomial are calculated. Unlike topographic maps produced with the triangular and bilinear methods, the bicubic-spline topographic maps are not restricted to have maxima and minima at the recording electrode sites. In addition, bicubic-spline topographic maps are more realistic because they do not contain sharp edges or boundaries which could not exist in the actual distribution of potential on the scalp.

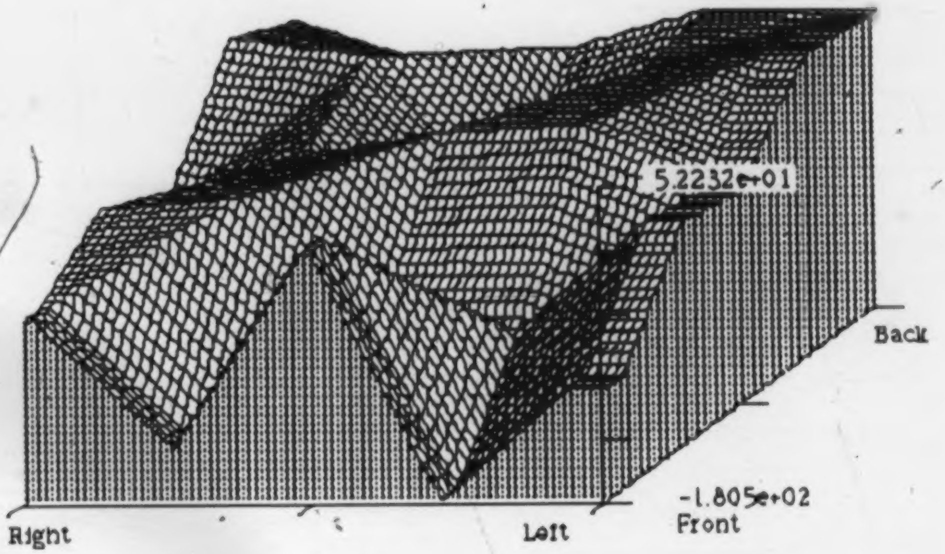

Figure 2.2 Three dimensional wireframe view of a topographic maps of actual EEG data constructed with the triangular method of interpolation. Directions on the scalp are indicated under the map. The potential is indicated in µvolts on the vertical axis.

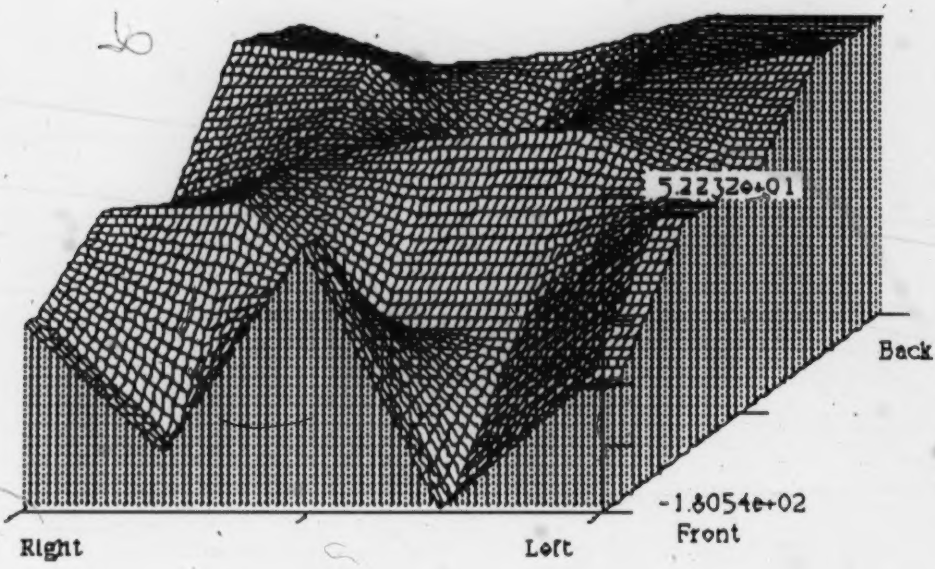

Figure 2.3 Three dimensional wireframe view of a topographic maps of actual EEG data constructed with the bilinear method of interpolation. Directions on the scalp are indicated under the map. The potential is indicated in µvolts on the vertical axis.

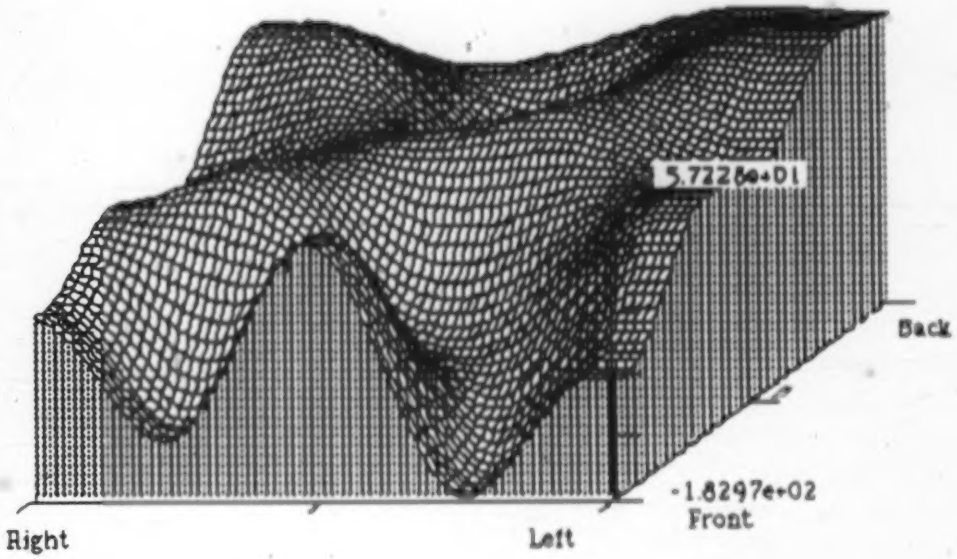

Figure 2.4 Three dimensional wireframe view of a topographic maps of actual EEG data constructed with the bicubic-spline method of interpolation. Directions on the scalp are indicated under the map. The potential is indicated in μvolts on the vertical axis.

## 2.3 A Pilot Study

A simple pilot study was carried out to test the validity of the hypothesis: topographic maps of the EEG are accurate and precise representations of the potential distribution over the scalp. If the hypothesis is correct then the EEG is an adequately-sampled, spatially-distributed signal and the spatial power spectrum of topographic maps of the EEG can be used as the basis of a classification paradigm for EEG analysis.

In order to fully test this hypothesis the actual potential distribution over the scalp would have to be known at all points and a comparison between the actual and the predicted potentials from an interpolated topographic map would have to be made. The actual potential everywhere on the scalp cannot normally be determined, therefore, to test the hypothesis the following procedure was adopted. The EEG was recorded using a modified International 10-20 Electrode System and a number of test-electrodes. The measured potentials were projected onto a plane using the Mercator method. Topographic maps were then constructed without using the potentials recorded at the test-electrode sites. A comparison of the potentials measured with the test-electrodes was made with the potentials predicted from the topographic maps. Using this procedure, the relationship between topographic maps and the actual distribution of potential on the scalp was described.

### 2.3.1 Methods

EEG data was recorded from 4 normal volunteers at the University of Alberta Hospitals' EEG laboratory. Each of the subjects (normal males, age 23 to 50) was asked to adopt a relaxed, resting mental-state and to stay awake and alert. They were to remain with their eyes closed. This normally induces an EEG with a strong alpha rhythm (frequency content between 8 Hz and 13 Hz). The EEG was recorded for a 2-minute interval from each volunteer and portions of this data were analyzed.

EEG data was recorded using two Grass model 16 EEG amplifiers connected in parallel to two pen chart recorders and to a digital data acquisition system (Koles, 1983).

The data acquisition system digitizes and stores signals at a rate of 120 samples/second with 12 bits/sample. Analog filters were set on the Grass model 16 amplifiers at 0.5 Hz and 30 Hz to limit aliasing in the digitized signal. Potentials on the scalp were recorded relative to the left ear, however, before processing they were transformed to be relative to an average-spatial reference (Nunez, p. 193, 1981).

Potentials on the scalp were recorded with the modified International 10-20 Electrode System. This system, presented in figure 2.5, is made up of the standard 19 electrodes sites of the 10-20 system augmented with 6 extra electrodes to form an approximately regular 5x5 grid over the scalp. Mercator topographic maps were generated using this grid. Up to eight test-electrodes were also used to record EEG signals. An example of the test-electrode sites is also shown in figure 2.5.

Four types of EEG data were analyzed: broad-band instantaneous EEG, alpha-band instantaneous EEG, root-mean-square (rms) EEG and alpha-band rms EEG. Topographic maps of these types of data were considered because maps of instantaneous EEG are similar to those commonly used in the analysis of evoked potentials and topographic maps of rms EEG are often used in the analysis of the background EEG (Nuwar, 1988). The alpha-band data was generated by passing the recorded signal through a digital filter designed to pass 8 Hz to 13 Hz. This was done in an effort to reduce the complexity of the maps and thereby presumably reduce the level of error. One hundred and twenty maps of the instantaneous EEG were calculated from each second of recorded data and a 2-second record was considered from each subject. The rms EEG was calculated over 0.5-second epochs, a period that is commonly used in topographical analysis of the background EEG (Duffy, 1986), and a 25-second record of EEG data from each subject was analyzed.

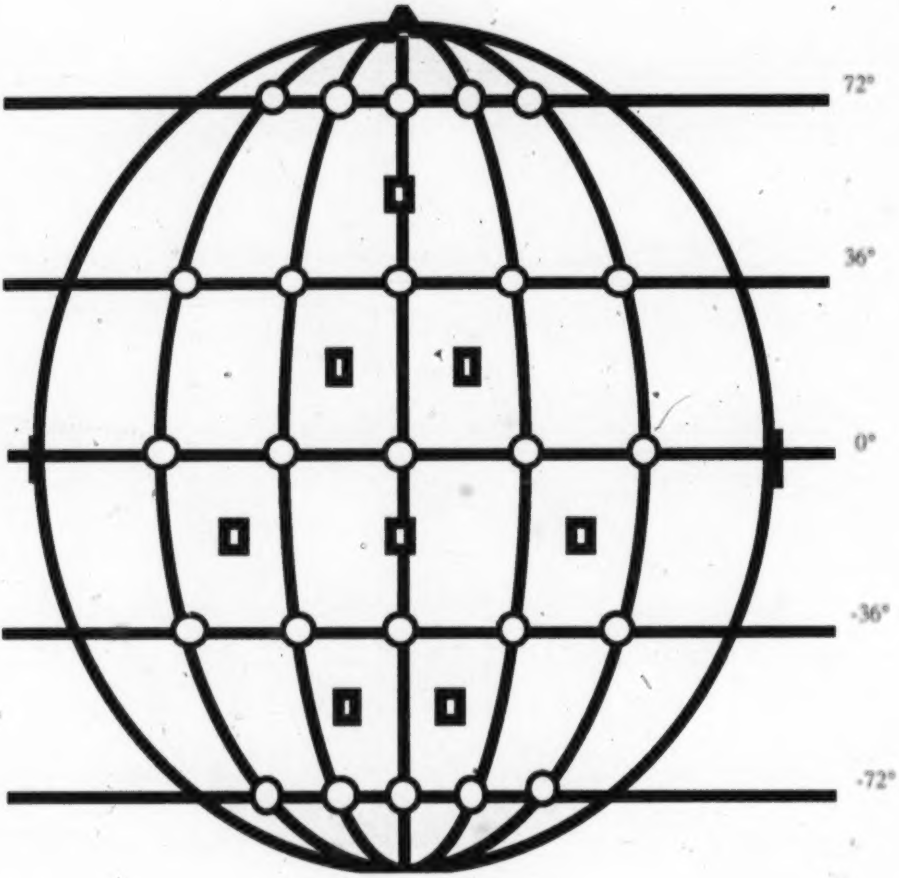

Figure 2.5 Stylized diagram of the modified International 10-20 Electrode System. The head is projected as a circle onto a plane with the nose and the ears indicated. Electrode sites of the modified International 10-20 Electrode System are indicated by small rings on meridian and parallel lines which form an approximately regular 5x5 grid over the scalp. The locations of the test-electrode are shown with small black rectangles.

A set of parameters was used to characterize the relationship between the measured potentials (from the test-electrodes) and the predicted potentials (from the topographic maps). The error signal, the difference between the measured and the predicted signals, was first calculated. The mean error (ME) was the first parameter used. It is the average difference between the measured and the predicted signals. It was defined as:

(2.3:1)

$$ME = \sum_{i=1}^{N} \frac{m_i - p_i}{N}$$

where

$m_i$ is the measured potential,

$p_i$ is the predicted potential from the topographic map,

N is the number of values in a record (240 for instantaneous EEG, 50 for rms EEG).

A value of zero for the mean error indicates that the average value of the predicted signal is equal to the average value of the measured signal.

The root-mean-square (rms) value of the error signal was the second parameter used. It was defined as:

(2.3:2)

$$rms_e = \sqrt[2]{\sum_{i=1}^{N} \frac{(m_i - p_i)^2}{N}}$$

where

$rms_e$ is the rms error signal.

Equal predicted and measured signals results in a value zero for the $rms_e$.

A regression line between the predicted and the measured potentials was calculated. The slope of the regression line was the third parameter used. A value of 1 for the slope indicates that a change in the mean value of the measured signal corresponds to an equal change in the mean value of the predicted signal.

The fourth parameter used was the coefficient of determination ($r^2$) which is commonly provided in regression analysis. The coefficient of determination may be interpreted as an indicator of statistical variation of a population about the regression line. A value of 1 indicates that the interpolated values fall exactly on the regression line while a value of 0 indicates that the regression line can not be used to describe the relationship between the predicted and measured signals. The coefficient of correlation (r) is the square root of the coefficient of determination and is commonly used to assess the linearity of the relationship between two time series.

The final parameter used to compare the measured and the predicted signals was the $\chi^2$ goodness-of-fit statistic. It is defined as (Hoel, p. 228, 1971):

(2.3:2)

$$\chi^2 = \sum_{i=1}^{N} \frac{(m_i - p_i)^2}{m_i} \qquad df = N-1$$

The $\chi^2$ statistic is a criterion for determining the confidence with which both the measured and the predicted signals can be considered as samples from the same distribution. The $\chi^2$ statistic was not used in the analysis of the instantaneous EEG data because of possible 0 values for $m_i$.

### 2.3.2 Results

Before discussing the results of this study, typical examples of measured, predicted and error signals are presented in figures 2.6, - , 2.9. These figures are representative of a 1-second record of instantaneous EEG data.

In figure 2.6 the measured signal and the predicted signals for a test-electrode site located over the left-occipital region of the scalp are presented as time series. The predicted signals were produced using triangular, bilinear and bicubic-spline interpolations. The three interpolated signals appear to be similar.

The data used in figure 2.6 may be presented as a set of points on a graph of predicted potential versus measured potential. The set of points will form a line if there is a linear relationship between these variables. Such a graph is presented in figure 2.7 for bilinearly interpolated data. The regression line between the two variables is also presented. The slope of the line will be 1 if the measured potentials are equal to the predicted potentials. The slope of the regression line is 0.987 indicating that, in this example, the predicted signal slightly under-estimated the magnitude of the measured signal. The $r^2$ value of the regression line is 0.968 indicating that 96.8% of the variance in the predicted signal can be explained by the regression line.

The error signal of the bilinear interpolation is shown in figure 2.8 as a time series. The error signal in this example has a mean value of -0.124 μV and a rms value of 6.52 μV. These values can be compared to the mean and rms values of the measured signal, -1.02 μV and 25.5 μV respectively. The mean values of both the error signal and the measured signal are small relative to signals routinely recorded in the EEG. The rms value of the error signal is about 25% of the rms value of the measured signal. In figure 2.9 the error signal is plotted against the measured signal. There appears to be little correlation between the error signal and the measured signal.

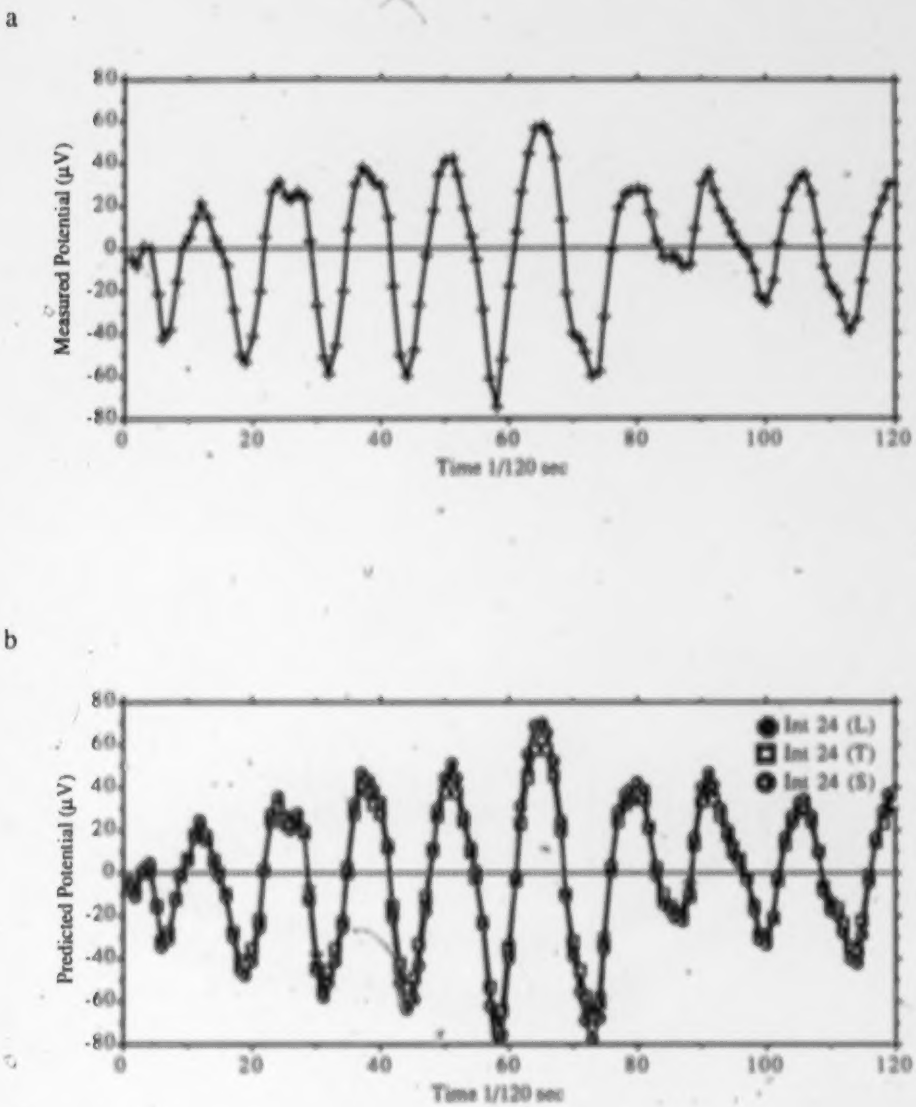

Figure 2.6 Time series of the instantaneous potential from the left-occipital region of the scalp: (a) shows measured potential, (b) shows interpolated potential using bilinear (L), triangular (T), and bicubic spline (S) methods. These graphs represent a 1-second EEG record.

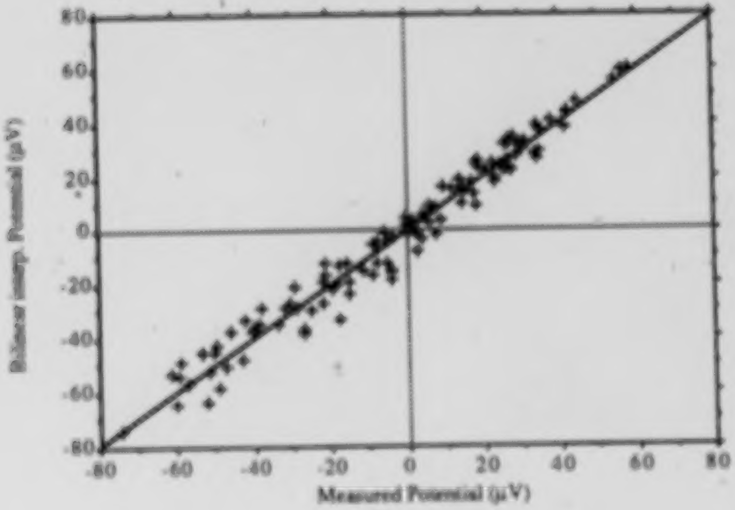

$y = 0.987x + 0.095, \quad r^2 = 0.968$

Figure 2.7 Predicted signal from bilinear interpolation plotted against measured potential for left-occipital test-electrode site. The expected value of the slope of the regression line and of the $r^2$ value is 1.

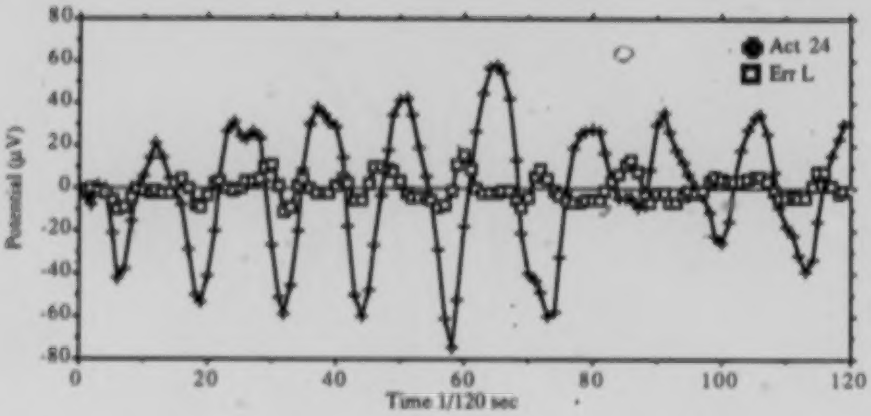

Figure 2.8 Time series of measured and error potentials from topographic maps constructed using bilinear interpolation. The bilinear interpolated signal is presented in figure 2.6. The time series represents a 1 second record of EEG data.

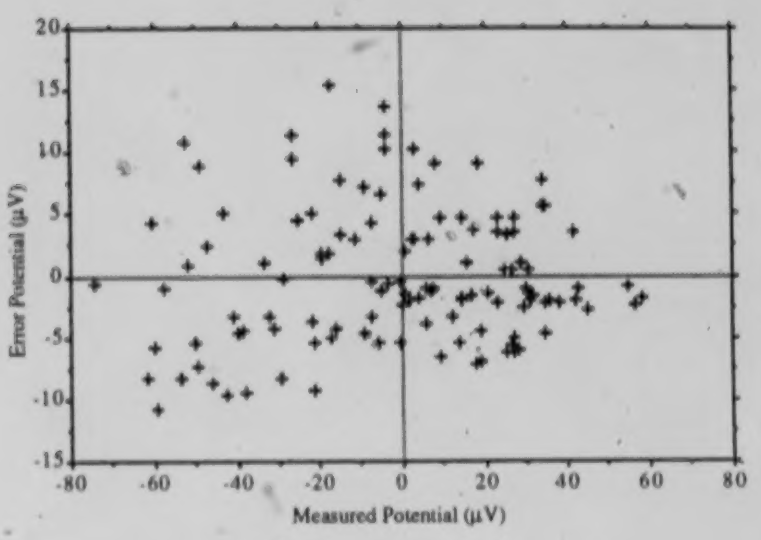

Figure 2.9 Graph of error signal from bilinear interpolation plotted against measured potential from left-occipital region of the scalp.

#### 2.3.2.1 Analysis of Instantaneous EEG Data

A summary of the results from a comparison between the measured and the predicted potentials at the test-electrode sites for instantaneous EEG data is shown in table 2.1. This table was derived from topographic maps constructed using triangular, bilinear and bicubic-spline interpolations. Values for the parameters discussed in section 2.3.1 are presented in this table.

The EEG data used for table 2.1 was recorded from 4 normal volunteers. There were six test-electrodes applied to subject 1 and eight test-electrodes were applied to subjects 2, 3 and 4. The numbers in the table are the average values over all the test-electrodes applied to each subject. It was assumed that these average values were representative of the entire topographic map rather than specific regions.

It should be noted that the signals recorded from the test-electrodes sites were not completely homogeneous: larger amplitude signals were measured at peripheral locations than in more central locations. It has previously been observed that the error signal in topographic mapping can have a spatial dependence (Koles and Paranjape, 1988). In this data there appeared to be relatively larger error in the interpolations of low amplitude signals.

The first set of parameters in table 2.1 is the mean error (ME) for both broad-band and alpha-band EEG. The mean error is always <1 μV, irrespective of the method of interpolation that was used. The mean error can be considered as small relative to the magnitude of the signals that are routinely recorded in the EEG.

The rms error ($rms_e$) is also presented in table 2.1. It can be compared to the rms value of the measured signal. The rms error is relatively large, it is in the order of 50% of the rms value of the measured signal for broad-band EEG, and in the order of 37% of the rms value of the measured signal for alpha-band EEG.

Table 2.1 also indicates that the slope of the regression line (slope) for alpha-band EEG is greater than the slope for broad-band EEG for all subjects and with all methods of interpolation. The average slope for alpha-band EEG is 0.884 (SD=0.095) while for broad-band EEG it is 0.784 (SD=0.132). The slope of the regression line between the predicted and the measured signals is <1 for all but one subject. The average value and the standard deviation of the slope indicate that during positive excursions of the measured signal there tend to be negative errors in the predicted signal and during negative excursions of the measured signal there tend to be positive errors in the predicted signal. These errors are distributed about zero and their average value is small (ie. small mean error). The $r^2$ value of the regression with alpha-band EEG is always closer to 1 than that found with broad-band EEG, indicating that the regression line explains more of the variance for alpha-band EEG than for broad-band EEG.

The method of interpolation has only a small effect on the relationship between the topographic map and the actual distribution of potential. The slope of the regression line in the bicubic-spline topographic maps is closer to 1 than that for either the triangular or the bilinear methods of interpolation. The slope is on average 0.120 (SD=0.038) greater than the slope of the regression line for the triangular or bilinear methods of interpolation. On the other hand, the $r^2$ value of the bilinear interpolations is generally closer to 1 than with the other methods of interpolation. However, there are only small differences between the $r^2$ values of the three methods. Lastly, the rms error signal of the bilinear method appears be the smallest followed by that for the triangular and then the bicubic-spline methods.

#### 2.3.2.2 Analysis of rms EEG Data

In table 2.2 results of the analysis of topographic maps of rms EEG data are presented. The triangular, bilinear and bicubic-spline methods of interpolation are again used. The format of table 2.2 is similar to that used in table 2.1, however, a row indicating the probability that the predicted signal and the measured signal are from the same distribution, as determined with the $\chi^2$ goodness-of-fit test, is also provided in this table.

The mean error in the topographic maps of the broad-band rms EEG is larger than that found with alpha-band rms EEG. The mean error is still small ($<2\mu V$) however, relative to EEG signals routinely recorded from the scalp. The ratio of the mean error to the mean value of the measured signal is a good indicator of the level of the consistent error in the interpolation. For both the broad-band and the alpha-band EEG data this ratio is $<0.05$.

It was observed in the previous section that errors are consistently larger with broad-band EEG than with alpha-band EEG. This is not seen in the results presented in table 2.2, results for both broad-band and alpha-band rms EEG maps were quite similar. The rms error was on average 18% of the rms value of the measured signal for broad-band EEG and 22% for alpha-band EEG. This indicates a large improvement in accuracy in topographic maps of rms EEG data over maps of the instantaneous EEG data.

The slope of the regression line was closer to 1 for broad-band EEG than for alpha-band EEG (in 3 of 4 subjects). These differences of the slope for rms EEG data were smaller than those found for instantaneous EEG data. The $r^2$ value of the regression line is similar for broad-band EEG and alpha-band EEG maps.

The $\chi^2$ goodness-of-fit statistic indicates the probability that the measured and the predicted signals are from the same distribution. Topographic maps of alpha-band EEG consistently have a value of $>0.80$ while topographic maps of broad-band EEG have a larger range of values. For example, in the case of subject 2 the value is 0.999 while in the case of subject 1 it is 0.526.

The results presented in table 2.2 indicate that for rms EEG data the characteristics of topographic maps of alpha-band and broad-band EEG are generally quite similar. The mean error, rms error, slope and $r^2$ value of the broad-band EEG are marginally closer to their expected values that for alpha-band EEG, however, the $\chi^2$ goodness-of-fit test shows that the probability that the measured signals and the predicted signals are from the same population is highest for alpha-band EEG data.

Table 2.1
Table of parameters from the analysis of error in topographic maps of instantaneous potential and filtered instantaneous potential from the scalp.

| | | SUB 1 | | SUB 2 | | SUB 3 | | SUB 4 | |
|---|---|---|---|---|---|---|---|---|---|
| | | UF | F | UF | F | UF | F | UF | F |
| ME | L | 0.445 µV | -.032 µV | .058 µV | .009 µV | -.168 µV | .001 µV | -.047 µV | .028 µV |
| | T | 0.428 µV | -.033 µV | .082 µV | .012 µV | -.129 µV | -.002 µV | -.082 µV | .015 µ V |
| | S | 0.516 µV | -.032 µV | .067 µV | .013 µV | -.138 µV | .003 µV | -.037 µV | .033 µV |
| $rms_e$ | L | 33.517 µV | 4.188 µV | 3.974 µV | 2.124 µV | 11.107 µV | 2.524 µV | 6.482 µV | 3.155 µV |
| | T | 33.470 µV | 4.733 µV | 4.124 µV | 2.108 µV | 11.389 µV | 2.676 µV | 6.261 µV | 3.327 µV |
| | S | 34.903 µV | 4.436 µV | 4.012 µV | 2.052 µV | 11.466 µV | 2.749 µV | 7.663 µV | 3.693 µV |
| Slope | L | .637 | .902 | .821 | .853 | .648 | .732 | .886 | .901 |
| | T | .638 | .900 | .845 | .887 | .648 | .717 | .865 | .865 |
| | S | .688 | .994 | .948 | .965 | .766 | .845 | 1.015 | 1.045 |
| $r^2$ | L | .471 | .794 | .925 | .958 | .682 | .709 | .911 | .924 |
| | T | .473 | .748 | .910 | .949 | .667 | .675 | .910 | .918 |
| | S | .468 | .799 | .913 | .949 | .673 | .689 | .898 | .914 |
| $mean_m$ | | .424 µV | -.016 µV | -.127 µV | -.033 µV | -.246 µV | .015 µV | -.148 µV | .027 µV |
| $rms_m$ | | 43.737 µV | 8.908 µV | 13.489 µV | 9.046 µV | 19.659 µV | 4.673 µV | 21.643 µV | 11.422 µV |

UF - unfiltered data.
F - filtered data.
ME - mean difference between measured and predicted potentials.
$rms_e$ - root-mean-square value of error signal.
Slope - slope of regression line from graph of measured (independent variable) verses predicted (dependent variable) potentials.
$r^2$ - coefficient of determination for regression.
$mean_m$ - mean value of measured signal.
$rms_m$ - root-mean-square value of measured signal.
L - bilinear interpolated topographic maps.
T - triangle interpolated topographic maps.
S - bicubic spline interpolated topographic maps.

Table 2.2
Table of parameters from analysis of error in topographic maps of rms value data of unfiltered and filtered potentials from the scalp.

| | | SUB 1 | | SUB 2 | | SUB 3 | | SUB 4 | |
|---|---|---|---|---|---|---|---|---|---|
| | | UF | F | UF | F | UF | F | UF | F |
| ME | L | -1.589 µV | -.337 µV | -.268 µV | -.221 µV | -.225 µV | -.116 µV | -.347 µV | -.324 µV |
| | T | -1.852 µV | -.432 µV | -.235 µV | -.227 µV | -.186 µV | -.122 µV | .528 µV | -.063 µV |
| | S | -0.574 µV | -.063 µV | .181 µV | .101 µV | -.143 µV | -.063 µV | -.669 µV | -.671 µV |
| $rms_e$ | L | 5.017 µV | 2.308 µV | 1.747 µV | 1.653 µV | 5.555 µV | 1.633 µV | 3.654 µV | 2.373 µV |
| | T | 5.661 µV | 2.446 µV | 1.777 µV | 1.670 µV | 5.351 µV | 1.681 µV | 3.471 µV | 2.360 µV |
| | S | 5.494 µV | 2.241 µV | 1.539 µV | 1.307 µV | 6.618 µV | 1.658 µV | 3.619 µV | 2.649 µV |
| Slope | L | .773 | .689 | .739 | .633 | .381 | .753 | .800 | .792 |
| | T | .810 | .705 | .778 | .677 | .407 | .777 | .797 | .790 |
| | S | .851 | .777 | .933 | .840 | .352 | .856 | 1.065 | 1.049 |
| $r^2$ | L | .747 | .692 | .826 | .721 | .236 | .729 | .805 | .810 |
| | T | .772 | .660 | .797 | .706 | .274 | .717 | .821 | .809 |
| | S | .791 | .710 | .847 | .817 | .135 | .738 | .859 | .831 |
| $\chi^2$ | L | .587 | .853 | .993 | .821 | .581 | .990 | .840 | .872 |
| | T | .526 | .839 | .996 | .829 | .597 | .989 | .847 | .890 |
| | S | .629 | .840 | .999 | .995 | .407 | .920 | .704 | .818 |
| $mean_m$ | | 38.193 µV | 9.646 µV | 12.573 µV | 7.552 µV | 18.954 µV | 5.017 µV | 19.983 µV | 10.807 µV |
| $rms_m$ | | 39.685 µV | 10.487 µV | 13.143 µV | 8.142 µV | 19.084 µV | 5.911 µV | 21.615 µV | 12.074 µV |

UF - unfiltered data.
F - filtered data.
ME - mean difference between measured and predicted potentials.
$rms_e$ - root-mean-square value of error signal.
Slope - slope of regression line from graph of measured (independent variable) verses predicted (dependent variable) potential.
$r^2$ - coefficient of determination for regression.
$\chi^2$ - probability that measured and predicted potentials are from the same population.
$mean_m$ - mean value of measured signal.
$rms_m$ - root-mean-square value of measured signal.
L - bilinear interpolated topographic maps.
T - triangle interpolated topographic maps.
S - bicubic spline interpolated topographic maps.

### 2.3.4 Conclusions

This pilot study was designed to assess the relationship between topographic maps and the spatial distribution of various types of EEG data. It is concluded that topographic maps of the EEG are in fact representative of the distribution of electric potential on the scalp. The mean value of the error signal for the maps was small for all data indicating that the topographic maps have a low bias. However, the rms value of the error signal was large for broad-band instantaneous EEG data indicating low precision. By restricting the temporal frequency content of the EEG to the alpha-band, about a 20% decrease in the percentage of rms error was obtained. By further restricting temporal frequency and considering rms EEG data (calculated over 0.5 sec epochs) the rms error became about 20% of the measured signal. The difference in the rms error between broad-band and alpha-band rms EEG topographic maps was small. It is concluded therefore, that topographic maps of rms EEG data can be considered representative of the rms potential distribution on the scalp.

The regression of the measured and predicted potentials indicated that a close to linear relationship exists for all EEG data. The slope of the regression was generally close to unity and the coefficient of determination ($r^2$ value) was generally greater than 0.7.

The method of interpolation did not significantly affect the quality of the topographic map. No one method of interpolation was consistently better in terms of the parameters that were studied. Interpolations based on the bilinear method appeared to have the smallest rms error and the bicubic-spline interpolations appeared to have a slope nearest to 1 for the regression between predicted signals and measured signals.

It is concluded that error in topographic maps is related to the sample density (which was not varied in this study) and the temporal frequency content of EEG data. It is further concluded that alpha-band rms EEG data can be considered as an adequately-sampled, spatially distributed signal on which further spatial analysis may be performed.

# Chapter 3

# Power Spectrum Estimation

## 3.0 Introduction

When a glass prism is placed in the path of a beam of sunlight it causes the disassociation of the light into its constituent components. This empirical discovery, made by Sir Isaac Newton, was the first reported instance of spectral analysis. Robert Wilhelm Bunsen repeated this experiment and carried it much further when he studied the light emitted from a burning oil rag. Bunsen was able to identify specific lines in the spectrum of the emitted light. He suggested that these spectral lines were characteristic of particular chemical elements. Further he proposed spectral lines as a new method of identification and classification of elements (Robinson, 1982).

One of the most basic features of all scientific inquiry is to identify, classify and define natural phenomena. In order to facilitate this, there has been a significant attempt to define natural phenomena in terms of analytic functions. Jean Baptist Joseph de Fourier made a major contribution to this effort in 1807. In an address to the French Academy he suggested that any arbitrary graph or signal could be defined completely by the superposition of an infinite number of sine and cosine functions. Thus he suggested a unique method to define a signal in terms of an orthogonal set of basis functions. Fourier's method still forms a corner stone of modern spectral analysis (Robinson, 1982).

## 3.1 Time Series

A discrete time series ($x_n = x_1, x_2, \ldots, x_N$), is a set of measurements of a process at times $\Delta t, 2\Delta t, \ldots N\Delta t$. Such a set of measurements may be generated in practice by uniformly sampling a continuous-time signal $x(t)$ at the rate of $1/\Delta t$ samples per second.

A time series is said to be deterministic if the future values of the series can be exactly described by some mathematical function. On the other hand, the time series is said to be random if the future values of the series can only be described in terms of a probability distribution function. A stochastic process is a random phenomenon that evolves in time according to some probabilistic laws and a random time series represents one particular realization of the process. A stochastic process is said to be strictly stationary if its properties are unaffected by a change in the time origin. An important consequence of strict stationarity is that the entire probability structure of the process depends only on time differences.

### 3.2 The Autocorrelation Function

Consider the time series $x_n$, which is one particular realization of a discrete stochastic process. The mean of this process is defined as:

(3.2:1)

$$\mu_x(n) = E[x_n]$$

where

E denotes the expectation operator.

The autocorrelation function (ACF) of the process is defined in terms of lag, m, and time origin, n, as:

(3.2:2)

$$R_{xx}(m,n) = E[x_{n+m}\, x_n^*]$$

where

* denotes the complex conjugate operation.

The autocovariance function (ACV) of the process, for lag m and time origin n, is defined as:

(3.2:3)

$$C_{xx}(m,n) = E[\,(x_{n+m}-\mu_x(n+m))\,(x_n^*-\mu_x^*(n))\,]$$

In the case of a signal with zero mean the ACF and the ACV are equal. The ACF and the ACV represent a time-domain description of the second order statistics of a stochastic process, and they can be useful in representing and characterizing the process. A stochastic process is said to be wide sense stationarity (WSS) if its mean and its ACF, and thus its ACV as well, are indepehdent of the time origin. An ACF of a WSS process exhibits conjugate symmetry, that is:

(3.2:4)

$$R_{xx}(-m) = R_{xx}^*(m)$$

### 3.3 Power Spectrum Estimation

The general problem of spectral estimation is that of determining the spectral content of a stochastic process based on a finite set of observations from that process. The power spectrum (PS), which is denoted by P(f), of a stochastic process $x_n$ is defined as (Oppenheim and Schafer, p. 534, 1975):

(3.3:1)

$$P(f) = \sum_{m=-\infty}^{\infty} R_{xx}(m) \exp(-j\, 2\pi\, f\, m) \qquad -\frac{1}{2} \le f \le \frac{1}{2}$$

In the characterization of a stochastic process, use of the PS is often preferred to the ACF because a spectral representation may reveal such useful information as obscure periodicities or close spectral peaks.

The PS, as defined in equation (3.3:1), is the weighted sum of an infinite number of ACF values, thus the task of determining the true PS based on a finite number of ACF values is impossible. In most situations in which the PS of an actual process is to be determined the amount of data available is limited. This may be due to physical constraints such as a limited data holding capacity, or other more fundamental reasons, such as a finite duration of the process of interest. Thus, in many practical situations one must do PS analysis based on only a subset of the ACF which is estimated from the limited data set.

### 3.3.1 Classical Methods

Until 1967, most of the procedures used for estimating the power spectrum of a stochastic process were based on the classical work by Blackman and Tukey. In these procedures, the available time series is first used to estimate the ACF for a limited number of lags, and then the ACF is multiplied by a window function that goes to zero beyond the largest available lag. Next, the Fourier transform of this product is determined to obtain an estimate of the power spectrum.

An alternate procedure for estimating the power spectrum is based on the so-called periodogram, which is defined as the squared magnitude of the Fourier transform of the available time series. This approach has become rather popular with the introduction of the Fast Fourier Transform (FFT) algorithm for performing discrete Fourier transforms. The procedure results in a significant reduction in the number of computations and in the amount of storage required for long data records. The periodogram can be shown to be equivalent to the Blackman-Tukey approach if the ACF is estimated from data assumed to be zero outside the measurement interval (Oppenheim and Schafer, 1975).

Spectral density estimators based on the Blackman-Tukey approach and the periodogram are said to be linear (Haykin, p. 6, 1983). A major shortcoming of these linear estimators however, is that misleading or false conclusions may sometimes be drawn by using them. This is a result of the fact that they all involve the use of window functions which are independent of the properties of the stochastic process being analyzed. The windowing problem may be particularly acute if the available time series is limited in length so that the window on the process makes it impossible to resolve the frequency components of interest.

Two commonly used estimators of the ACF (Oppenheim and Schafer, 1975, p. 539-540) for N values of the real time series $x_n$ are:

(3.3:2)

$$R_{xx}''(m) = \frac{1}{N} \sum_{n=0}^{N-|m|-1} x_n x_{m+n} \qquad 0 \le m \le N-1$$

$$R_{xx}''(m) = 0 \qquad m > N-1$$

$$R_{xx}''(-m) = R_{xx}''(m)$$

(3.3:3)

$$R_{xx}'(m) = \frac{1}{N-m} \sum_{n=0}^{N-|m|-1} x_n x_{m+n} \qquad 0 \le m \le N-1$$

$$R_{xx}'(m) = 0 \qquad m > N-1$$

$$R_{xx}'(-m) = R_{xx}'(m)$$

It is useful to compare these estimators by calculating their expected values. They are (Jenkins and Watts, p. 175, 1968):

(3.3:4)

$$E\,[\,R_{xx}''(m)\,] = ((N-m)/N)\,R_{xx}(m)$$

(3.3:5)

$$E\,[\,R_{xx}'(m)\,] = R_{xx}(m) \qquad |m| \le (N-1).$$

$R_{xx}''(m)$ is a biased estimator of the ACF. Its expected value is the ACF multiplied by a triangular window. In the limit of infinite data however, the expected value of $R_{xx}''(m)$ is the ACF. Thus $R_{xx}''(m)$ is described as an asymptotically unbiased estimator of the ACF. $R_{xx}'(m)$, on the other hand, is an unbiased estimator of the ACF.

The PSE based on $R_{xx}''(m)$ is called the periodogram (PG) PSE. That is:

(3.3:6)

$$\text{PG PSE}(f) = \sum_{m=-(N-1)}^{(N-1)} R_{xx}''(m) \exp(-j\, 2\pi\, m\, f)$$

The PG PSE is, however, much easier to calculate from the data directly (Oppenheim and Schafer, 1975, p. 542) as:

(3.3:7)

$$\text{PG PSE}(f) = \left[ \frac{1}{N} \left| \sum_{n=0}^{N-1} x_n \exp(-j\, 2\pi\, f\, n) \right|^2 \right]$$

It is interesting to determine the bias and variance of the PG PSE. The bias of an estimator is defined as the true value of the parameter minus its expected value. The variance of an estimator is a measure of the variability of the estimator about its expected value. Generally speaking, an estimator is satisfactory and is said to be consistent if, as the data available for the estimate increases, the bias and the variance of the estimator decreases (Oppenheim and Schafer, p. 543, 1975).

The expected value of the PG PSE is:

(3.3:8)

$$E\,[\,\text{PG PSE}(f)] = \sum_{m=-(N-1)}^{(N-1)} \left[ \frac{N-m}{N} \right] R_{xx}(m) \exp(-j\, 2\pi\, f\, m)$$

(3.3:9)

$$E\,[\,\text{PG PSE}(f)] = \int_{-0.5}^{0.5} W_B(f-\xi)\, P(\xi)\, d\xi$$

where

$P(\xi)$ is the actual spectrum of the process,

$\xi$ is the variable of integration,

$$W_B(f) = \frac{1}{N} \left[ \frac{\sin(\pi f N)}{\sin(\pi f)} \right]^2 .$$

In the limit as N tends to infinity $W_B$ becomes a Dirac delta function and the expected value of the PG PSE becomes the true PS. Thus, the PG PSE is described as an asymptotically unbiased estimator.

It is not straight-forward to determine the variance of the PG PSE for most signals. However, if the time series to be analyzed is obtained from a Gaussian, white noise process the variance of the PG PSE can be shown to be (Oppenheim and Schafer, p. 544, 1975):

(3.3:10)

$$\mathrm{Var}\,[\ \mathrm{PG\ PSE}(f)] = P(f)^2\left[1 + \left[\frac{C}{N}\right]^2\right]$$

where

C is sin(πfN)/sin(πf).

In the limit as N goes to infinity, the second term in equation (3.3:10) approaches zero and the variance of the PG PSE tends to the true PS squared. Thus, the PG PSE is described as an inconsistent estimate of the PS.

The PG method can be modified to reduce its variance by averaging a number of independent PG PSEs together. This approach is attributed to Bartlett (Oppenheim and Schafer, 1975, p. 548). A long data record of length N, is divided into smaller segments of length L. The PG PSE is calculated for each segment and the PSEs thus obtained are averaged (called BA PSE here).

The variance of the BA PSE is:

(3.3:11)

$$\mathrm{Var}\,[\ \mathrm{BA\ PSE}] \approx \frac{1}{\left[\frac{N}{L}\right]}\left[P(f)^2\left[1 + \left[\frac{C}{L}\right]^2\right]\right]$$

In the limit as N goes to infinity the variance of the BA PSE goes to zero. Thus the BA PSE is consistent.

It is important to note that in dividing the data into segments of length L (L<N), the bias of the BA PSE increases over that of the PG PSE of the entire data set. This can be observed by replacing N with L (L<N) in equation (3.3:8). It is not possible to resolve fine detail in the BA PSE because the function $W_B$ smears these components together if they are

separated by less than 1/L. The spectral estimator is thus said to have a resolution of 1/L cycles/sample. For maximum resolution in the BA PSE, L should be chosen as large as possible (clearly to the limit of L=N which is the PG PSE). However, for a maximum reduction in the variance one must choose L as small as possible, so that N/L in equation (3.3:11) is large. Thus, the goals of low bias and low variance are in conflict and cannot be met simultaneously. Bias must be sacrificed for variance or vice versa.

The PSE based on the ACF estimate, $R_{xx}'(m)$, is called the Blackman-Tukey (B-T) PSE. That is:

(3.3:12)

$$\text{B-T PSE}(f) = \sum_{m=-(N-1)}^{(N-1)} R_{xx}'(m) \exp(-j\, 2\pi\, m\, f)$$

The expected value of the B-T PSE is:

(3.3:13)

$$E[\text{ B-T PSE}(f)] = \sum_{m=-(N-1)}^{(N-1)} E[\, R_{xx}'(m)]\ \exp(-j\, 2\pi\, f\, m)$$

(3.3:14)

$$E[\text{ B-T PSE}(f)] = \int_{-0.5}^{0.5} W_{BT}(f-\xi)\, P(\xi)\ d\xi$$

where

$\xi$ is the variable of integration,

$$W_{BT}(f) = \frac{2}{N}\left[\frac{\sin(2\pi f N)}{\sin(2\pi f)}\right].$$

In the limit that N goes to infinity, the expected value of this estimator is the true PS, thus the B-T PSE is an asymptotically unbiased estimate.

As with the PG PSE, the variance of the B-T PSE does not decrease as N increases and the method is described as inconsistent. To obtain a consistent PSE some modification must be made to the B-T PSE. There are a number of techniques to reduce the variance of the B-T PSE. One such technique is to consider only part of the ACF estimate. This can be achieved by multiplying $R_{xx}'(m)$ by a rectangular window of length L where L<<2N-1. This has the effect of convolving the B-T PSE with the FT of the rectangular window function of length L. The resulting PSE is smoother and has a reduced variance. It is called B-T$^+$ PSE here. The variance of the B-T$^+$ PSE can be shown to be (Oppenheim and Schafer, 1975, p. 551):

(3.3:15)

$$\mathrm{Var}\,[\text{ B-T}^+\text{ PSE}] \approx \frac{2L}{N}\,P(f)^2$$

In the limit as N tends to infinity the variance of the B-T$^+$ PSE goes to zero.

A second technique for consistent PS analysis is to average independent B-T PSEs together. This is equivalent to averaging independent ACF estimates and is similar to the Bartlett approach. PSEs based on the averaged ACF will be referred to here as the B$\bar{\text{T}}$ PSEs.

Both techniques for converting B-T PSEs into consistent PSEs require that a smaller extent ACF be used than that which can be estimated from the data. Therefore, as with the BA PSE, these techniques for producing consistent PSEs involve trading off bias for lower variance.

The principle conclusion which results from the study of classical methods is that the variance of the estimator can be reduced if an increase in the bias is accepted, but both types of errors can not be reduced simultaneously. If the bias is too severe or if the variance is too large for a given application, then other methods of PS analysis have to be considered. If, however, the resolution is adequate and the variance is at an acceptable level, the classical methods provide satisfactory PSEs.

## 3.4 Modern Methods of Power Spectrum Estimation

The classical methods of PS analysis involve the application of the Fourier transform to windowed data or windowed ACF estimates and therefore their use requires the implicit assumption that the unobserved data or ACF values are zero. This is normally an unrealistic assumption and results in smearing of spectral components of the PS. Often there is more information available about the process from which the data samples are taken and it is possible to make more reasonable assumptions about the data or the ACF. Through the use of prior knowledge or assumptions, a model of the process generating the data may be selected. If the model is a good approximation of the generating process it is possible to obtain a high resolution spectral estimate as well as a parametric description of the process.

Modern parametric methods of time series analysis are divided into 3 large groups, autoregressive (AR), moving average (MA), and autoregressive-moving average (ARMA). These methods of analysis generate predictive models of stochastic processes. In this section each of these models is described followed by a discussion of some methods for estimating the parameters of these models.

The AR approach to time series analysis is the most popular of the three modeling methods. A model is developed which predicts future terms of a time series as the linear combination of previous terms in the time series and a noise term. It is expressed mathematically as (Ulrych and Ooe, 1983):

(3.4:1)

$$x_n = \sum_{k=1}^{p} a_k x_{n-k} + n_n$$

where

$x_n'$ is an estimate of the $n^{th}$ value of the time series,

$x_{n-k}$ are the last k known terms of the time series,

$n_n$ is the $n^{th}$ value of a Gaussian, white noise series,

$a_k$ is the $k^{th}$ coefficient of the model of order P.

The MA model of a stochastic process, on the other hand, predicts future terms of a time series as the sum of a set of values from a Gaussian, white noise process. The model form is (Ulrych and Ooe, 1983):

(3.4:2)

$$x_n' = \sum_{k=1}^{Q} b_k q_{n-k}$$

where

$q_n$ is the $n^{th}$ value of a Gaussian, white noise series,

$b_k$ is the $k^{th}$ coefficient of the model of order Q.

The ARMA approach uses both the AR and the MA models together. The mathematical expression for this model is (Ulrych and Ooe, 1983):

(3.4:3)

$$x_n' = \sum_{j=1}^{Q} b_j q_{n-j} - \sum_{k=1}^{P} a_k x_{n-k}$$

Wold pointed out, in 1938, that all stationary time series can be decomposed into deterministic and non-deterministic components. He suggested that a time series from a real valued, stationary stochastic process can be decomposed as:

(3.4:4)

$$y_n = u_n + v_n$$

where

$y_n$ is the time series,

$u_n$ is the deterministic component and is completely predictable,

$v_n$ is the non-deterministic component.

In addition, the non-deterministic component, $v_n$, has a MA representation such that:

(3.4:5)

$$E[q_n] = 0$$

and

$$E[q_n q_m] = \sigma_q^2 \delta_{nm}$$

where

$\sigma_q^2$ is the variance of the noise process,

$\delta_{nm}$ is the kronecker delta function.

Based on this approach it would appear that the best method of characterizing a time series is the ARMA model, with the AR model representing the deterministic part of the signal and the MA model representing the stochastic part of the signal (Ulrych and Ooe 1983). The ARMA model is considered a parsimonious representation of an unknown random process.

Parameter estimation for MA models of order Q is now discussed. Recall that the form of the model is:

(3.4:2)

$$x_n' = \sum_{k=1}^{Q} b_k q_{n-k}$$

The difference between the actual value of the time series, $x_n$, and the estimated value, $x_n'$, is defined as the error signal, $e_n$. It can be expressed as:

(3.4:6)

$$e_n = x_n - \sum_{k=1}^{Q} b_k q_{n-k}$$

The variance of $e_n$ is:

(3.4:7)

$$\mathrm{Var}[e_n] = E[e_n^2] = E[(x_n - \mathbf{q}_n^T \mathbf{b})^2]$$

where

bold type indicates a vector

for example

$$\mathbf{q}_n^T \mathbf{b} = \sum_{k=1}^{Q} b_k q_{n-k}$$

Using the method of least squares minimization the gradient of the variance is set to zero:

(3.4:8)

$$\nabla[E[e_n^2]] = -2E[x_n - \mathbf{q}_n{}^T\mathbf{b}]\, \mathbf{q}_n{}^T = 0$$

and,

(3.4:9)

$$E[\, x_n \mathbf{q}_n \,] - E[\, \mathbf{q}_n{}^T\mathbf{b}\, \mathbf{q}_n \,] = 0$$

$$E[\, x_n \mathbf{q}_n \,] = \sigma_q{}^2\, \mathbf{b}.$$

Therefore,

(3.4:10)

$$\frac{1}{\sigma_q^2} E[x_n \mathbf{q}_n] = \mathbf{b}$$

However, the problem is that $E[x_n \mathbf{q}_n]$ is not known so equation (3.4:10) cannot be used to determine **b**. The information which is available is of the correlation function of $x_n$. It can be shown from equation (3.4:2) that the MA ACF is:

(3.4:11)

$$E[\, x_n\, x_{n+m}] = \begin{cases} \sigma_q^2 \sum\limits_{k=|m|}^{Q} b_k\, b_{k-|m|} & \text{for } |m| \le Q \\ 0 & \text{for } |m| > Q \end{cases}$$

An ACF can be estimated from the recorded data in a number of ways (see section 3.2). By taking the z transform of this estimated ACF a polynomial in z is determined. The roots of the ACF polynomial appear in reciprocal, conjugate pairs (see section 3.7) and they can be determined by the use of, for example, the iterative Newton-Raphson method. The zeros of the ACF polynomial which lie inside the unit circle can then be used to define B(z) the z transform of the vector **b** however, this approach assumes that the coefficients of **b** are of minimum phase form.

The iterative solution to the problem of MA parameter estimation is, in general, inconvenient and if prior information is available that **b** is minimum phase, a much simpler approach can be adopted (Ulrych and Ooe, 1983). This approach is now presented.

The z transform of equation (3.4:2) is:

(3.4:12)

$$X(z) = B(z)\,Q(z)$$

where

X(z) is the z transform of the recorded time series,

B(z) is the z transform of the MA coefficient series,

Q(z) is the z transform of a white noise series.

Defining $B(z)^{-1}$ as the inverse of B(z):

(3.4:13)

$$X(z)\,B(z)^{-1} = Q\,(z).$$

Call $B(z)^{-1} = G(z)$

$$X(z)\,G(z) = Q(z).$$

Now retransforming:

(3.4:14)

$$\sum_{k=0}^{P} x_{n-k}\, g_k = q_n$$

Setting $a_k = -g_k$, k=1, 2, ...

$$x_n = q_n + a_1\, x_{n-1} + a_2\, x_{n-2} + \ldots .$$

This is the AR model of a time series and it was presented in equation (3.4:1). A major advantage of AR modeling is that the time series can have a deterministic component.

Often, purely AR models can be used to describe time series rather than the more complex ARMA or MA models. This can be done because all MA models can be represented as AR models and vice versa (Ulrych and Ooe, 1983). There are, however, some practical limitations to this due to model size. For example, a deterministic infinite extent time series requires an infinite MA model, and an exact representation of a finite MA model requires an infinite AR model.

In sections 3.5-3.7 two different approaches to the determination of the coefficients of AR models are presented. In section 3.5 parameter estimation by the least squares method is presented and in section 3.6 the maximum entropy (ME) method is discussed. The parallel between the least squares and the ME approach is presented in section 3.7 by showing that the model generated by these methods are identical for one dimensional signals.

### 3.5 AR Parameter Estimation - The Wiener Filter and the Prediction-error Filter

In this section parameter estimation for AR models of discrete one dimensional signals is presented through an analysis of the Wiener filtering problem. The prediction-error filter, a special case of the Wiener filter is presented and it is shown that the power spectrum (PS) of the input signal to the prediction filter may be determined from filter coefficients.

#### 3.5.1 Wiener Filtering

Consider a linear digital filter defined by the impulse response $h_k$ $(k=1, \dots, M)$. Suppose that a wide sense stationary time series $x_n$ of length N is applied to the input of this filter. The time series $y_n$ represents the output of the filter, so that:

(3.5:1)

$$y_n = \sum_{k=1}^{M} h_k \, x_{n-k+1}$$

The desired output of the filter is defined to be $d_n$ and the difference between the desired output and the actual output is defined as the error signal, $e_n = d_n - y_n$. The Wiener filter has coefficients which make the variance of $e_n$ a minimum. The variance of the error signal, $E\,[|e_n|^2]$, is equal to the average power of the error signal, $P_e$.

(3.5:2)

$$P_e = E\,[\,|e_n|^2\,] = E\,[\,e_n e_n^*]$$

$$\therefore$$

$$P_e = E\,[\,(d_n - y_n)(d_n^* - y_n^*)\,]$$

$$P_e = E\,[\,d_n d_n^*\,] - E\,[\,d_n y_n^*\,] - E\,[\,y_n d_n^*\,] + E\,[\,y_n y_n^*\,]$$

However,

$$y_n = \sum_{k=1}^{M} h_k \, x_{n-k+1}$$

Thus,

(3.5:3)

$$P_e = \left[\begin{array}{l} 1)\;\; E\,[\,d_n d_n^*] \;+ \\[2ex] 2)\;\; -\sum_{k=1}^{M} h_k^* \, E\,[\,d_n \, x_{n-k+1}^*] \;+ \\[2ex] 3)\;\; -\sum_{k=1}^{M} h_k \, E\,[\,x_{n-k+1} \, d_n^*] \;+ \\[2ex] 4)\;\; +\sum_{k=1}^{M} h_k \sum_{j=1}^{M} h_j^* \; E\,[\,x_{n-k+1} \, x_{n-j+1}^*] \end{array}\right.$$

The terms (indicted numerically above) in this expression can be interpreted as either the autocorrelation or the cross correlation of the signals $d_n$ and $x_n$. Each term in equation (3.5:3) is further evaluated:

1) $E\,[d_n d_n^*] = R_{dd}(0)$

where

$R_{dd}(0)$ is the autocorrelation of the signal $d_n$ at lag zero.

2)

$$-\sum_{k=1}^{M} h_k{}^* E[d_n\, x_{n-k+1}{}^*] = -\sum_{k=1}^{M} h_k{}^* R_{dx}(k-1)$$

where

$R_{dx}(k-1)$ is the cross correlation of $d_n$ and $x_n$ at lag (k-1).

The equation is written in vector notation (bold type) as:

$$-\sum_{k=1}^{M} h_k{}^*\ E[\, d_n\, x_{n-k+1}{}^*] = -\,\mathbf{h}^H\, \mathbf{R}_{dx}$$

where

$\mathbf{h}^T = h_1, h_2, h_3 \ldots h_M$

$\mathbf{R}^T{}_{dx} = R_{dx}(0), R_{dx}(1), R_{dx}(2), \ldots, R_{dx}(M-1),$

The superscript $^T$ is used to indicate the transpose operator and superscript $^H$ is used for the Hermitian operator. The Hermitian operator indicates transposition and conjugation of a vector.

3)

$$-\sum_{k=1}^{M} h_k\, E[\, x_{n-k+1}\, d_n^*] = -\,\mathbf{R}_{dx}^{H}\, \mathbf{h}$$

The above equation follows by proceeding in a fashion similar to that for term 2.

4)

$$\sum_{k=1}^{M} h_k \sum_{j=1}^{M} h_j{}^* E[x_{n-k+1}\, x_{n-j+1}{}^*] = \sum_{k=1}^{M} h_k \sum_{j=1}^{M} h_j{}^* R_{xx}(j-k) = \mathbf{h}^H\, \mathbf{R}_{xx}\, \mathbf{h}$$

The $\mathbf{R}_{xx}$ matrix is a square symmetric matrix defined by:

$$\mathbf{R}_{xx} = \begin{array}{cccccc} R_{xx}(0) & R_{xx}(-1) & R_{xx}(-2) & . & . & . \quad R_{xx}(1-M) \\ R_{xx}(-1) & R_{xx}(0) & R_{xx}(1) & . & . & . \quad R_{xx}(2-M) \\ R_{xx}(-2) & R_{xx}(-1) & R_{xx}(0) & . & . & . \\ R_{xx}(1-M) & & & . & . & . \quad R_{xx}(0) \end{array}$$

Therefore, equation (3.5:3) can be written as

(3.5:4)

$$P_e = R_{dd}(0) - \mathbf{h}^H \mathbf{R}_{dx} - \mathbf{R}_{dx}{}^H \mathbf{h} + \mathbf{h}^H \mathbf{R}_{xx} \mathbf{h}$$

The power of the error signal is minimized to determine the Wiener filter coefficients, $h_k$. The partial derivative of $P_e$ with respect to $h_k$ is therefore set equal to zero. Since the $h_k$'s can be complex, two sets of equations must be solved simultaneously. However, these equations reduce to (Haykin and Kesler, 1983):

(3.5:5)

$$0 = - \mathbf{R}_{dx}{}^H + \mathbf{h}^H \mathbf{R}_{xx} \qquad \text{as } \mathbf{R}_{xx} = \mathbf{R}_{xx}{}^H$$

$$\mathbf{R}_{xx} \mathbf{h} = \mathbf{R}_{dx}$$

Writing this out in non-vector form

$$\sum_{k=1}^{M} h_k R_{xx}(m-k) = R_{dx}(m) \qquad \text{for } m = 0, 1, 2 \dots M-1$$

This equation is called the Wiener-Hopf equation and can be used to determine the Wiener filter coefficients, $h_k$. Thus,

(3.5:6)

$$\mathbf{h} = \mathbf{R}_{xx}{}^{-1} \mathbf{R}_{dx}$$

To find the minimum power of the error signal substitute for $\mathbf{R}_{dx}$ in (3.5:4) from (3.5:5).

(3.5:7)

$$P_e = R_d(0) - \mathbf{h}^H \mathbf{R}_{dx} - \mathbf{R}_{dx}{}^H \mathbf{h} + \mathbf{h}^H \mathbf{R}_{xx} \mathbf{h}$$

$$P_e = R_d(0) - \mathbf{R}_{dx}{}^H \mathbf{h}$$

### 3.5.2 The Prediction-error Filter

The prediction-error filter follows from the analysis of a Wiener filter designed to predict future values of the time series $x_n$ (also called the Wiener prediction filter). The desired output of the Wiener prediction filter, $d_n$, is future values of the input signal, so that $d_n = x_{n+1}$. Substituting into the Wiener-Hopf equation for $d_n$ with $x_{n+1}$:

(3.5:8)

$$\sum_{k=1}^{M} h_k R_{xx}(m-k) = R_{xx}(m) \qquad \text{for } m = 0, 1, 2 \ldots M-1$$

The RHS of the Wiener-Hopf equation is now the autocorrelation of $x_n$. This equation indicates that the value of the ACF at lag m is equal to the sum of the previous M lag terms multiplied by the Wiener filter coefficients. The error in the output of this filter continues to be defined by $e_n$ and it is written as:

(3.5:9)

$$e_n = d_n - y_n$$

$$e_n = x_n - \sum_{k=1}^{M} h_k x_{n-k}$$

$$e_n = \sum_{k=0}^{M} a_k x_{n-k}$$

where

$$a_0 = 1,\ a_k = -h_k, \text{ for } k = 1, 2, \ldots M$$

Equation (3.5:9) defines the prediction-error filter because its output, $e_n$, will be the error in the output of the Wiener prediction filter (whose coefficients are defined in equation (3.5:8)). Thus $e_n$ is predicted from the input signal, $x_n$, using the $a_k$ coefficients. To find the power of the error signal substitute $x_{n+1}$ for $d_n$ in equation (3.5:7).

$$P_e = R_{dd}(0) - \mathbf{R}_{dx}^{H}\,\mathbf{h} \qquad \text{thus,}$$

$$P_e = R_{xx}(0) - \mathbf{R}_{xx}^H \mathbf{h}$$ but,

$$R_{xx}^*(k) = R_{xx}(-k)$$ so,

$$P_e = R_{xx}(0) - \sum_{k=1}^{M} h_k R_{xx}(-k)$$

(3.5:10)

$$P_e = \sum_{k=0}^{M} a_k R_{xx}(-k)$$

This equation defines the power of the error signal in the Wiener prediction filter or the power of the output of the prediction-error filter.

Combining equations (3.5:8) and (3.5:10) into a single equation results in:

(3.5:11)

$$R_{xx}(m) + \sum_{k=1}^{M} -h_k R_{xx}(m-k) = \begin{cases} P_e & m = 0 \\ 0 & m = 1, 2, \ldots M \end{cases}$$

For m = 0 this is a restatement of equation (3.5:10) and for m>0 it is a restatement of equation (3.5:8) because the second term on the LHS equals the negative of the first term. This equation can be written in terms of the prediction filter coefficients.

(3.5:12)

$$\sum_{k=0}^{M} a_k R_{xx}(m-k) = \begin{cases} P_e & m = 0 \\ 0 & m > 0 \end{cases}$$

The prediction-error filter can be written in a form similar to an AR model. Recall

(3.5:9)

$$e_n = \sum_{k=0}^{M} a_k x_{n-k}$$

$$e_n = x_n - \sum_{k=1}^{M} h_k x_{n-k}$$

$$x_n = \sum_{k=1}^{M} h_k\, x_{n-k} + e_n$$

If the error signal, $e_n$, is considered to be a white noise signal and the order of the filter, M, equal to the order of an AR model then this equation describes an AR model (see equation 3.4:1) for the signal $x_n$.

The power spectrum of the input signal to the prediction-error filter can be determined from the filter coefficients. In order to show this, consider first the output of the prediction -filter which may be written as a polynomial in z:

$$P_e(z) = E(z)\, E(1/z^*)^* .$$

Now since $E(z) = A(z)\, X(z).$

(3.5:13)

$$P_e(z) = A(z)\, A(1/z^*)^*\, X(z)\, X(1/z^*)^* .$$

Now since the output signal is white, when $P_e(z)$ is evaluated on the unit circle it has a constant value which can be specfied as $\sigma^2$. Thus,

$$\sigma^2 = A(z)\, A(1/z^*)^*\, X(z)\, X(1/z^*)^* .$$

Note, however, that $X(z)\, X(1/z^*)^*$ is the z transform of the power of the input signal $P_x(z)$. Now solving for $P_x(z)$,

(3.5:14)

$$P_x(z) = \frac{\sigma^2}{A(z)\, A(1/z^*)^*} = \frac{\sigma^2}{|A(z)|^2}$$

Replace z with exp(-j 2π f k),

(3.5:15)

$$P_x(f) = \frac{\sigma^2}{\left| 1 + \sum_{k=1}^{M} a_k \exp(-j\, 2\pi f k) \right|^2}$$

Thus a method of determining the power spectrum of the signal $x_n$ is developed from the coefficients of the prediction-error filter.

### 3.6 Maximum Entropy Spectrum Estimation

In 1967, John Burg introduced his fundamental work entitled "Maximum Entropy Spectral Estimation" at the 37th Meeting of the Society of Exploration Geophysicists. This work started what has been described as a revolution in the field of spectral analysis (Robinson, 1982). Burg recognized that a windowed autocorrelation function (ACF) does not uniquely define a power spectrum (PS) and that there is in fact an infinite set of power spectra consistent with a windowed ACF. Therefore, additional information is required to choose the correct (or one particular) spectrum from the infinite set. Since no further information is provided, the PS that should be chosen is the one that corresponds to the most random time series which is consistent with the available ACF. This approach makes a minimum number of assumptions about the recorded data and therefore is in accordance with the principle of maximizing entropy. Maximum entropy (ME) spectral analysis involves finding the spectrum of the most unpredictable time-series whose autocorrelation coefficients are in agreement with the known set of values, determined from the recorded data (Robinson, 1982).

A simple example of the application of the ME principle to a problem of population estimation is presented in Appendix A. In this example it is shown that when no information is available the intuitive and correct solution to a problem requires making no assumption. The ME solution of the problem is in agreement with the intuitive solution.

A derivation of the method of ME PS analysis is now presented. This section follows a number of important references, Burg (1967), Ulrych and Bishop (1978), Lim and Malik (1981), Robinson (1982), Jaynes (1957, 1958, 1978, 1982), Malik *et al.* (1982), Haykin and Kesler (1983), Ulrych and Ooe (1983), Dudgeon and Mersereau (1984). The approach presented in this section is iterative and although it is presented with one dimensional signals it is applicable to multi-dimensional signal analysis (shown in section 3.8).

The explanation of the ME method starts with a restatement of the equation defining the power spectrum:

(3.6:1)

$$P(f) = \sum_{m=-\infty}^{\infty} R_{xx}(m) \exp(-j\, 2\pi\, f\, m) \qquad -\frac{1}{2} \leq f \leq \frac{1}{2}$$

where

P(f) is the PS of the process x(n),

$R_{xx}(m)$ is the ACF of the process x(n).

In most applications it is not possible to obtain an exact or complete ACF and an estimate of the ACF is normally used. Irrespective of the accuracy of the estimated ACF, it is only possible to estimate values of $R_{xx}(m)$ in the finite region, $|m| < N-1$, if the data, $x_n$, is available in the finite interval $0 < n < N-1$. When using classical methods of PS analysis, the ACF is assumed to be zero outside the region $|m| < N-1$, as discussed in section 3.3. On the other hand, in the ME method it is assumed that the segment of the ACF that is estimated from the data is exact but incomplete and through the application of the ME principle additional terms of the ACF are determined.

The ME PSE is defined as:

(3.6:2)

$$\text{ME PSE}(f) = \sum_{|m| \leq (N-1)} R_{xx}\text{^}(m) \exp(-j\, mf) + \sum_{|m| > (N-1)} R_{xx\_uk}(m) \exp(-j\, mf)$$

where

$R_{xx}$^(m) are ACF values estimated from the data,

$R_{xx\_uk}(m)$ are ACF values estimated by application of the ME principle.

The resolution of the ME PSE is increased over classical PSEs because the extent of the ACF is increased and the arbitrary assumption that the data is zero outside the measurement interval is removed.

The entropy, H, of a PSE is defined as:

(3.6:3)

$$H = \int_{-0.5}^{0.5} \ln(PSE(f))\, df$$

This definition for entropy is extensively used in PS analysis (Lim and Malik (1981), Robinson (1982), Haykin and Kesler (1983)), however, it is properly called the entropy rate. It has been shown that there are many different functions that may be described as entropy functions (Narayana and Nityananda, 1983) and maximizing any of these functions will produce similar results (See Appendix B for a short summary of this concept). The particular choice of the entropy function made here is for ease of computation. The results obtained by using this entropy function are similar to those obtained from the more conventional form for entropy ($H=-\sum p\ln(p)$).

The ME PSE is determined by maximizing H with respect to the unknown coefficients of ACF ($R_{xx\_uk}(m)$). Therefore the partial derivatives of H with respect to the unknown coefficients of the ACF are calculated and set equal to zero.

(3.6:4)

$$\frac{\partial H}{\partial R_{xx\_uk}} = 0$$

where

$R_{xx\_uk}$ are the unknown coefficients of the ACF.

The ACF coefficients which are not defined by the data, are determined by solving equations (3.6:4) and (3.6:2) simultaneously.

Substituting for H in equation (3.6:4)

(3.6:5)

$$\frac{\partial}{\partial R_{xx\_uk}} \left[ \int_{-0.5}^{0.5} \ln(PSE(f))\, df \right] = 0$$

then,

$$\int_{-0.5}^{0.5} \left[ \frac{\partial}{\partial R_{xx\_uk}} \left[ \ln (PSE(f)) \right] \right] df = 0$$

and then using the chain rule,

$$\int_{-0.5}^{0.5} \left[ \frac{1}{PSE(f)} \frac{\partial}{\partial R_{xx\_uk}} \left[ PSE(f) \right] \right] df = 0$$

From equation (3.6:2) for a particular $R_{xx\_uk}(m)$,

$$\frac{\partial PSE(f)}{\partial R_{xx\_uk}} = \exp(-j\, 2\pi\, f\, m).$$

Substituting this into equation (3.6:5)

(3.6:6)

$$\int_{-0.5}^{0.5} \left[ \frac{1}{ME\ PSE(f)} \exp(-j\, 2\pi\, f\, m) \right] df = 0$$

This equation can be interpreted as the Fourier transform of (1/(ME PSE)). (1/(ME PSE)) is called the inverse ME PSE (Robinson, 1982). Equation (3.6:6) is applicable for the terms $R_{xx\_uk}(m)$ which are not defined by the signal $x_n$ and thus it applies only in the region $|m| > N-1$.

The PSE of any process is by definition positive and therefore the inverse PSE is also positive. If it is assumed that the inverse PSE is bounded, it too can be viewed as a well-behaved PSE. It has an ACF associated with it which is called the inverse ACF and is denoted by ¥(n).

The Fourier transform of ¥(n) is of course (1/(ME PSE)).

(3.6:7)

$$\sum_{n=-\infty}^{\infty} \text{¥}(n) \exp(-j\, 2\pi\, f\, n) = \frac{1}{ME\ PSE(f)}$$

This equation now looks very similar to equation (3.6:6), except that (3.6:7) is a forward Fourier transform of ¥(n) and (3.6:6) is a forward Fourier transform of (1/(ME PSE)).

Replace n with -n in equation (3.6:7).

(3.6:8)

$$\sum_{n=\infty}^{-\infty} ¥(-n)\exp(\,j\,2\pi f n) = \frac{1}{\text{ME PSE(f)}}$$

If ¥(n) comes from a real process, then ¥(n) is real and even and ¥(-n) = ¥(n). The order of the summation in equation (3.6:8) can be reversed. Thus, this equation becomes a backward transform.

(3.6:9)

$$\sum_{n=-\infty}^{\infty} ¥(n)\exp(\,j\,2\pi f n) = \frac{1}{\text{ME PSE(f)}}$$

Changing the direction of the transform in equation (3.6:9),

(3.6:10)

$$\int_{-0.5}^{0.5} \frac{1}{\text{ME PSE(f)}}\exp(-j\,2\pi f n)\,df = ¥(n)$$

It is thus shown that equations (3.6:6) and (3.6:10) are equivalent and it is clear that ¥(n) = 0 for |n|>(N-1).

The ME PSE must be consistent with both equation (3.6:2) and equation (3.6:7). These equations can be written in a concise form:

(3.6:11)

$$\text{PSE(f)} = \text{FT}(R_{XX}(m))$$

(3.6:12)

$$\text{PSE(f)} = 1/\text{FT}(¥(n))$$

The constraints on these equations are:

For (3.6:11) $R_{xx}(m) = R_{xx}{}^\wedge(m)$ for $|m| \leq (N-1)$

For (3.6:12) ¥(n) = 0 for $|n| > (N-1)$

They may be written as a single equation:

(3.6:13)

$$FT\,(R_{xx}\,(m)) = 1/FT(¥(n))$$

An iterative algorithm for ME PS analysis has been developed by Lim and Malik (1981) which is based on equation (3.6:13). In figure 3.1 a simplified version of this algorithm is presented in the form of a flowchart. By appropriate selection of the initial estimates and gradual correction of $R_{xx}(m)$ and ¥(n), this algorithm has been shown to always converge.

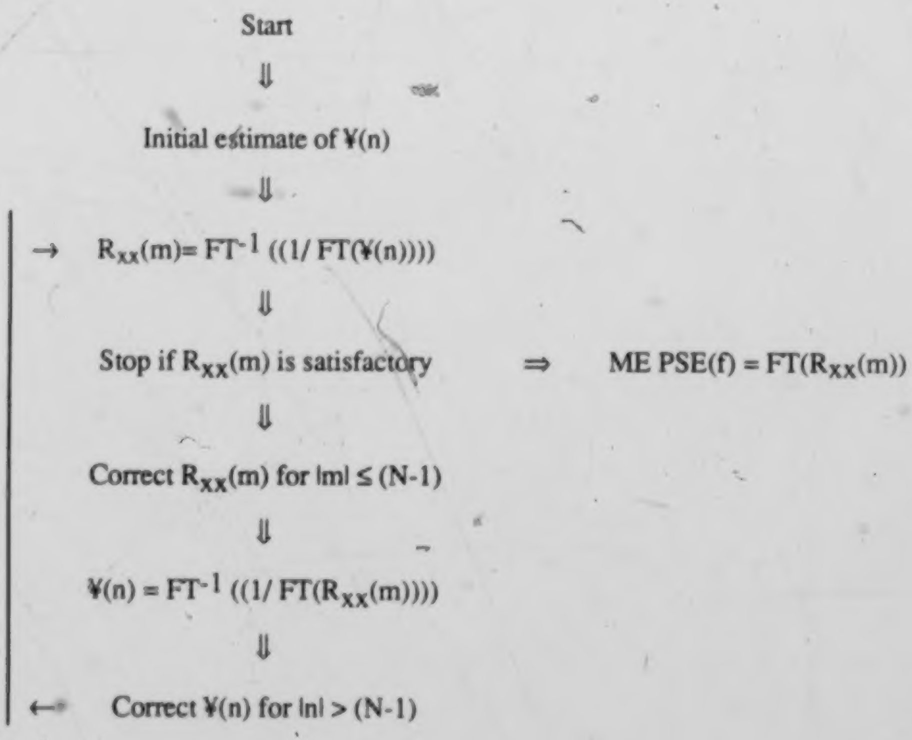
Start
Initial estimate of ¥(n)
$R_{xx}(m)= FT^{-1}\,((1/\,FT(¥(n))))$
Stop if $R_{xx}(m)$ is satisfactory
ME PSE(f) = $FT(R_{xx}(m))$
Correct $R_{xx}(m)$ for $|m| \leq (N-1)$
¥(n) = $FT^{-1}\,((1/\,FT(R_{xx}(m))))$
Correct ¥(n) for $|n| > (N-1)$

Figure 3.1 An iterative algorithm for ME PS analysis (Lim and Malik, 1981).

The algorithm can be applied to multidimensional PS analysis. A complete description of this algorithm for two-dimensional signal analysis is presented in section 3.8.

## 3.7 Equivalence of the Prediction-error and Maximum Entropy Power Spectrum Estimates

In this section it is shown that the PSE from the prediction-error filter is identical in form to the ME PSE for one dimensional signals. It generally follows work presented by Haykin and Kesler (1983). It has been shown in section 3.6 that the ME PSE has an inverse ACF, ¥, which is of finite extent. This is expressed mathematically as:

(3.7:1)

$$\frac{1}{\mathrm{ME\ PSE}(f)} = \sum_{n=-(N-1)}^{(N-1)} ¥(n) \exp(-j\ 2\pi\ f\ n)$$

Recalling the Wiener-Khintchine theorem, that the PS and the ACF are Fourier transform pairs, the ACF is equal to,

(3.7:2)

$$R_{xx}(m) = \frac{1}{2\pi} \int_{-0.5}^{0.5} P(f) \exp(j\ 2\pi\ f\ m)\ df$$

Substituting into equation (3.7:2) for P(f) with ME PSE(f),

(3.7:3)

$$R_{xx}(m) = \frac{1}{2\pi} \int_{-0.5}^{0.5} \frac{1}{\sum_{n=(N-1)}^{N-1} ¥(n) \exp(-j\ 2\pi\ f\ n)} \exp(j\ 2\pi\ f\ m)\ df$$

Set,

$$z = \exp(j\ 2\pi\ f) \qquad dz = j\ 2\pi \exp(j\ 2\pi\ f)\ df$$

so

$$df = \frac{dz}{j\,2\pi\,\exp(j\,2\pi\,f)} = \frac{dz}{j\,2\pi\,z}$$

Therefore,

(3.7:4)

$$R_{xx}(m) = \frac{1}{j\,4\pi^2} \oint \frac{z^m}{\sum_{n=-(N-1)}^{N-1} ¥(n)\,z^{-n}} \frac{dz}{z}$$

and,

$$R_{xx}(m) = \frac{1}{j\,4\pi^2} \oint \frac{z^{m-1}}{\sum_{n=-(N-1)}^{N-1} ¥(n)\,z^{-n}} dz$$

This is a contour integral and it is carried out over the unit circle in the z plane in a counter-clockwise direction. It can be shown that ¥ can be written as:

(3.7:5)

$$¥(z) = \sum_{n=-(N-1)}^{(N-1)} ¥(n)\,z^{-n} = G_M(z)\,G_M(1/z^*)^*$$

where

$$G_M(z) = \sum_{n=0}^{M} g_n\,z^{-n}$$

$$G_M(1/z^*)^* = \sum_{n=0}^{M} g_n^*\,z^{n}$$

This implies that the polynomial ¥(z) can be factored into two polynomials G(z) and G(1/z*)*, that have poles and zeros in reciprocal locations. This can be shown by doing a change of variable in ¥(z) and replacing z by (1/z*). The poles and zeros of ¥(1/z*) should be at reciprocal and conjugate locations to the poles and zeros of ¥(z). However, their locations do not change in this way. Consider:

(3.7:6)

$$\yen(1/z^*) = \sum_{n=-(N-1)}^{(N-1)} \yen(n)\left[\frac{1}{z^*}\right]^n = \sum_{n=-(N-1)}^{(N-1)} \yen(n)\,(z^*)^n$$

Substituting for n with -n,

$$\yen(1/z^*) = \sum_{n=-(N-1)}^{(N-1)} \yen(-n)\,(z^*)^n$$

But $\yen(n)^* = \yen(-n)$ for any autocorrelation function and making the summation in ascending order:

$$\yen(1/z^*) = \sum_{n=-(N-1)}^{(N-1)} \yen(n)^*\,(z^*)^n$$

Grouping the conjugated terms together.

(3.7:7)

$$\yen(1/z^*) = \left[\sum_{n=-(N-1)}^{(N-1)} \yen(n)\,z^n\right]^* = \left[\yen(z)\right]^*$$

From this equation it is observed that the poles and zeros of the function $\yen(1/z^*)$ are at conjugate but not necessarily in reciprocal locations to the poles and zeros of the function $\yen(z)$. This can only happen if the roots of $\yen(z)$ occur in pairs which are related by being reciprocal. Thus $\yen(z)=\yen(1/z^*)^*$.

Therefore $\yen(z)$ can be written as the product of two functions, G(z) whose poles and zeros are inside the unit circle, and $G(1/z^*)^*$ whose poles and zeros are outside the unit circle and are reciprocals of the poles and zeros of G(z).

Recall:

(3.7:4)

$$R_{xx}(m) = \frac{1}{j\,4\pi^2}\oint \frac{z^{m-1}}{\sum\limits_{n=-(N-1)}^{N-1} \yen(n)\,z^{-n}}\,dz$$

Substituting with $\Psi(z) = G(z)\,G(1/z^*)^*$,

$$R_{xx}(m) = \frac{1}{j\,4\pi^2} \oint \frac{z^{m-1}}{G(z)\ G(1/z^*)^*}\, dz$$

Now multiply on both sides by G(z) to get,

$$\sum_{k=0}^{M} g_k\, R_{xx}(m-k) = \frac{1}{j\,4\pi^2} \oint \frac{z^{m-1}}{G(z)\,G(1/z^*)^*}\ G(z)\ dz$$

Which can be written as,

(3.7:8)

$$\sum_{k=0}^{M} g_k\, R_{xx}(m-k) = \frac{1}{j\,4\pi^2} \oint \frac{z^{m-1}}{G(1/z^*)^*}\, dz$$

Now G(z) is defined as a polynomial with zeros inside the unit circle. $G(1/z^*)^*$ is defined as a polynomial with zeros outside the unit circle. Thus the RHS of the above equation is analytic on and inside the unit circle for $m \geq 1$. For $m=0$ there is a single pole at $z=0$. Now using the Cauchy's Residue theorem, the contour integral is zero for $m>0$ and is the residue for $m=0$. Therefore evaluating the RHS for $m=0$ at $z=0$.

(3.7:9)

$$\sum_{k=0}^{M} g_k\, R_{xx}(m-k) = \begin{cases} \dfrac{1}{2\pi\ g_0^*} & m = 0 \\ 0 & m \geq 1 \end{cases}$$

Now this equation is similar to the equation

(3.5:11)

$$\sum_{k=0}^{M} a_k\, R_{xx}(m-k) = \begin{cases} P_e & m = 0 \\ 0 & m = 1, 2, \dots M \end{cases}$$

This equation defines the prediction-error filter and is an autoregressive model for the signal $x_n$. Thus, the ME equations are only scalar multiples of the prediction-error filter equations if,

(3.7:10)

$$g_k = \frac{1}{2\pi \; g_0{}^{*} \, P_e} \, a_k$$

Recalling that $a_0 = 1$,

$$g_0 g_0{}^{*} = |\, g_0 |^2 = \frac{1}{2\pi \; P_e}$$

The similarity of these two sets of equations for determining the autocorrelation of $x_n$ implies that the PSE of the prediction-error filter and the ME method are the same for one dimensional signals. In two or more dimensions, however, some differences exist between these methods. This is due to the non-uniqueness of the prediction-error approach in multidimensional signal analysis. The analysis of multidimensional signals by the ME approach is discussed further in section 3.8.

## 3.8 A Description of the Lim and Malik Algorithm for Two dimensional Maximum Entropy Power Spectrum Estimation

The problem of power spectrum (PS) estimation of two dimensional signals arises in many fields such as, seismic signal processing (Woods, 1976), image processing (Andrews and Hunt, 1978), radar (McDonough, 1983) and sonar (Baggeroer, 1978). This problem has received considerable attention and a variety of techniques have been developed.

The technique for ME PS analysis for one dimensional signals has been shown to be equivalent to AR modeling by the least squares method. The least squares solution is theoretically tractable and computationally attractive however, it does not extend in a straight-forward manner to the analysis of two dimensional signals. Presently there are no methods that can provide an exact solution to the problem of multidimensional ME PS analysis. As suggested in section 3.6, however, the iterative method (figure 3.1) proposed by Lim and Malik (1981) can be used in spectral analysis of multi-dimensional signals.

In the absence of a closed form for the ME solution, it is important to know the conditions under which the ME solution exists and is unique. In this regard, Woods (1976) has shown that given an ACF in the region w, which is part of some positive definite (Fourier transform is positive for all frequencies) correlation function, a solution for the ME PSE exists and is unique.

The iterative method is now discussed further. The outline of the method that was presented in section 3.6 cannot be used directly to obtain ME PSE without some modification due to the problem of zero-crossings in the power spectrum. Specifically, the algorithm requires two inversions of the spectral estimates in each iteration, and thus the algorithm cannot continue if the PSE has a zero crossing at any stage of the iteration. Unfortunately, zero crossings can occur in two different ways in each iteration. One is the correction of the ACF and the other is the truncation of the inverse ACF. To see this, let $R_y{}^m$ represent the m^th^ estimate of the ACF and $¥^m$ represent the m^th^ estimate of the inverse ACF. Suppose that the following conditions hold:

(3.8:1)

$$FT(R_y{}^m) > 0 \qquad \text{for all frequencies}$$

$$FT(¥^m) > 0 \qquad \text{for all frequencies}$$

and

$$¥^m = FT^{-1}\left[\frac{1}{FT(R_y^m)}\right] w$$

where

$$w = \begin{bmatrix} 1 & \text{for known region of ACF} \\ 0 & \text{for all other regions} \end{bmatrix}$$

Similarly, let $¥^{m+1}$ and $R_y{}^{m+1}$ represent $¥$ and $R_y$ after the m+1th iteration. In the iterative algorithm of figure 3.1 $¥^{m+1}$ and $R_y{}^{m+1}$ are obtained from $¥^m$ by:

(3.8:2)

$$R'(m) = FT^{-1}\left[\frac{1}{FT(\gamma^{m}(n))}\right]$$

$$R_y^{m+1}(m) = R'(m) + (R_x(m) - R'(m))\, w(m)$$

$$\gamma'(n) = FT^{-1}\left[\frac{1}{FT\,(R_y^{m+1}(m))}\right]$$

and

$$\gamma^{m+1}(n) = \begin{cases} \gamma'(n) & \text{for known region} \\ 0 & \text{otherwise} \end{cases}$$

From these equations it is clear that R' is positive definite since $\gamma^m$ is assumed to be positive definite but $R_y^{m+1}$ may not be positive definite due to the window, w. Furthermore, even if $R_y^{m+1}$ were positive definite so that $\gamma'$ is positive definite, $\gamma^{m+1}$ may not be positive definite, again due to w.

To ensure that the resulting $R_y^{m+1}$ and $\gamma^{m+1}$ are positive definite so that the iterations can be continued, some modification are made. Specifically, $R_y^{m+1}$ is obtained by linearly interpolating between R' and the known values of the ACF, and $\gamma^{m+1}$ is obtained from linearly interpolating between $\gamma'$ and $\gamma^m$. In the modified algorithm, $\gamma^{m+1}$ and $R_y^{m+1}$ are obtained by:

(3.8:3)

$$R_y^{m+1}(m) = R'(m) + (1 - a_{m+1})(R_x(m) - R'(m))\, w(m)$$

and

$$\gamma^{m+1}(n) = \beta_{m+1}\, \gamma^{m}(n) + (\,1 - \beta_{m+1})\, \gamma'(n)\, w(n)$$

These equations reduce to those in figure 3.1 when $a_m=0$ and $\beta_{m+1}=0$. Any other choice of $a_m$ represents a non-ideal correction of R' with the known values of the ACF, and larger values of $a_m$ corresponding to more non-ideal corrections. With the appropriate choice of $a_m$, however, the resulting $R_y^{m+1}$ can be guaranteed positive definite. This can be seen by noting that since $¥^m$ and therefore R' are assumed to be positive definite, then by considering $a_m$ sufficiently close to 1, $R_y^{m+1}$ can be made arbitrarily close to R'. Similarly for $¥^m$, with any other choice for $\beta_m$ other than $\beta_m=0$, a non-ideal correction to $¥'$ is made, but it can be shown that with the proper choice of $\beta_m$, $¥^{m+1}$ can be guaranteed positive definite. Therefore, by choosing $a_m$ and $\beta_m$ in the ranges $0 \leq a_m < 1$, $0 \leq \beta_m < 1$, the spectral zero crossing problem can be avoided so that the iterations can be continued.

A flowchart of the Lim and Malik algorithm is presented here for two-dimensional signals and a list of symbols used in the flowchart is presented in table 3.1.

**Table 3.1 A list of the symbols used in figure 3.2.**

$a_m, \beta_m$ --- correction factors
k --- convergence factor
$E_0$ --- acceptable mean square error
$E_m$ --- mth mean square error
w --- window function which when applied to $R_{xx}$ produces the known portion of $R_{xx}$
$R_{xx}$ --- true ACF
R' --- estimate of ACF from current $¥^m$
$R_y{}^m$ --- mth estimate of the autocorrelation function after correcting R'
¥' --- estimate of inverse autocorrelation function from current $Ry^m$
$¥^m$ --- mth estimate of inverse autocorrelation function after correcting ¥'
$P_m$ --- Current estimate of power spectrum
$= FT(R_y{}^m)$ or
$= 1/FT(¥^m)$
$Q_m$ --- Current estimate of inverse power spectrum
$= 1/P_m$

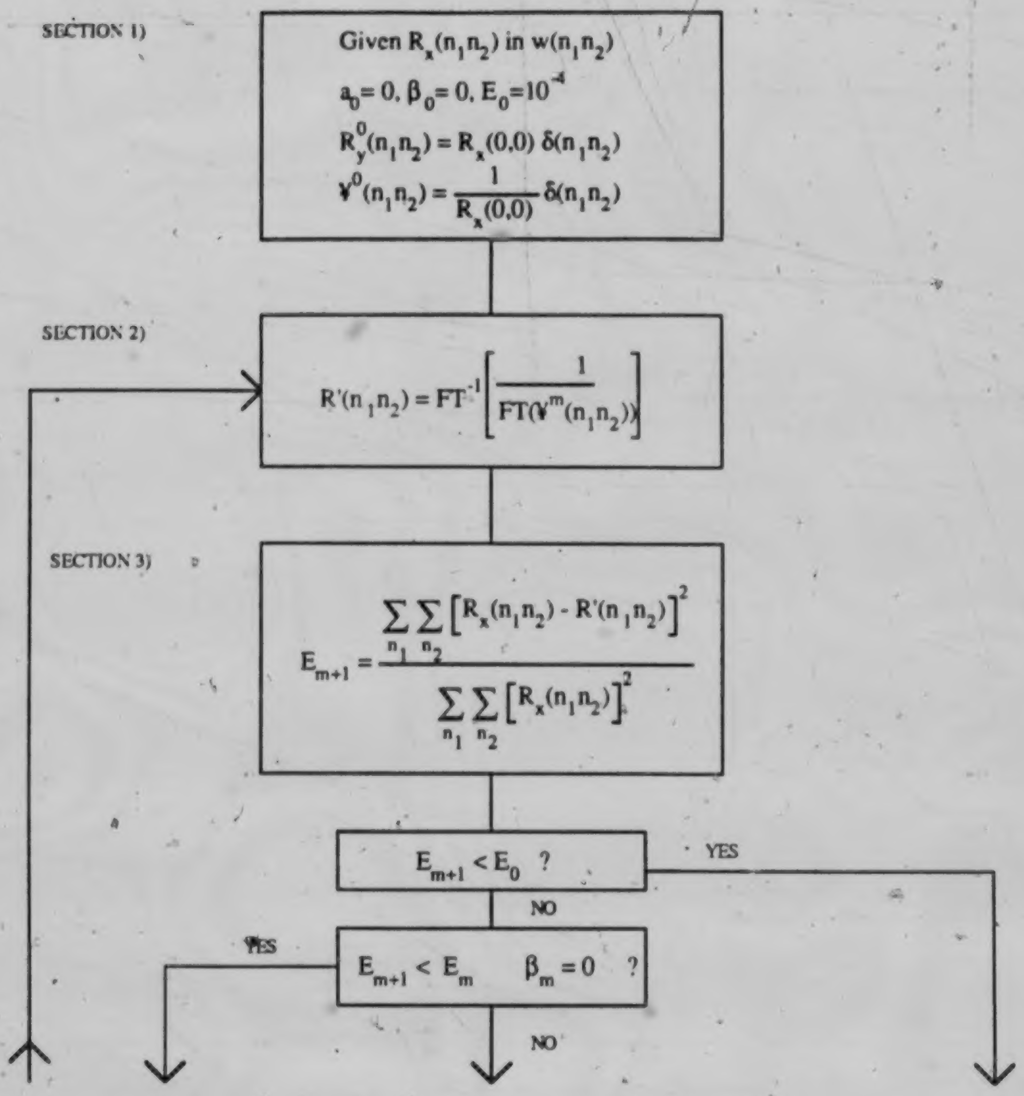
SECTION 1)
Given $R_x(n_1n_2)$ in $w(n_1n_2)$
$a_0 = 0,\ \beta_0 = 0,\ E_0 = 10^{-4}$
$R_y^0(n_1n_2) = R_x(0,0)\,\delta(n_1n_2)$
$\gamma^0(n_1n_2) = \frac{1}{R_x(0,0)}\,\delta(n_1n_2)$
SECTION 2)
$R'(n_1n_2) = FT^{-1}\left[\frac{1}{FT(\gamma^m(n_1n_2))}\right]$
SECTION 3)
$E_{m+1} = \frac{\sum_{n_1}\sum_{n_2}\left[R_x(n_1n_2) - R'(n_1n_2)\right]^2}{\sum_{n_1}\sum_{n_2}\left[R_x(n_1n_2)\right]^2}$
$E_{m+1} < E_0$ ?
YES
NO
YES
$E_{m+1} < E_m \quad \beta_m = 0$ ?
NO

Figure 3.2 Flowchart of the Lim and Malik algorithm for maximum entropy spectral estimation.

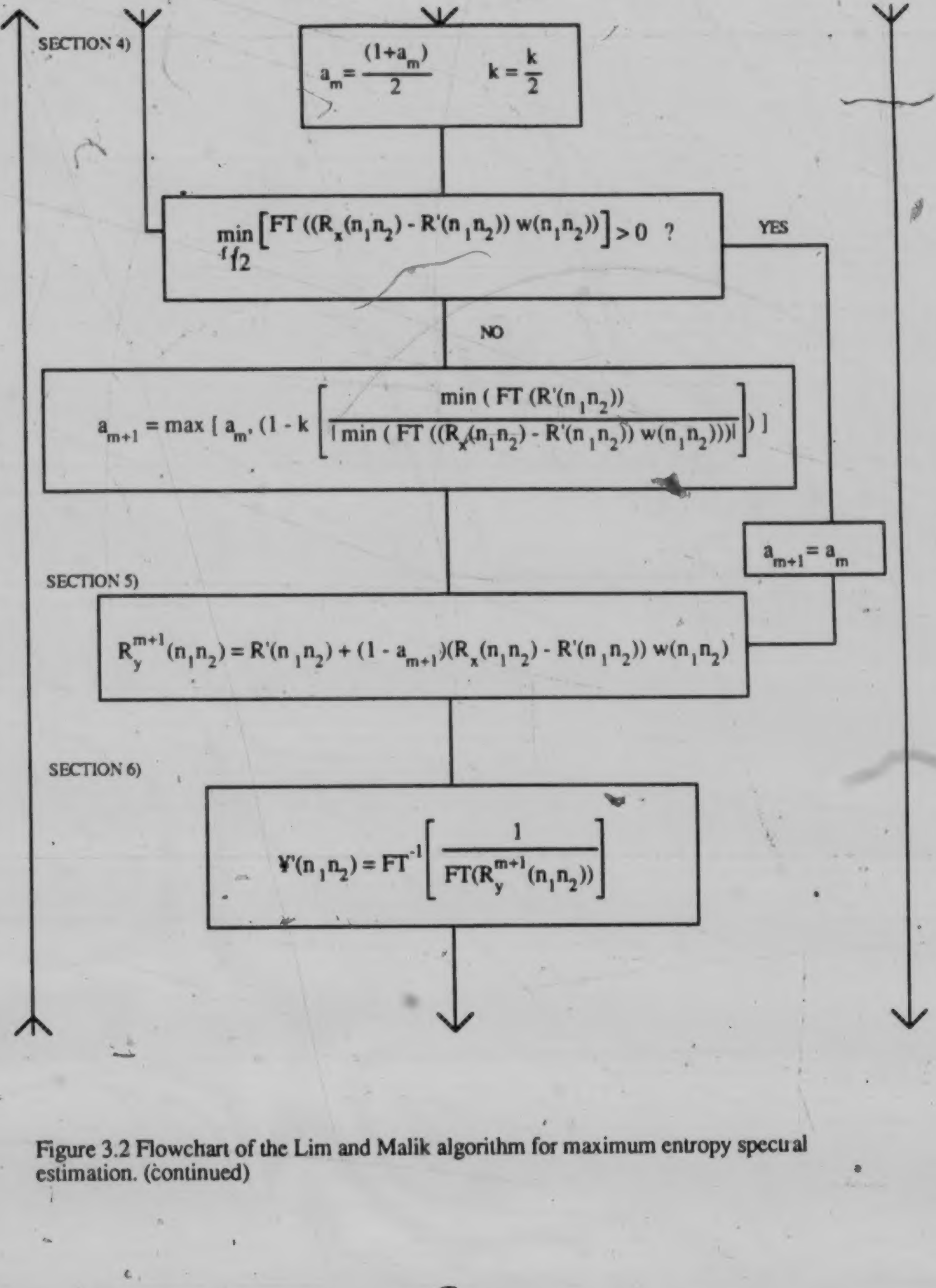
SECTION 4)
$a_m = \frac{(1+a_m)}{2}$
$k = \frac{k}{2}$
$\min_{f_1 f_2} \left[ FT\left((R_x(n_1 n_2) - R'(n_1 n_2))\, w(n_1 n_2)\right) \right] > 0$ ?
YES
NO
$a_{m+1} = \max\left[ a_m, \left(1 - k \left[ \frac{\min(FT(R'(n_1 n_2)))}{|\min(FT((R_x(n_1 n_2) - R'(n_1 n_2))\, w(n_1 n_2)))|} \right]\right) \right]$
$a_{m+1} = a_m$
SECTION 5)
$R_y^{m+1}(n_1 n_2) = R'(n_1 n_2) + (1 - a_{m+1})(R_x(n_1 n_2) - R'(n_1 n_2))\, w(n_1 n_2)$
SECTION 6)
$¥'(n_1 n_2) = FT^{-1}\left[ \frac{1}{FT(R_y^{m+1}(n_1 n_2))} \right]$

Figure 3.2 Flowchart of the Lim and Malik algorithm for maximum entropy spectral estimation. (continued)

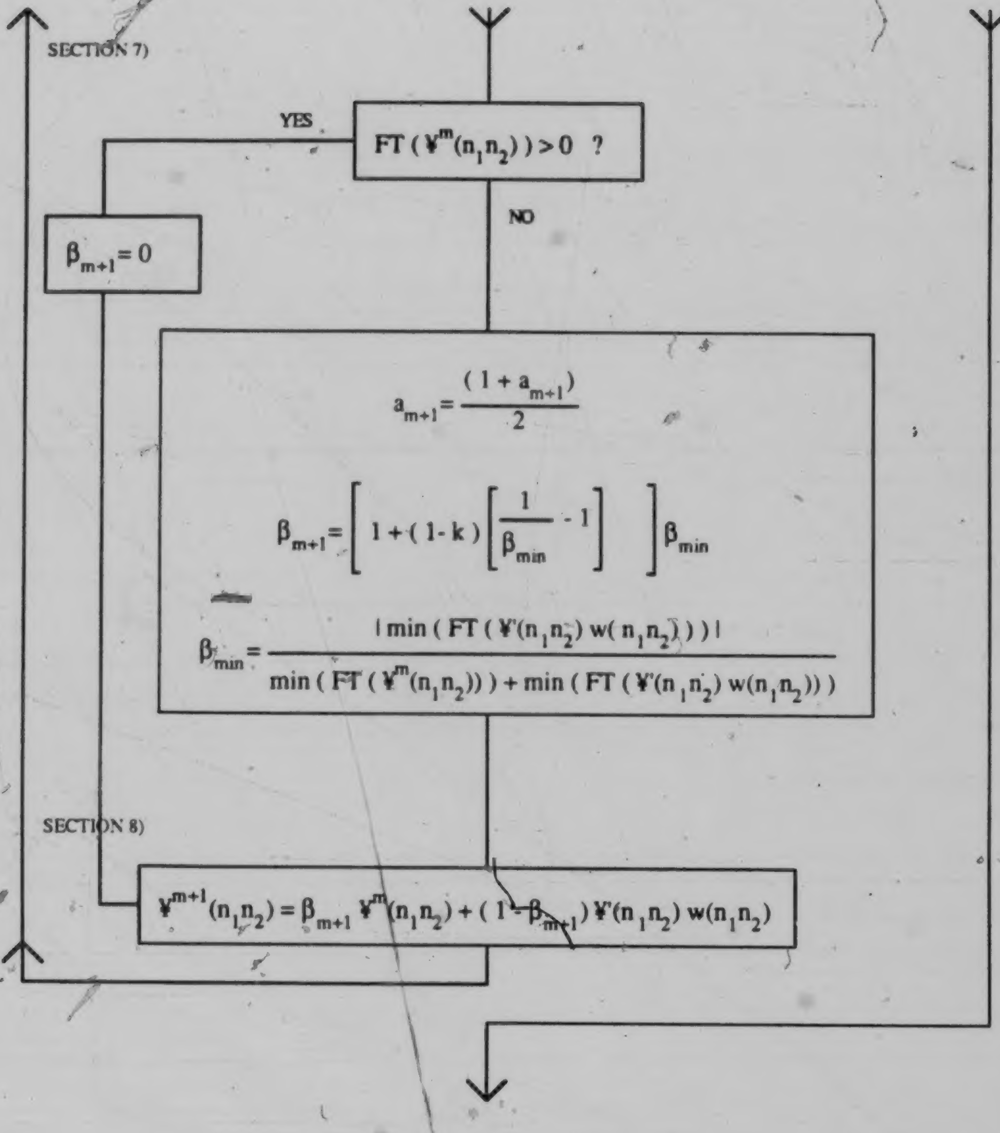
SECTION 7)
YES
FT ( ¥^m(n_1n_2) ) > 0 ?
NO
β_{m+1} = 0
a_{m+1} = (1 + a_{m+1}) / 2
β_{m+1} = [ 1 + ( 1 - k ) [ 1/β_min - 1 ] ] β_min
β_min = | min ( FT ( ¥'(n_1n_2) w( n_1n_2) ) ) | / ( min ( FT ( ¥^m(n_1n_2)) ) + min ( FT ( ¥'(n_1n_2) w(n_1n_2)) ) )
SECTION 8)
¥^{m+1}(n_1n_2) = β_{m+1} ¥^m(n_1n_2) + ( 1 - β_{m+1}) ¥'(n_1n_2) w(n_1n_2)

Figure 3.2 Flowchart of the Lim and Malik algorithm for maximum entropy spectral estimation. (continued)

SECTION 9)

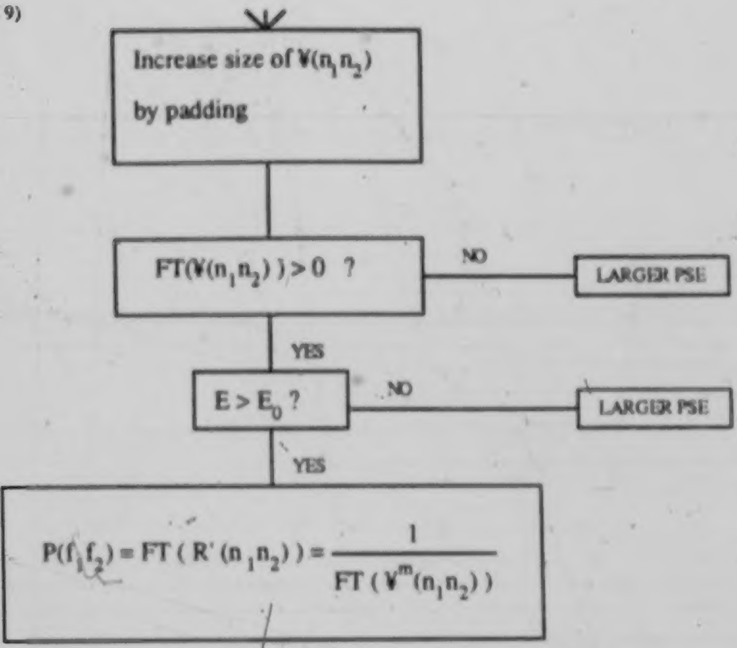
Increase size of ¥$(n_1 n_2)$ by padding
FT(¥$(n_1 n_2)$ ) > 0 ?
NO
LARGER PSE
YES
$E > E_0$ ?
NO
LARGER PSE
YES
$P(f_1 f_2) = FT(R'(n_1 n_2)) = \frac{1}{FT(¥^m(n_1 n_2))}$

Figure 3.2 Flowchart of the Lim and Malik algorithm for maximum entropy spectral estimation. (continued)

In this flowchart modifications for zero-crossings are included, as is a test for determining if the algorithm has converged. The algorithm, which has been divided into nine sections, is now discussed.

(Section 1) In this section of the algorithm, various parameters are initialized. The parameters are set to:

$$a_0 = 0,\ \beta_0 = 0,\ E_0 = 10^{-4},\ \yen^0(0,0) = 1/R_{xx}(0,0),\ k = 0.5$$

The inverse ACF, $\yen^0$, is non-zero only at (0,0) so that its FT, $Q_m$, is a constant. $P_m$ is therefore also a constant and is positive and the ACF, R', then is non-zero only at (0,0). The first estimates of $\yen^m$ and R' are positive definite and all subsequent estimates are made such that they remain positive definite.

(Section 2) In this section of the algorithm, the ACF, R', is estimated from the inverse ACF, $\yen^m$. The equation which relates these two functions is:

$$R' = FT^{-1}(\ 1/(FT(\yen^m))\ )$$

(Section 3) In this section of the algorithm, the important decision of when the algorithm has converged is made so that iterations can be stopped. It is considered that the algorithm has converged when the following condition is satisfied.

$$E_{m+1} = \frac{\sum_{n_1}\sum_{n_2}\left[\ R_x(n_1n_2) - R'(n_1n_2)\right]^2}{\sum_{n_1}\sum_{n_2}\left[R_x(n_1n_2)\right]^2} \le E_0$$

Clearly, if $E_{m+1}=0$ and R' is computed from $\yen^m$ using an infinite extent Fourier transform then the resulting solution corresponds to the ME PSE. However, due to the finite extent of R' and finite precision arithmetic used, it is not possible to reduce the error exactly to zero and a larger value must be used for $E_0$. When the current error level, $E_{m+1}$ gets below $E_0$ execution of the algorithm goes to section 9.

If $E_{m+1}$ is not below the acceptable level, then a test is performed to determine if $E_{m+1}$ is below the previous error level, $E_m$. In most cases $E_{m+1}<E_m$ and execution goes to

section 4. If $E_{m+1}>E_m$, $a_{m+1}$ is increased to $(1+a_m)/2$ and k is decreased to k/2. This reduces the rate of convergence of the algorithm. Section 4 is then executed.

(Section 4) In this section of the algorithm, the correction factor, $a_{m+1}$, is determined. There are two conflicting criteria that must be considered when choosing the correction factor. The first is to choose as small a factor as possible, so that R' converges quickly to $R_{xx}$. The second is to use a large correction factor (which is less than one), so that the corrected estimate of the ACF, $R^{m+1}$, remains positive definite.

If FT(R' w) > FT($R_{xx}$ w) then the correction factor is not changed. If FT(R' w) < FT($R_{xx}$ w) then the algorithm is converging too rapidly and the value for $a_{m+1}$ must be changed. The method of selecting the correction factor requires consideration of how the corrected ACF estimate, $R_y^{m+1}$, is calculated from the current estimate, R'. This is done in section 5.

(Section 5) In this section of the algorithm, $R_y^{m+1}$ is calculated as a linear combination of R' and $R_{xx}$ in the region defined by w and is R' outside the region defined by w. The correction to $R_y^{m+1}$ is described by:

$$R_y^{m+1} = \left[\begin{array}{ll} R'(n_1 n_2) & \text{for } n_1 n_2 \text{ not in } w \\ a_{m+1}(R'(n_1 n_2)) + (1-a_{m+1})\,(R_{xx}(n_1 n_2)) & \text{for } n_1 n_2 \text{ inside of } w \end{array}\right.$$

This equation can be rewritten as:

$$R_y^{m+1} = R' - R'\,w + R_{xx}\,(1-a_{m+1})\,w + R'\,a_{m+1}\,w$$

$$R_y^{m+1} = R' + (-R' + R'\,a_{m+1})\,w + R_{xx}(1-a_{m+1})w$$

$$R_y^{m+1} = R' - R'\,(1-a_{m+1})\,w + R_{xx}(1-a_{m+1})\,w$$

$$R_y^{m+1} = R' + (1-a_{m+1})\,(R_{xx} - R')\,w$$

Now, $a_{m+1}$ is determined as follows:

For $R_y^{m+1}$ to be positive definite, $FT(R_y^{m+1}) > 0$.

$$FT(R') + (1-a_{m+1}) FT( (R_{xx} - R')w) > 0$$

$$\therefore$$

$$| FT ( R') | > (1-a_{m+1}) | FT ( (R_{xx} - R' )w) |$$

$$| FT ( R') | / | FT ( (R_{xx} - R' )w) | > (1-a_{m+1})$$

$$-1 + | FT ( R') | / | FT ( (R_{xx} - R' )w) | > - a_{m+1}$$

$$\therefore$$

$$a_{m+1} > 1 - \{ | FT ( R') | / | FT ( (R_{xx} - R' )w) | \}$$

This equation defines the smallest value of $a_{m+1}$ that can be used for $R_y^{m+1}$ to remain positive definite. In the algorithm of Lim and Malik, $a_{m+1}$ is defined as:

$$a_{m+1} = 1 - \{\min | FT ( R') | / | \min( FT ( (R_{xx} - R' )w) ) | \}.$$

The smallest value of FT(R') and the smallest negative value of $FT(R_{xx}-R')$ are used in calculating $a_{m+1}$. These extrema will, in general, occur for different $(n_1, n_2)$. However, the use of these terms does insure that the $a_{m+1}$ is larger than that defined previously and is a safe value for $a_{m+1}$. This choice is, however, at the expense of rapid convergence.

Returning to the calculation of the $a_{m+1}$, it is defined in the algorithm by:

$$a_{m+1} = \max \left[ a_m, \left(1 - k \left[ \frac{\min ( FT (R'(n_1 n_2))}{| \min ( FT ((R_x(n_1 n_2) - R'(n_1 n_2)) w(n_1 n_2)))|} \right]\right) \right]$$

The k term is described as an additional convergence factor and is, in fact, empirical. It makes $a_{m+1}$ even larger than the minimum value defined previously. It also results in a decrease in the speed of convergence.

(Section 6) In this section of the algorithm, the inverse ACF, ¥', is estimated. This section is similar to section 2 but R' and ¥' are interchanged and ¥' is determined as:

¥' $= FT^{-1}( 1/FT(R_y^{m+1}) )$

(Section 7) In this section, the correction factor for $¥^{m+1}$, $\beta_{m+1}$, is calculated. As in section 4 one must study how $¥^{m+1}$ is calculated before one can see how $\beta_{m+1}$ is calculated. This is done in section 8.

(Section 8) In this section $¥^{m+1}$ is determined using:

$$¥^{m+1} = ¥^{m}\,(\beta_{m+1}) + (1-\beta_{m+1})\,¥'\,w$$

If $\beta_{m+1} = 0$ then $¥^{m+1}$ is $¥^{m}$ multiplied by a window function. This satisfies the constraint that the inverse ACF is a spatially limited function (see equation (3.6:12)). $\beta_{m+1}$ is made non-zero only if ¥' is not positive definite. If $\beta_{m+1}$ is set equal to 1, then the previous estimate, $¥^{m}$, is used as $¥^{m+1}$ and execution of the algorithm is set back one iteration. However, the $a_{m+1}$ term is now smaller and a new inverse ACF is calculated.

As with the determination of $a_{m+1}$ the determination of $\beta_{m+1}$ depends on the associated ACF, in this case $¥^{m+1}$. Recall that:

$$¥^{m+1} = ¥^{m}(\beta_{m+1}) + ¥'\,(1-\beta_{m+1})\,w$$

In order that $¥^{m+1}$ be positive definite.

$$\beta_{m+1}\,|\,FT\,(¥^{m})\,| > (1-\beta_{m+1})\,|\,FT\,(¥'\,w)\,|$$

$$\frac{|\,FT\,(¥^{m})\,|}{|\,FT\,(¥'\,w)\,|} > \frac{(1-\beta_{m+1})}{\beta_{m+1}}$$

$$\frac{|\,FT\,(¥^{m})\,|}{|\,FT\,(¥'\,w)\,|}\,\beta_{m+1} > (1-\beta_{m+1})$$

$$\left[\frac{|\,FT\,(¥^{m})\,|}{|\,FT\,(¥'\,w)\,|} + 1\right]\beta_{m+1} > 1$$

$$\beta_{m+1} > \frac{|\,FT\,(¥'\,w)\,|}{|\,FT\,(¥'\,w)\,| + |\,FT\,(¥^{m})\,|}$$

This defines the smallest $\beta_{m+1}$ that can be used in the prediction or correction of $¥^{m+1}$. However in the algorithm the following is used:

$$\beta_{m+1} = \left[ 1 + (1 - k)\left(\frac{1}{\beta} - 1\right) \right] \beta$$

where

$\beta$ is the $\beta_{m+1}$ that was defined above.

Thus the $\beta_{m+1}$ which is actually used in the algorithm is larger than that required and the rate of convergence is slowed. From the new estimate of ¥$^{m+1}$, a new R' can be estimated and the algorithm can be continued in this cyclic fashion.

The algorithm is executed through these eight sections until the error, $E_{m+1}$ decreases to below an acceptable level $E_0$ at which point execution jumps to section 9.

(Section 9) This section is executed when the current error, $E_{m+1}$, is smaller than the acceptable error, $E_0$. The current inverse ACF, ¥', is padded so that its dimensions are doubled and its FT is calculated. This is used as a test for positive definiteness. The FT of the padded ¥' has a higher density of samples in the frequency domain than the unpadded function and zero crossings in between the frequency samples of the unpadded function may be detected by this procedure. If no zero crossings are found, the PSE associated with the inverse ACF is considered to be the maximum entropy power spectrum. If however zero crossings are found, the extent of the PSE used is not adequate and the algorithm must be executed again with a larger extent PSE.

This is a detailed description of the Lim and Malik algorithm. However, to really appreciate its mechanics one must be intimately familiar with the maximum entropy method as well as Fourier transform theory.

Lim and Malik (1981) state that they have empirically observed that the ACF, R', eventually converges to $R_{xx}$ if $R_{xx}$ is part of a true ACF. However, when estimating ACFs from data, one is never sure that the estimate $R_{xx}$ is part of a true ACF. Thus, if the execution does not result in convergence of R' to $R_{xx}$ then it may be concluded that the $R_{xx}$ provided was not part of a valid ACF.

### 3.9 Statistical Properties

Since the ME spectral estimator is non-linear, it is in general not possible to obtain an analytic expression for its statistical properties. This is one of the major shortcomings of the non-linear techniques of PS analysis. However, the asymptotic properties of the ME have been determined (Ulrych and Bishop, 1975) and can be compared to those of the classical estimators. It has been shown that the ME spectral estimator is asymptotically normal and unbiased (Haykin and Kesler, 1983). In other words, when both the number of samples, N, and the order of the filter, M, are sufficiently large, then:

(3.9:1)

$$E[\text{ME PSE}] = P_{True}$$

$$\text{Var}\,[\text{ME PSE}] = (v/2)P^2_{True}$$

where

$P_{True}$ is the actual PS of the process,

E is the expectation operator,

$v$=N/M.

These asymptotic expressions are of the same form as expressions for the mean and variance of the BA spectral estimate (discussed in section 3.3) and they are valid if the spectral estimate is reasonably smooth.

### 3.10 Conclusions

This chapter discusses both classical and modern methods of spectral estimation. The short-comings of the classical methods are that the variance of these estimators can only be reduced if increased bias is accepted and that the classical methods require unjustifiable assumptions to be made about the data not in evidence. The modern methods of spectral analysis on the other hand, assume a model for the recorded data and avoid assumptions about data that is unavailable. Of the modern methods considered, the ME method appears to be most suitable to the analysis of EEG topographic maps. The ME approach is shown to be equivalent to AR modelling for one-dimensional signals and it extends logically from one to two dimensions. The bias and variance of the ME PS estimator is shown to be asymptotically equivalent to that of the classical spectral estimators.

# Chapter 4

# Bartlett, Blackman-Tukey and Maximum Entropy Power Spectrum Estimates of Simulated Data

## 4.0 Introduction

The theoretical bases of the Bartlett (BA), Blackman-Tukey (BT) and maximum entropy (ME) methods of power spectrum estimation have been discussed in Chapter 3. These methods are now applied to simulated data of known power spectra (PS). The power spectrum estimates (PSEs) thus obtained are compared with the true PS to determine the applicability of these methods to actual EEG data.

## 4.1 Methods

The simulated data used in these tests was made up of a deterministic sinusoidal process and Gaussian white-noise. The sinusoidal process was defined in terms of spatial frequency components, $f_1$ and $f_2$ indicating frequencies in the lateral and sagittal directions respectively. Frequencies were normalized to the sampling rate so that a sinusoidal signal of wavelength equal to the distance between sample points had a frequency of unity.

The simulated data, $x(n_1, n_2)$, was defined by,

(4.1:1)

$$x(n_1, n_2) = \sum_{i=1}^{M} a_i \sin(2\pi f_{1i} n_1 + 2\pi f_{2i} n_2 + \phi_i) + b\,N(n_1, n_2)$$

where

$a_i$ is the amplitude of the $i^{th}$ sinusoid,

b is the amplitude of the noise process,

$n_1$, $n_2$ are orthogonal spatial variables,

$\phi_i$ is the phase angle of the ith sinusoid, N is a Gaussian white-noise process of zero mean and unit variance,

M is the number of sinusoids in the data set.

PSEs of real, 2-dimensional signals (such as $x(n_1, n_2)$) are radially symmetric about the origin. The PSE of an infinite-extent sinusoidal wave, for example, contains two impulse functions located at a distance of 2π/wavelength from the origin and oriented at the angle of the wave (ie. $\tan^{-1}(f_2/f_1)$ from the horizontal).

In most practical situations the amount of data available for PS estimation is limited by physical constraints. This can be modelled by an infinite-extent signal multiplied by a finite window function. PSEs from a limited amount of data are naturally affected by the window function. In the case of a sinusoidal signal, the impulse functions in the PSE are convolved with the point spread function associated with the window producing peaks of finite width. In the results presented in this chapter the data size was limited to 5x5 which represents an acceptable number of samples from a topographic map.

PSEs are also affected by the noise level in the data. The noise level was defined here by the signal-to-noise ratio (SNR):

(4.1:2)

$$\mathrm{SNR} = 20 \log \left[ \frac{\sum_{i=1}^{M} a_i}{b} \right]$$

As the SNR decreases the background level of the PSE increases and peaks in the PSE become more difficult to identify. Malik *et al.*, (1982) have studied the properties of two dimensional ME PSEs. They observed that an increase in the noise level also results in an increase in the width of the peaks in the ME PSE.

A standard technique for reducing variance in PS estimation is to average over a number of independent data sets (Oppenheim and Schafer, 1975 p. 548). This reduces the effect of noise and thus refines or smooths the PSE. Each PSE of simulated data in these tests was averaged over 15 independent data sets each with fixed SNR.

The array size of the PSEs in these simulations was 64x64. A common array size for all PSEs was used to facilitate comparison of the results. This 64x64 size was adopted because PS estimation requires the calculation of the DFT. This is most efficiently done via the FFT algorithm which requires the dimensions of the PSEs to be an integer power of 2. The PSEs presented here are therefore quantized at intervals of (1/64, 1/64), ie. (0.0156, 0.0156).

As discussed in Chapter 3, the BA PSE is calculated directly from the data while the BT and ME PSEs are calculated from an ACF that is first estimated from the data. The size of the ACF estimate used for these tests was 7x7. The ACF was estimated using:

(4.1:3)

$$\mathrm{ACF}(m_1\ m_2) = \frac{1}{N_1 - m_1}\ \frac{1}{N_2 - m_2} \sum_{n_1=m_1}^{N_1-1} \sum_{n_2=m_2}^{N_2-1} x(n_1\ n_2)\ x(n_1-m_1\ n_2-m_2)$$

where

$m_1$, $m_2$ are orthogonal spatial variables in the correlation domain.

The ME PSE was calculated using the Lim and Malik algorithm which was presented in Chapter 3. The ME PSE was determined after 30 iterations of the algorithm as there was little change in the PSE during the final iterations of the algorithm.

## 4.2 Results

### 4.2.1 BA, BT and ME PSEs

In figure 4.1 greylevel plots of PSEs obtained using the BA, BT, and ME methods are presented. They were produced from a simulated sinusoidal signal of frequency (0.15, -0.15) with no noise component. These plots show the base band of the frequency domain, that is, the horizontal axis indicates frequencies in the lateral direction from -0.5 to +0.5 and the vertical axis indicates frequencies in the sagittal direction from -0.5 to +0.5.

The origin of the PSE is in the center of the plot. The highest point in the PSE is normalized to 0 dB and is indicated by white. The region between 0 dB and -3 dB is black and the region below -3 dB is grey. It is observed that the -3 dB contour around each peak is approximately circular for the BA and BT PSEs. The 0 dB to -3 dB region for the ME PSE is so small that quantization in the frequency domain distorts its shape. Figures 4.2, 4.3, 4.4 are 3-dimensional wireframe views of the PSEs. This type of view provides an overall picture of the PSEs.

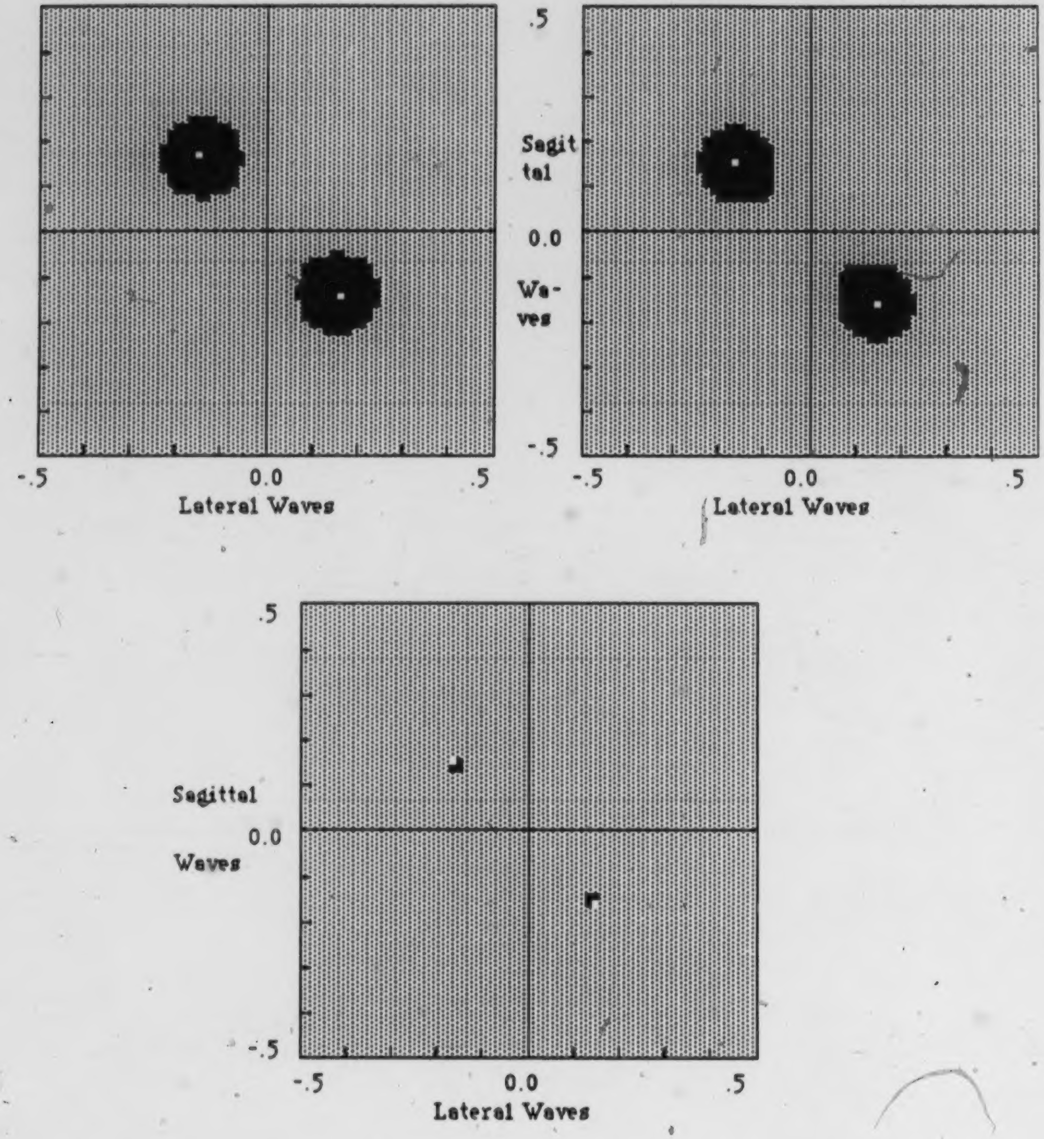

Figure 4.1 Greylevel view of the BA, BT and ME PSEs. Zero dB is indicated by white, <0 dB to -3 db is indicated by black and <-3 dB is indicated by grey.

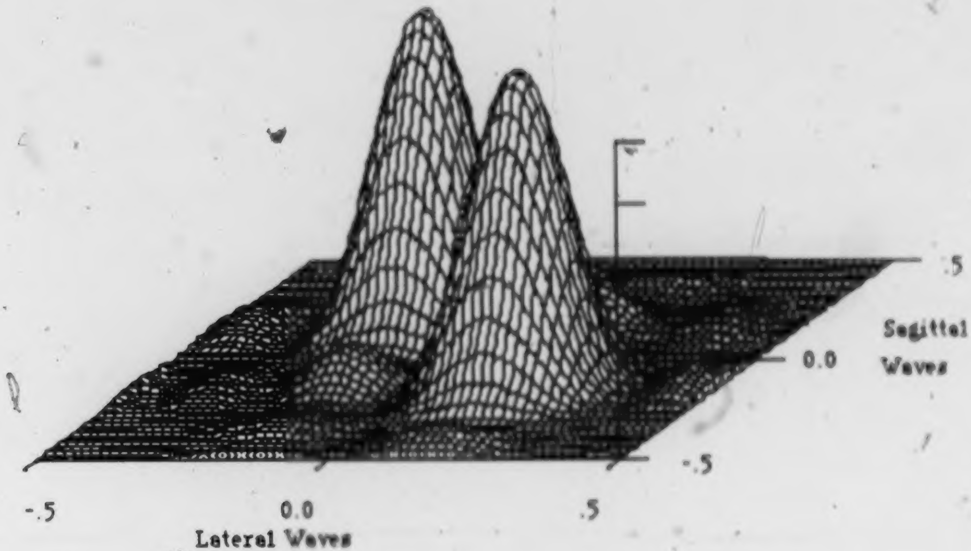

Figure 4.2 Three-dimensional wireframe view of a BA PSE for sinusoidal signal (0.15, -0.15) on a 5x5 data grid with no noise.

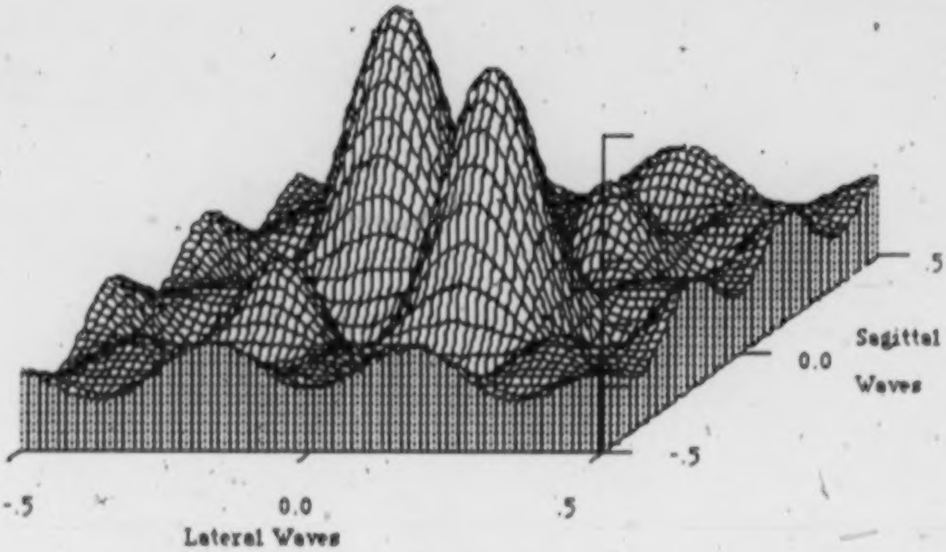

Figure 4.3 Three-dimensional wireframe view of a BT PSE for sinusoidal signal (0.15, -0.15) on a 7x7 ACF and no noise.

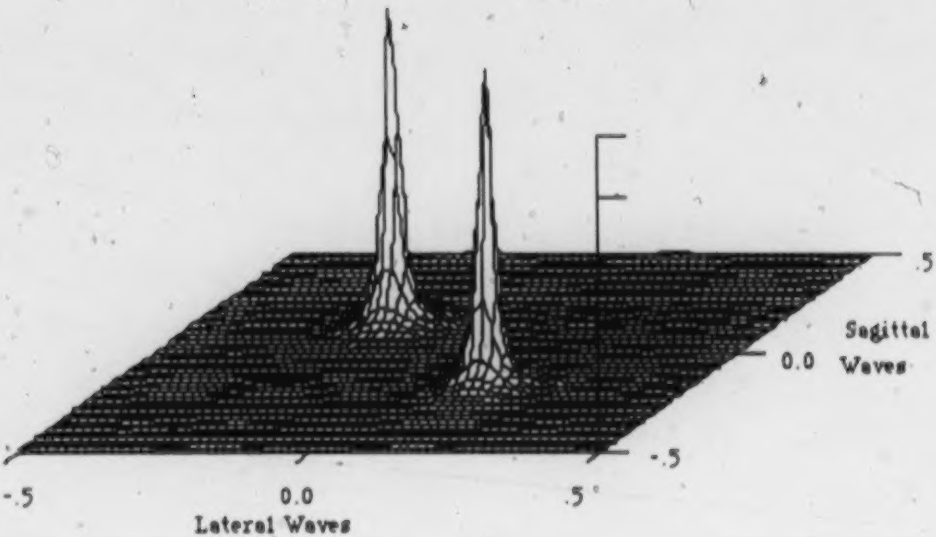

Figure 4.4 Three-dimensional wireframe view of a ME PSE for sinusoidal signal (0.15, -0.15) on a 7x7 ACF and no noise.

### 4.2.2 Effects of Frequency

The effect of the frequency of the simulated signals on peaks in the PSE was considered. PSEs were analyzed in terms of peak-position, defined as the location of the highest point in the PSE, and peak-width, defined as the radius of a circle of area equal to the -3 dB contour around a 0 dB peak in the PSE.

The results of BA, BT and ME PS analysis are summarized in table 4.1. The table is divided into four sections. In the first section the results of PS analysis of a constant value data set are presented. The second and third sections deal with signals in purely the lateral and sagittal directions respectively. The fourth section presents results for signals with equal components in both the lateral and sagittal directions. The simulated data used for this table was free of noise.

From table 4.1 it is observed that the peak-widths are consistently largest in BA PSEs, followed by those in BT PSEs and they are smallest in ME PSEs. The errors in peak-position are generally small (near quantization level). However, a pattern of error in peak-position is observable from table 4.1. The largest error in peak-position occurs for sinusoidal signals with frequencies close to the origin or the folding frequency (sampling frequency divided by two) of the PSE. For example, the BA and BT PSEs of the sinusoidal signal (0.075, 0.0) have a peak-position of (0.0, 0.0) The error in peak-position is due to the large peak-width associated with these methods of PS estimation. The constructive interference of the 'mirror' peaks (at (0.075, 0.0), (-0.075, 0.0)) in these PSEs produced the large, 'false' peak at the origin. Similar effects are observed in the BA PSE for the sinusoid (0.425, 0.0) in which the peak-position in the estimate is (0.5, 0.0).

Figure 4.5 summarizes the results in table 4.1. It shows an outline of the base band of a PSE and indicates the regions in which the interference between 'mirror' peaks causes errors in peak-position. The size of the special regions in figure 4.5 may be estimated from table 4.1. The size appears to be related to the method of PS estimation used and is

## Table 4.1

Results of PS analysis of sinusoidal signals using the BA, BT, and ME methods.

| Orient. | True Freq. (Lat, Sag) | Method (BA/ BT/ ME) | Peak-position (Lat, Sag) | Peak-width |
|---|---|---|---|---|
| Constant value | (0.000,0.000) | BA | (0.000,0.000) | 0.065 |
| | | BT | (0.000,0.000) | 0.062 |
| | | ME | (0.000,0.000) | 0.009 |
| Lateral | (0.075,0.000) | BA | (0.000,0.000) | 0.083 |
| | | BT | (0.000,0.000) | 0.073 |
| | | ME | (0.078,0.000) | 0.018 |
| | (0.175,0.000) | BA | (0.172,0.000) | 0.091 |
| | | BT | (0.172,0.000) | 0.083 |
| | | ME | (0.172,0.000) | 0.009 |
| | (0.425,0.000) | BA | (0.500,0.000) | 0.073 |
| | | BT | (0.500,0.000) | 0.068 |
| | | ME | (0.422,0.000) | 0.015 |
| Sagittal | (0.000,0.075) | BA | (0.000,0.000) | 0.083 |
| | | BT | (0.000,0.000) | 0.073 |
| | | ME | (0.000,0.078) | 0.018 |
| | (0.000,0.175) | BA | (0.000,0.172) | 0.088 |
| | | BT | (0.000,0.172) | 0.082 |
| | | ME | (0.000,0.172) | 0.009 |
| | (0.000,0.425) | BA | (0.000,0.500) | 0.083 |
| | | BT | (0.000,0.500) | 0.073 |
| | | ME | (0.000,0.422) | 0.018 |
| Lateral & Sagittal | (0.075,0.075) | BA | (0.063,0.063) | 0.089 |
| | | BT | (0.063,0.063) | 0.086 |
| | | ME | (0.078,0.078) | 0.009 |
| | (0.175, 0 175) | BA | (0.172,0.172) | 0.095 |
| | | BT | (0.172,0.172) | 0.089 |
| | | ME | (0.172,0.172) | 0.009 |
| | (0.425,0.425) | BA | (0.422,0.422) | 0.097 |
| | | BT | (0.422,0.422) | 0.089 |
| | | ME | (0.422,0.422) | 0.009 |

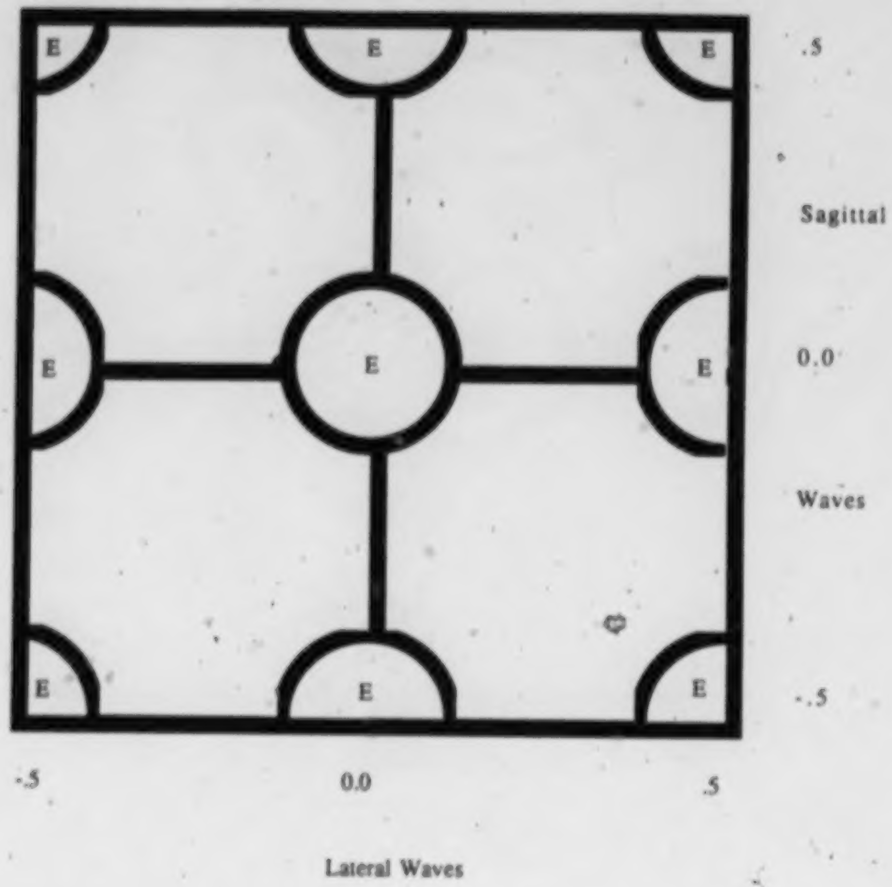
E
E
E
E
E
E
E
E
E
.5
Sagittal
0.0
Waves
-.5
-.5
0.0
.5
Lateral Waves

Figure 4.5 Base band of the 2-dimensional PSE with the special regions (E) where larger error in peak-position occur indicated.

approximately equal to the peak-width. Average values of the peak-widths from table 4.1 are: 0.086 for BA PSEs, 0.078 for BT PSEs, and 0.012 of the ME PSEs.

### 4.2.3 Identification of Two Sinusoids

To determine how well the frequencies of two different sinusoidal signals can be predicted from the PSEs a set of simulations was performed. The special regions of the frequency domain (figure 4.5) where errors occur in the PSE were not considered. The three methods of PS estimation (BA, BT, ME) were again used. The sinusoids in the simulated data sets had frequency components of equal magnitude in the lateral and sagittal directions. As the true position of the peak was known, identification of the peaks was based on visual detection.

Table 4.2 presents a summary of results of this analysis. The first column of table 4.2 indicates the true frequencies of the sinusoidal signals in the simulated data. The next column indicates the method of PS estimation used and the third column presents the frequencies at the positions of the peaks in the PSEs. In order to further emphasize the distinctness of the peaks in the PSE an additional criterion was used. The column labelled '3 dB distinct' indicates that the trough between the two peaks in the PSE was at least 3 dB down from the lower of the two peaks.

The results presented in table 4.2 begin with sinusoids widely separated in frequency and the separation in frequency is gradually decreased through the table. When the two sinusoids are widely separated in frequency two distinct peaks appear clearly in the PSE. As the frequency separation decreases the two peaks in the PSE begin to interfere with each other. Below a minimum separation of the frequencies the peaks in the PSE merge and produce a single 'false' peak.

Table 4.2 shows that the PSE of the BA method has '3 dB distinct' peaks for sinusoids separated in frequency by 0.20. The PSE of the ME method has '3 dB distinct' peaks for sinusoids separated in frequency by 0.125. It is interesting to note that this

## Table 4.2

The results of PS analysis of two sinusoidal processes on a uniform grid using the BA, BT and ME methods (frequency separation 0.200 - 0.075)

| True Freq. (Lat, Sag) | Method ( BA/ BT/ ME) | Peak-position (Lat, Sag) | 3 dB Distinct (T/F) |
|---|---|---|---|
| (0.100,0.100)<br>(0.300,0.300) | BA | (0.094,0.094)<br>(0.297,0.297) | T |
| | BT | (0.094,0.094)<br>(0.297,0.297) | T |
| | ME | (0.094,0.094)<br>(0.297,0.297) | T |
| (0.100,0.100)<br>(0.275,0.275) | BA | (0.109,0.109)<br>(0.281,0.281) | F |
| | BT | (0.109,0.109)<br>(0.281,0.281) | T |
| | ME | (0.094,0.094)<br>(0.281,0.281) | T |
| (0.100,0.100)<br>(0.250,0.250) | BA | (0.109,0.109)<br>(0.234,0.234) | F |
| | BT | (0.109,0.109)<br>(0.234,0.234) | T |
| | ME | (0.094,0.094)<br>(0.234,0.234) | T |
| (0.100,0.100)<br>(0.225,0.225) | BA | (0.109,0.109)<br>(0.234,0.234) | F |
| | BT | (0.109,0.109)<br>(0.234,0.234) | T |
| | ME | (0.094,0.094)<br>(0.234,0.234) | T |
| (0.100,0.100)<br>(0.200,0.200) | BA | (0.156,0.156)<br>(single peak) | F |
| | BT | (0.141,0.141)<br>(single peak) | F |
| | ME | (0.084,0.094)<br>(0.219,0.219) | F |
| (0.100,0.100)<br>(0.175,0.175) | BA | (0.156,0.156)<br>(single peak) | F |
| | BT | (0.141,0.141)<br>(single peak) | F |
| | ME | (0.156,0.156)<br>(single peak) | F |

separation for the BA method is approximately twice the peak-width (for the BA method) while for the ME method it is much larger than twice the peak-width (for the ME method). This is attributed to the property of superposition which applies to the BA method but not the ME method.

The results presented in table 4.2 are in general agreement with the results of Malik *et al.* (1982). They have found that the ME method can be used to resolve sinusoids separated in frequency by 0.3 while the BA method can be used to resolve sinusoids separated in frequency by 0.6. The SNR for this result was +6 dB and 'exact' ACF values were used.

Malik *et al.* (1982) have observed that the PSE of the ME method provides the greatest improvement in terms of peak-position and peak-width over the BA PSE for small ACFs (4x4 to 12x12) estimated from data. Table 4.1 and 4.2 confirm that the ME PSE best represents the true PS of the three methods studied.

### 4.2.4 ME PSEs of Data with Noise

A PS analysis of simulated data with various levels of noise using the ME method was performed next. Variations in peak-position and peak-volume in the ME PSE were studied. The peak-position and peak-volume were used for the estimation of the frequency and the power of sinusoidal signals in the data set.

Fifty ME PSEs were calculated for a sinusoidal process (0.15, -0.15) at SNRs of 10 dB, 0 dB, and -10 dB. The position and the volume of the peaks in each of the fifty PSEs was recorded. The statistics of these variables are presented in table 4.3. The first column in table 4.3 indicates the variable considered, the second its mean value and the third its standard deviation (SD). The peak-position was defined as the frequency at the highest point in the PSE. The power of the sinusoidal signal was taken as the amplitude of the PSE at the peak-position. The average value of the PSE was also determined.

The results in table 4.3 indicate that at 10 dB and 0 dB SNRs the average position of the peak was close to the true frequency of the sinusoids. At -10 dB SNR there was a large error in average peak-position.

The estimates of the power of the sinusoidal signal from the PSE were also affected by the SNR. In the PSE as the noise level increased: the average peak-volume decreased, the standard deviation of the peak-volume increased and the ratio of average to standard deviation of peak-volume increased. This indicates that peaks become increasingly difficult to identify as the noise level increases.

The decrease in the mean peak-volume may be due to a change in the shape of the peak as reported by Malik *et al.*, (1982). An increase in the peak-width would produce a corresponding decrease in its amplitude. A high degree of variability in peak-position and peak-volume may be an indicator that the noise level is too high and spurious peaks exist in the PSE.

These results indicate that at 10 dB and 0 dB SNR the ME PSE can be used to identify sinusoidal waves on the 5x5 data grid. At a SNR of -10 dB the location of the peak in the ME PSE becomes random and the volume of the PSE at the peak become comparable to that of the background.

## Table 4.3

Statistics of the peak position and volume in ME PSE for a sinusoid (0.15,-0.15) in noise.

| | Mean | Standard Deviation |
|---|---|---|
| SNR 10 dB | | |
| n=50 | | |
| Estimated peak location | (0.154,-0.151) | (0.005, 0.008) |
| Error in peak location | (0.004, 0.001) | |
| Average peak volume | 381.2 | 90.64 |
| Background volume | 8.661 | 1.766 |
| SNR 0 dB | | |
| n=50 | | |
| Estimated peak location | (0.149, -0.151) | (0.009, 0.012) |
| Error in peak location | (0.001, 0.001) | |
| Average peak volume | 309.8 | 117.6 |
| Background volume | 8.281 | 1.818 |
| SNR -10 dB | | |
| n=50 | | |
| Estimated peak location | (.065, -0.246) | (0.226, 0.139) |
| Error in peak location | (0.085, 0.096) | |
| Average peak volume | 207.1 | 104.4 |
| Background volume | 28.45 | 7.357 |

### 4.3 Conclusions

From this analysis it is concluded that the ME method has higher resolution than other methods (BA and BT) of PS estimation. The ME method should therefore be used in spectral analysis of the spatial distribution of EEG data. This assumes, however, that the EEG can be described in terms of spatial waves, which are separated in frequency by at least 0.125 and that the SNR of the data is ≥0 dB.

# Chapter 5

# Spatial Spectral Analysis of the EEG

## 5.0 Introduction

This chapter examines the hypothesis: spatial PSEs of EEG topographic maps are correlated to the functional state of the brain. If the hypothesis can be supported by experimental data, it will indicate that the spatial waves on topographic maps are affected by brain function.

In order to test the hypothesis, topographic maps were constructed using EEG data from normal volunteers in two states, resting with eyes closed (EC) and resting with eyes open (EO). PSEs were obtained by applying the ME method to the topographic maps. Systematic variations between EC PSEs and EO PSEs were investigated using various statistical analyses. Systematic variations between PSEs normalized so that the total power in the topographic maps was a constant were also investigated.

## 5.1 Methods

### 5.1.1 Recording Conditions

The EEG data was recorded using the 31 Electrode System (developed in the Dept. of Applied Sciences in Medicine) under similar conditions to those described in Chapter 2. This electrode system (figure 5.1) provides a higher electrode density than the International 10-20 System. In addition, the electrodes are attached to a cap which is placed over the subject's scalp. This allows a relatively consistent positioning of the electrodes over a number of test subjects. The electrodes form a 5x7 grid on the scalp with the corner electrodes omitted. The electrode positions are defined in terms of meridian and parallel lines by assuming that the scalp forms a hemisphere with the nasion and inion at pole locations, a convention adopted in Chapter 2. The positions of the electrodes were

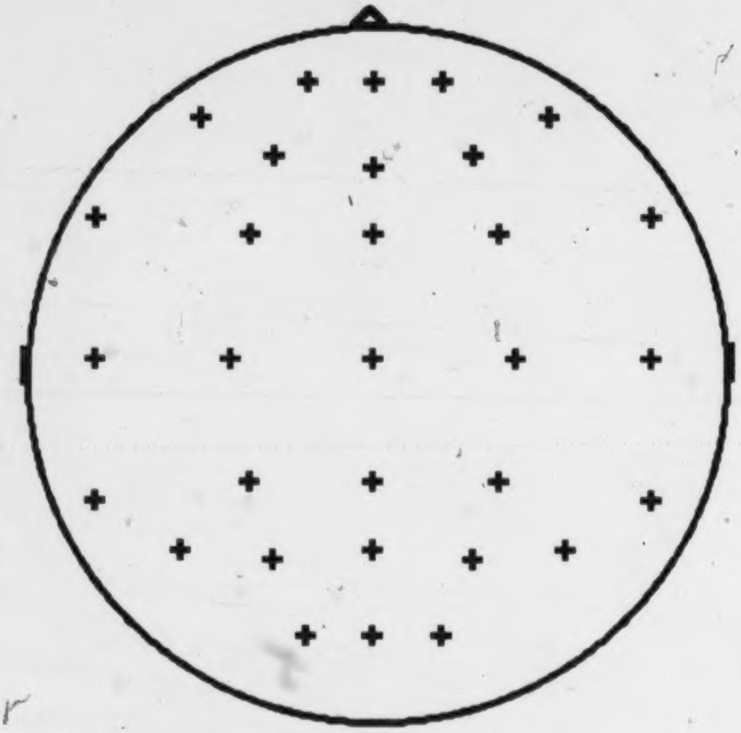

Figure 5.1 The 31 Electrode system orthonormally projected onto a plane.

determined for this study by placing the electrode cap over a styrofoam wig-head and marking the electrode sites, a practice commonly used in EEG laboratories (including U of A Hospital) to train electroenecphalographers in electrode placement. The positions of the electrodes are presented in table 5.1 in terms of meridian and parallel lines.

**Table 5.1 Electrode Positions of the 31 Electrode System in Meridians and Parallels.**

MERIDIANS (degrees)

| | | | | |
|---|---|---|---|---|
| * | +38.0° | 0.0° | -38.0° | * |
| +68.6° | +40.3° | 0.0° | -40.3° | -68.6° |
| +79.7° | +39.0° | 0.0° | -39.0° | -79.7° |
| +80.7° | +40.4° | 0.0° | -40.4° | -80.7° |
| +76.2° | +34.8° | 0.0° | -34.8° | -76.2° |
| +71.3° | +39.3° | 0.0° | -39.3° | -71.3° |
| * | +50.6° | 0.0° | -50.6° | * |

PARALLELS (degrees)

| | | | | |
|---|---|---|---|---|
| * | +68.6° | +73.1° | +68.6° | * |
| +47.2° | +46.1° | +55.5° | +46.1° | +47.2° |
| +25.1° | +21.1° | +19.4° | +21.1° | +25.1° |
| 0.0 | 0.0 | 0.0 | 0.0 | 0.0 |
| -29.3° | -28.0° | -20.0° | -28.0° | -29.3° |
| -49.5° | -49.8° | -55.5 | -49.8 | -49.5° |
| * | -70.9° | -75.0° | -70.9° | * |

EEG data was recorded and stored with a digitizer/datalogger (Koles, 1983). EEG signals were sampled at a rate of 120 per second, digitized with 12 bits per sample and stored on 8.5 inch floppy diskettes. The digitized signals were later transferred to and processed with a VAX 11/750 computer and a Amdhal 5870 in the Dept. of Applied Sciences in Medicine.

The volunteer subjects (18 males, 15 females) were first recorded in the EC state followed by the EO state. The EC state required subjects to be at rest with eyes closed. They were to remain awake and alert, yet completely relaxed during the recording session. The EC state was also used for the results presented in Chapter 2. The EO state required the subjects to be relaxed with eyes open. The subjects were required to remain still with eyes fixed on a single point and were asked to avoid blinking. It was presumed that subjects with their eyes closed were more relaxed then with their eyes open. Thus, the EC and EO states were distinguished by the brain processing visual stimuli as well as by the level of relaxation of the subjects. EEG data was recorded for a period of about 2 minutes in the EC state and 1 minute in the EO state from each subject.

### 5.1.2 Signal Processing and Topographic Mapping

EEG data is often corrupted by electrical signals generated by muscle movement and by external electrical noise-sources. The recorded data was therefore reviewed by trained clinical personnel and two 7.5-second segments of artifact-free data were selected from each record. All subsequent analyses were based on these 7.5-second segments of artifact-free data.

It was shown in Chapter 2 that, in the alpha band (8 to 13 Hz), topographic maps constructed from rms EEG data are representative of the actual distribution of potential on the scalp. In this study therefore, the data was first filtered into the alpha band and then converted to rms form. The rms EEG was calculated over 0.5-second epochs so that each 7.5-second segment of artifact-free data was converted into 15 rms EEG values.

The rms EEG was projected from the scalp onto a flat plane using the Mercator method (also discussed in Chapter 2). This projection, based on a hemispherical scalp of radius 100/2π cm, resulted in maps with dimensions of 44.8 cm by 57.9 cm (between ±80° meridians and ±70° parallels). The Mercator projection of the 31 Electrode System is presented in figure 5.2.

Topographic maps of the projected potentials were constructed using triangular interpolation (also presented in Chapter 2) which is most suitable to Mercator projections of the 31 Electrode System. Each topographic map, constructed from a set of rms EEG values, represented the distribution of rms scalp potential over a 0.5-second epoch.

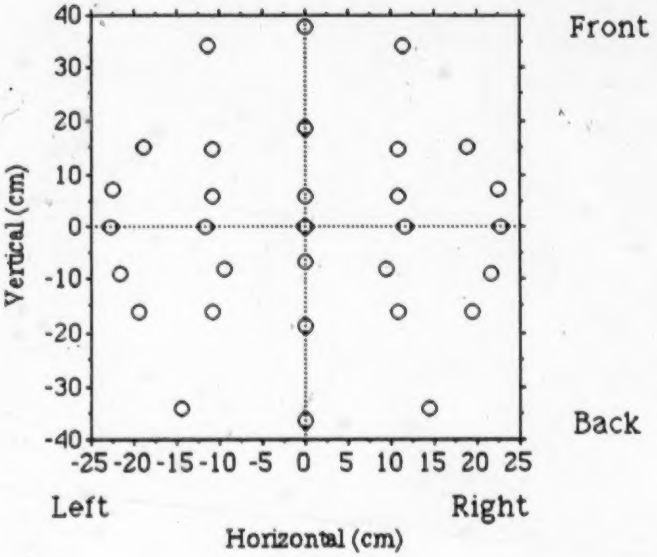

Figure 5.2 Mercator projection of the 31 Electrode System. The head is assumed to be a sphere of radius 100/2π cm.

### 5.1.3 Maximum Entropy Spectral Estimation

In this section, the application of the ME method of PS estimation to topographic maps of EEG data is reviewed. ME PSEs were calculated using the Lim and Malik (L&M) algorithm (L&M algorithm is discussed in Chapter 3). Use of this algorithm requires knowledge of a portion of the autocorrelation function (ACF). The ACF was estimated from the topographic maps using:

(5.1:1)

$$\mathrm{ACF}(m_1\, m_2) = \frac{1}{N_1 - m_1}\ \frac{1}{N_2 - m_2} \sum_{n_1=m_1}^{N_1-1} \sum_{n_2=m_2}^{N_2-1} x(n_1\, n_2)\, x(n_1 - m_1\, n_2 - m_2)$$

where

$x(n_1, n_2)$ is the voltage at $(n_1, n_2)$ on the topographic map,

$(n_1, n_2)$ are orthogonal integer variables in the spatial domain,

$(m_1, m_2)$ are orthogonal integer variables in the correlation domain.

In order to use equation (5.1:1) the potential distribution, x, must be uniformly sampled. The topographic maps were therefore resampled with a uniform pattern. The resampled sites were close to the actual electrode sites and formed a regular 5x5 grid. The distance between resampled sites on the map was 8.63 cm in the $n_1$ direction and 7.23 cm in the $n_2$ direction, and the maps were resampled in the region between ±62° meridians and ±46° parallels. The Mercator projection of the resampled sites as well as the actual electrode sites are presented in figure 5.3.

An ACF estimate was produced for each topographic map after removal of its average value. Fifteen ACF estimates were generated for each artifact-free segment of EEG data. A mean ACF estimate was then calculated and assumed to represent the entire segment. ME PSEs were calculated using these mean ACF estimates and the L&M algorithm.

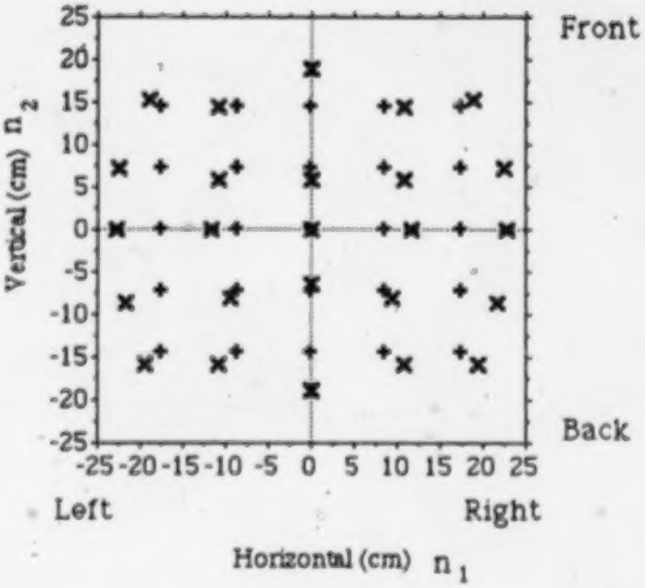

Figure 5.3 Mercator projection of the 31 Electrode System and resampled electrode sites. The electrode sites are shown with x's and the resampled sites are shown with +'s.

The stopping criterion for the number of iterations in the L&M algorithm is based on the normalized ACF error (defined in Chapter 3). A typical example of the profile of the normalized ACF error as a function of the number of iterations for actual EEG data is shown in figure 5.4. The rate of change (ie. the slope) of the error curve as a function of iteration number is an indicator of the change in the PSE between iterations. The slope of the error curve is initially very large, indicating rapid change with iterations, however, the slope decreases quickly and is close to zero by about 15 iterations. As an example, in figure 5.4 the slope is initially about -8000, at the 5th iteration it is -38, at the 10th iteration it is -0.243 and at the 15th iteration it is -0.0042. This suggests that there is little change in the PSE between the 14th and the 15th iteration. A substantial reduction in the slope occurred consistently for all subjects before 15 iterations indicating that this was sufficient for a final estimate of the ME PS. Therefore, in this study the ME PSEs were estimated after 15 iterations of the L&M algorithm.

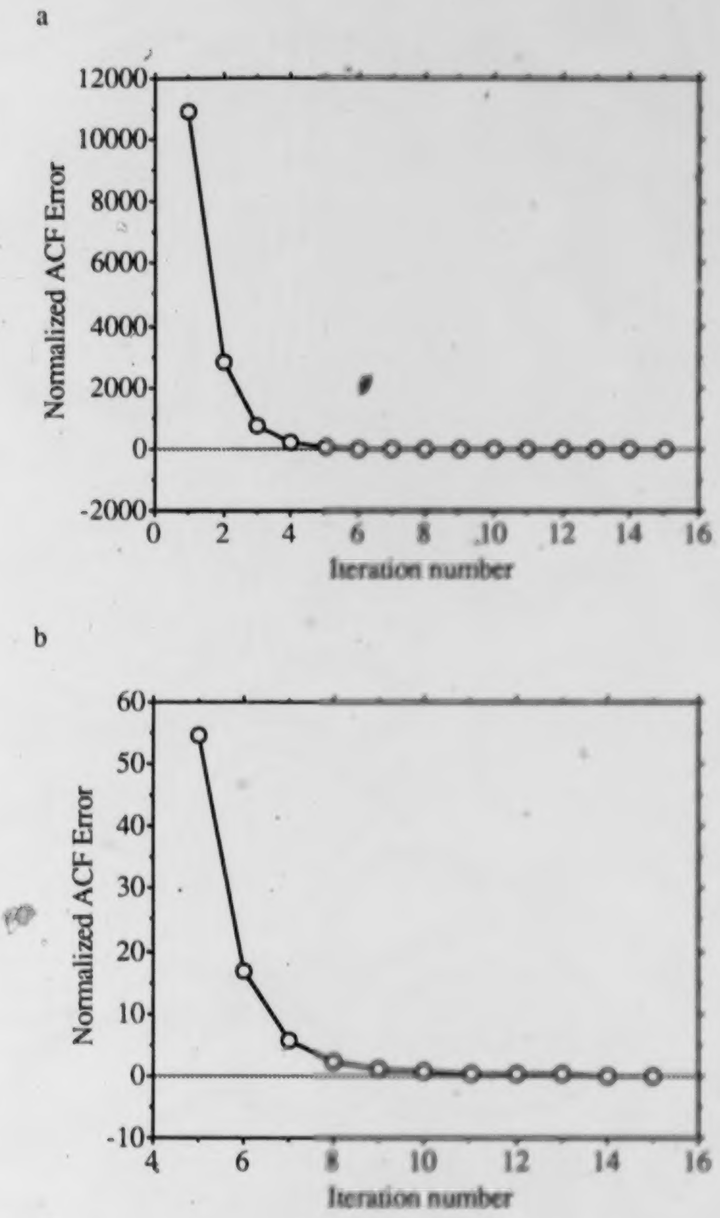

Figure 5.4 The normalized ACF error in successive iterations of the L&M algorithm for actual EEG data. The figure (a) shows values from 1 to 15 iterations while the figure (b) shows values from 5 to 15.

### 5.1.4 Data Reduction

In order to meaningfully compare the PSEs a form of data reduction was used. The PSEs were reduced into a set of feature vectors (FVs) with each FV consisting of 11 features computed from the first and second quadrants of the PSE.

The background of the PSE was removed before computation of the features. Any value in the PSE below 10% of the maximum value in the PSE was set to zero. This threshold, which is at the -10 dB level, was selected after observing that all PSEs had at least a 15 dB dynamic range.

The first 10 features (referred to as the A features) were computed by dividing the first and the second quadrants of the PSE into 10 regions or spatial frequency bands (shown in figure 5.5). The volumes under the PSE surface in these regions were used as the features. In this way, the PSE was approximately represented by 10 waves of various orientations and wavelengths corresponding to the midpoint of each region.The A features are presented as equivalent waves in table 5.2.

The final feature was the entropy of the PSE. It can be viewed as a generalized measure of uniformity. The entropy, defined as $E1=-(\Sigma f_n \cdot \ln(f_n))$, where $f_n = PSE(n)/\Sigma PSE(n)$, is at a minimum if the PSE contains a single impulse and it is at a maximum when the PSE is uniform. That is, for a single impulse in the PSE, $E1=0$ and for a completely uniform PSE, $f_n=1/N$ so that $E1=-\ln(1/N)$. For this particular study $N=(64x64)=4096$, and thus the range of values for the entropy was 0 to 8.318.

Some further processing was done with the features that were calculated from the PSEs. In order to analyze only variation between the EC and the EO states, first the average value of the feature was determined over both states for each subject. This subject average was then subtracted from the average value of the feature for each subject in each state. This processing resulted in the features indicating change in the PSE from its mean value that was dependent only on the state.

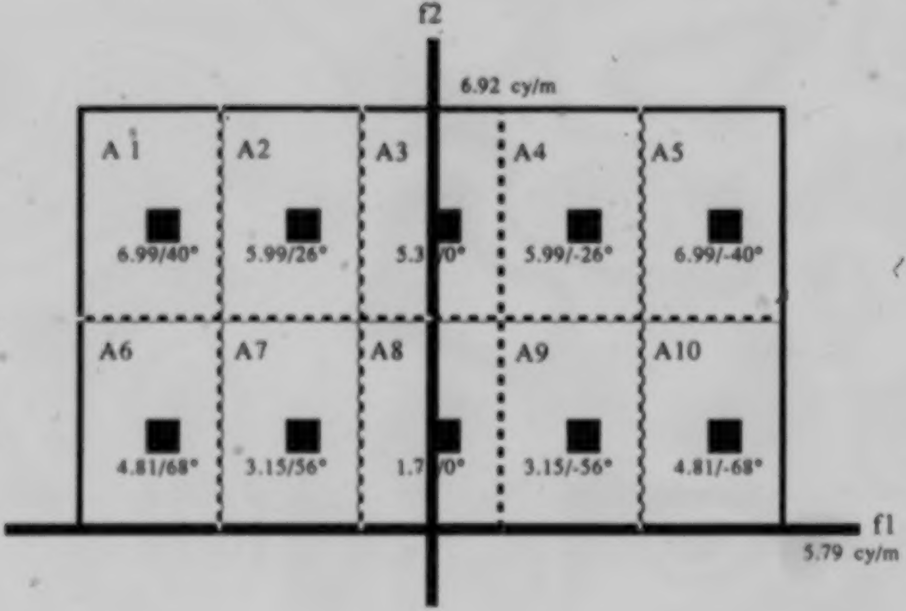
f2
6.92 cy/m
A 1
6.99/40°
A2
5.99/26°
A3
5.3
/0°
A4
5.99/-26°
A5
6.99/-40°
A6
4.81/68°
A7
3.15/56°
A8
1.7
/0°
A9
3.15/-56°
A10
4.81/-68°
f1
5.79 cy/m

Figure 5.5 First and second quadrants of the PSE divided into 10 regions. Each region has a black square indicating the center point of the region.

**Table 5.2 Waves Equivalent to Features**

| Feature | Wavelength (cm) | Orientation (degree from sagittal.) |
|---|---|---|
| A1 | 14.29 | +40 |
| A2 | 16.67 | +26 |
| A3 | 18.67 | 0 |
| A4 | 16.67 | -26 |
| A5 | 14.29 | -40 |
| A6 | 20.75 | +68 |
| A7 | 31.65 | +56 |
| A8 | 55.87 | 0 |
| A9 | 31.65 | -56 |
| A10 | 20.75 | -68 |

### 5.1.5 Methods of Data Analysis

Three approaches were used to investigate the characteristics of the data: (1) comparison of the feature means, (2) correlation analyses and (3) discriminant analyses. The mean value of the features were compared between the EC and the EO states with a paired t-test. This test was used to determine if significant differences existed in the mean values of the features between the two states. The correlation analysis, on the other hand, showed the interaction between features. It is useful for identification of features that are highly related. Finally in the discriminant analysis a linear function was determined that maximally separated EC data from EO data.

#### 5.1.5.1 Overview of Discriminant Analysis

Discriminant analysis is a statistical technique concerned with separating a set of multivariate observations into previously defined groups. The most commonly used form of this analysis is that due to Fisher (1936) which provides a linear function of the observations based on maximizing the between group sum of squares relative to the within group sum of squares. The resulting function can be used for classifying unknown observations. In practice a common procedure is to construct the discriminant function from samples of known composition, referred to as a training set. In order to evaluate the performance of the obtained function, this is often followed by a validation step in which the discriminant function is applied to a new sample of observations whose group membership is known. The proportion of observations correctly classified is then used as a criterion for evaluating the performance of the function.

There is some danger that a discriminant function can become tailored too closely to the training data if too many variables are allowed to enter the function. The number of variables can be reduced by using a stepwise discriminant analysis. This procedure constructs a linear discriminant function by selecting, according to certain criteria, a subset of the original variables which provides the best possible discrimination. Variables are usually selected in order of importance, for their ability to discriminate between groups. These variables are chosen by applying, at each step, statistical tests for inclusion or deletion of variables. In this study stepwise discriminant analysis was used.

### 5.1.6 Summary

In this study 66 records of EEG data were analyzed, 33 from the EC state and 33 from the EO state. From each record two 7.5-second segments of artifact-free data were identified by trained clinical personnel. These artifact-free segments were processed by filtering into the alpha band and then a time series of rms values over 0.5-second epochs was determined. The rms EEG was projected using the Mercator method onto a flat plane and topographic maps were constructed using triangular interpolation. The maps were then resampled at regular intervals on a 5x5 grid. Estimates of the autocorrelation function were made from the resampled maps and then averaged to produce a mean ACF estimate. The mean ACF estimate was taken to represent the artifact-free segment of EEG data. The L&M algorithm was used with the mean ACF estimates to produce ME PSEs. The ME PSEs were reduced into a set of feature vectors, with each feature indicating changes in the volume of the PSE in various regions about the subject mean for each functional state.

Paired t-tests, correlation analyses and discriminant analyses were used to study characteristics of features from EC PSEs and EO PSEs.

## 5.2 Results

### 5.2.1 PSEs of Topographic Maps

Examples of topographic maps used in this study are presented in figure 5.6. They were produced from a subject in the EO state and are representative of maps from a artifact-free segment of EEG data. In maps 1 and 2 there appear to be larger values in the front-left and back-right regions. These spatial variations may be considered as a wave on these topographic maps. In addition, the maps have larger values in the back than in the front. This too may be described as a wave on the maps.

Figure 5.7 and 5.8 presents the PSE corresponding to the artifact-free segment of EEG data from which figure 5.6 was derived. Figure 5.7 is a wireframe view and 5.8 is a greylevel view. Recall that a sinusiodal wave is represented in the PSE as a pair of peaks oriented in the direction of the wave and situated symmetrically about the origin. There are 4 peaks observed in the PSEs in figures 5.7 and 5.8, one pair that corresponds to the front-left to back-right variation and the other pair that corresponds to the front to back variation in the topographic maps.

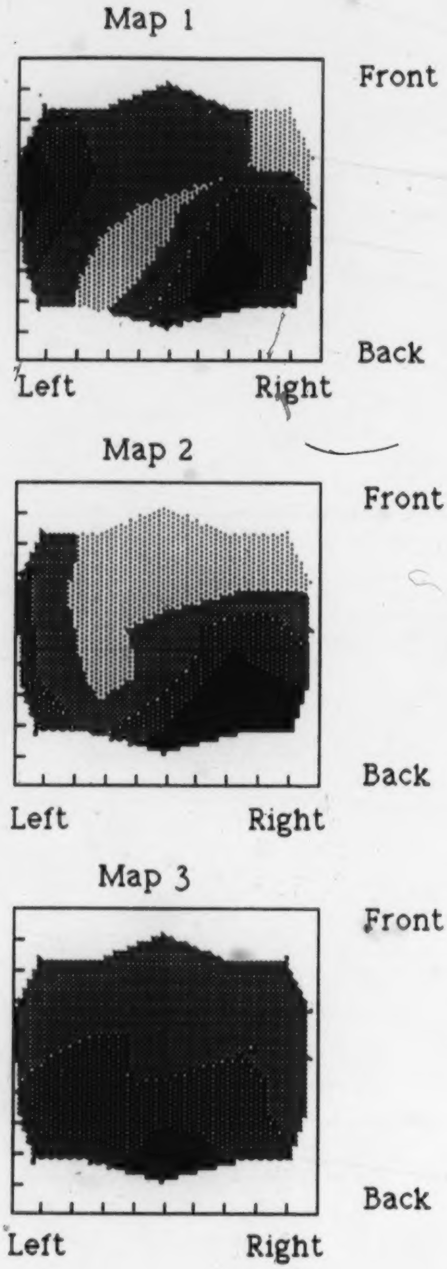
Map 1
Front
Back
Left
Right
Map 2
Front
Back
Left
Right
Map 3
Front
Back
Left
Right

Figure 5.6 Mercator topographic maps of rms EEG data from a subject in the EO state. The maps are the 1st, 6th, and 11th of a set of 15 obtained from the subject. Dark areas represent higher values of potential.

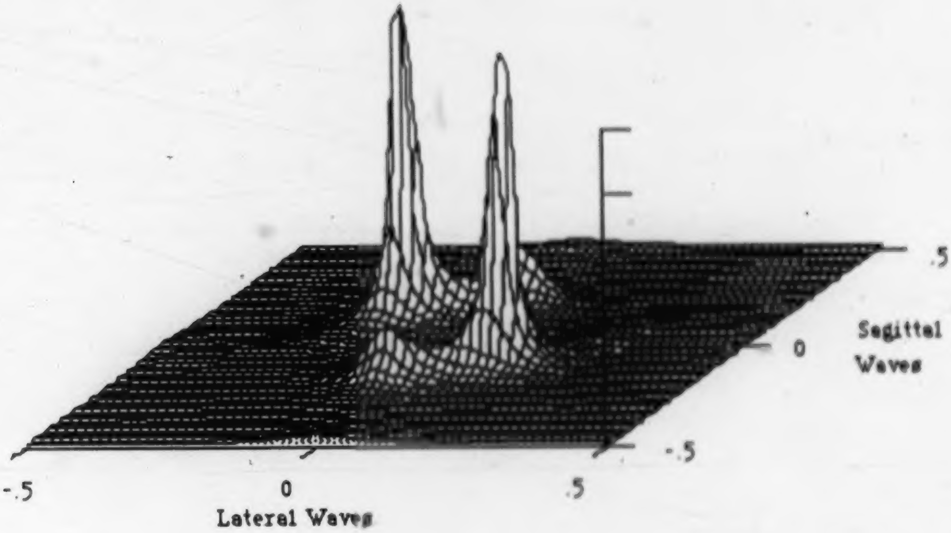

Figure 5.7 Wireframe view of PSE of topographic maps presented in figure 5.6 The origin of the PSE is in the center of the figure. The PSE is symmetric about the origin.

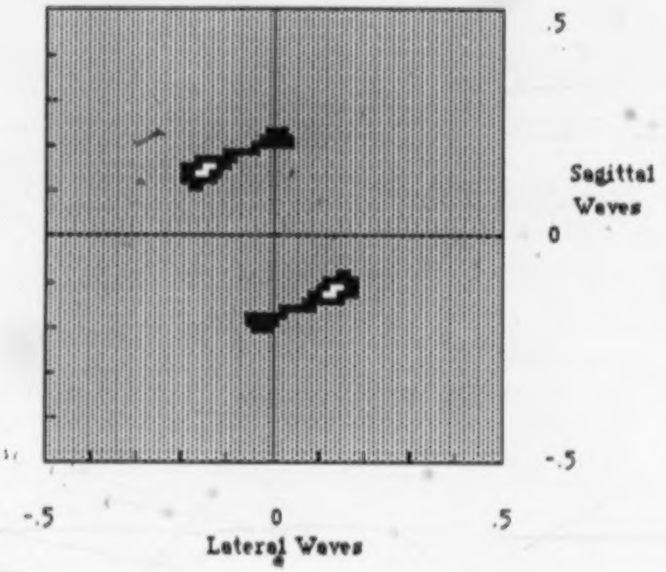

Figure 5.8 Greylevel plot of PSE of topographic maps presented in figure 5.6. The origin of the PSE is in the center of the figure. The greylevels used are: 0 to -3 dB, white; -3 db to -10 dB, black; and <-10 dB, grey.

### 5.2.2 Comparison of Feature Means

The mean and standard deviation of the 11 features from the PSEs are presented in table 5.3. The mean values of six of the A features are positive for the EC state and negative for the EO state. This indicates that the energy of waves in EC topographic maps was generally higher than that found in EO topographic maps. In other words, the EC topographic maps simply contained more powerful signals than did EO topographic maps.

The features means were compared with a paired t-test since correlations were observed between EC and EO FVs. The null hypothesis of equal group means was rejected ($p<0.01$) for features A3 and E1. This indicates that the means of these features differ significantly between EC and EO states.

The mean and standard deviation of the features from the normalized PSEs are presented in table 5.4. The mean values of the A features are negative in the EC state for all regions except A3 and A8. These two regions identify waves oriented purely in the sagittal direction. This suggests that the EC state is characterized by a large portion of the activity in the map oriented in the sagittal direction while the EO topographic map is more diverse with activity oriented in all directions.

The feature means from the normalized PSEs were also compared with the paired t-test. For this data set the null hypothesis of equal group means was rejected ($p< 0.01$) for A3, A4, A7, A9, A10 and E1. Thus, the distribution of power in the normalized PSE appears to be dependant on the subject's state. These results show that statistically significant differences exist between the normalized EC PSEs and EO PSEs.

The E1 feature was found to be significantly different in the paired t-test for both PSEs and normalized PSEs. The E1 feature represents the entropy and is a measure of uniformity. A highly uniform PSE indicates that all waves are present in equal magnitude in the corresponding topographic map. Such a map appears complex with little or no spatial correlation. The E1 feature had a larger mean value for EO PSEs than for EC PSEs therefore the EO state is characterized by topographic maps more complex than those for the EC state.

**Table 5.3 Mean & Standard Deviations of Features and paired t-test for PSEs** (n=66, df=32)

| Variable | Cognitive State | | | | t-value | Sig >.99 |
|---|---|---|---|---|---|---|
| | EC | | EO | | | |
| | Mean | SD | Mean | SD | | |
| A1 | ----- | ----- | ----- | ----- | ----- | no |
| A2 | .0214 | .1331 | -.0214 | .1331 | .4961 | no |
| A3 | 6.275 | 8.643 | -6.275 | 8.643 | 4.540 | yes |
| A4 | -.0648 | .2460 | .0648 | .2460 | 1.972 | no |
| A5 | ----- | ----- | ----- | ----- | ----- | no |
| A6 | 0.718 | .3373 | -0.718 | .3373 | 1.701 | no |
| A7 | .0414 | .6137 | -.0414 | .6137 | .0805 | no |
| A8 | .4762 | 1.280 | -.4762 | 1.280 | 1.136 | no |
| A9 | -.0820 | .5670 | .0820 | .5670 | .0441 | no |
| A10 | .0315 | .3012 | -.0315 | .3012 | .0375 | no |
| E1 | -.9847 | 2.015 | .9847 | 2.015 | 2.381 | yes |

----- indicates that the value of the feature was zero.

**Table 5.4 Mean & Standard Deviations of Features and paired t-test for Normalized PSEs** (n=66, df=32)

| Variable | Cognitive State | | | | t-value | Sig >.99 |
|---|---|---|---|---|---|---|
| | EC | | EO | | | |
| | Mean | SD | Mean | SD | | |
| A1 | ----- | ----- | ----- | ----- | ----- | no |
| A2 | -.8645 | 4.515 | .8645 | 4.515 | 1.795 | no |
| A3 | 23.57 | 36.85 | -23.57 | 36.85 | 2.956 | yes |
| A4 | -2.217 | 4.678 | 2.217 | 4.678 | 3.234 | yes |
| A5 | ----- | ----- | ----- | ----- | ----- | no |
| A6 | -1.011 | 9.451 | 1.011 | 9.451 | .1998 | no |
| A7 | -11.13 | 20.199 | 11.13 | 20.20 | 3.234 | yes |
| A8 | 1.297 | 15.16 | -1.297 | 15.16 | 1.176 | no |
| A9 | -5.279 | 11.997 | 5.279 | 11.99 | 2.268 | yes |
| A10 | -5.077 | 11.07 | 5.077 | 11.07 | 3.216 | yes |
| E1 | -.9847 | 2.015 | .9847 | 2.015 | 2.381 | yes |

----- indicates that the value of the feature was zero.

### 5.2.3 Correlation Analysis

Table 5.5 presents the correlation of the features from the PSEs. The relationships between the features can be identified from this table. These relationships are best visualized by considering the features as waves of various wavelengths and orientations (equivalent waves are presented in table 5.2).

Two basic patterns are observed from this table, correlations tend to exist between waves that are oriented in almost perpendicular directions and correlations tend to exist between waves that are oriented in almost parallel directions. Examples of this are A2, A9 and A10 which are highly correlated (> 0.7). A2 is oriented at +26° from the sagittal line, and A9 and A10 are oriented at -56° and -68° from the sagittal line respectively. A2 is almost perpendicular to both A9 and A10, and A9 and A10 are almost parallel to each other. Other examples are A4 and A6 which are perpendicular and mildly correlated (0.4 to 0.6), and A3 and A8 which are parallel and mildly correlated. Other features in this table follow this pattern also.

Table 5.6 presents the correlations of the features from normalized PSEs. The most striking characteristic observed from this table is that A3 is mildly correlated with A6, A7, A8, A9 and A10. Thus, in normalized topographic maps the sagittal wave associated with A3 occurs with waves in virtually all orientations and wavelengths.

### Table 5.5 Correlations of PSE Features

| | A1 | A2 | A3 | A4 | A5 | A6 | A7 | A8 | A9 | A10 | E1 |
|---|---|---|---|---|---|---|---|---|---|---|---|
| A1 | | | | | | | | | | | |
| A2 | | 1.0 | | | | | | | | | |
| A3 | | -.06 | 1.0 | | | | | | | | |
| A4 | | .012 | -.12 | 1.0 | | | | | | | |
| A5 | | | | | | | | | | | |
| A6 | | .279 | -.24 | -.43 | | 1.0 | | | | | |
| A7 | | .088 | -.04 | .009 | | -.13 | 1.0 | | | | |
| A8 | | -.07 | .596 | -.13 | | -.24 | .449 | 1.0 | | | |
| A9 | | .803 | -.10 | .195 | | .318 | .102 | -.02 | 1.0 | | |
| A10 | | .754 | -.50 | .071 | | .291 | .124 | -.26 | .742 | 1.0 | |
| E1 | | .372 | -.42 | .039 | | .600 | .258 | -.167 | .511 | .600 | 1.0 |

No values printed for A1 and A5 as they are constants.

### Table 5.6 Correlations of Normalized PSE Features

| | A1 | A2 | A3 | A4 | A5 | A6 | A7 | A8 | A9 | A10 | E1 |
|---|---|---|---|---|---|---|---|---|---|---|---|
| A1 | | | | | | | | | | | |
| A2 | | 1.0 | | | | | | | | | |
| A3 | | .250 | 1.0 | | | | | | | | |
| A4 | | .286 | -.09 | 1.0 | | | | | | | |
| A5 | | | | | | | | | | | |
| A6 | | -.05 | -.35 | .250 | | 1.0 | | | | | |
| A7 | | -.15 | -.58 | -.09 | | -.11 | 1.0 | | | | |
| A8 | | -.42 | -.59 | -.05 | | -.09 | .255 | 1.0 | | | |
| A9 | | .056 | -.48 | .228 | | .422 | -.09 | .036 | 1.0 | | |
| A10 | | .164 | -.41 | .223 | | .045 | -.17 | .142 | .468 | 1.0 | |
| E1 | | .054 | -.45 | .361 | | .553 | -.22 | .114 | .451 | .630 | 1.0 |

No values printed for A1 and A5 as they are constants.

### 5.2.4 Discriminant Analysis

A total of 66 FVs, each containing 9 non-zero features, were used in these analyses. FVs were randomly divided into a training set (about 60%) containing 43 FVs (23 EC FVs and 20 EO FVs) and a test set (about 40%) containing 23 FVs (10 EC FVs and 13 EO FVs). A stepwise discriminant analysis of the training set was performed with the maximum number of variables in the discriminant function restricted to four. The obtained discriminant function was then applied to the test set and the percentage of correct classifications tabulated.

#### 5.2.4.1 Discriminant Analysis of PSEs

The stepwise discriminant analysis of the training set FVs formed a discriminant function containing A3, A6, A10, and E1. For this set, 87% of the EC FVs were correctly classified and 95% of the EO FVs were correctly classified. When the discriminant function obtained from the training set was applied to the test set, 100% of the EC FVs were correctly identified and 92% of the EO FVs were correctly identified. It appears from the high classification rates that discriminant analysis based on ME PSEs provides a useful method for predicting the EC and EO state of subjects. The percentage of FVs correctly classified was about the same in the training set as in the test set indicating that the classification rule is stable when applied to new observations. These results are presented in table 5.7.

The features in this analysis may be visualized as equivalent waves. A3 represents a wave of wavelength 18.67 cm and an orientation along the sagittal direction. A6 and A10 represent waves of wavelength 20.75 cm with symmetric orientations of ±68° from the sagittal direction. In order to obtain an intuitive understanding for these waves, they are presented on topographic maps in figure 5.9. The topographic map spans about 2 cycles of the A3 wave and slightly less cycles of the A6 and A10 waves. The mean values of these features were larger in the EC state than in the EO state (shown in table 5.3). Therefore, these waves tend to have large amplitudes in the EC topographic maps than in the EO topographic maps.

E1, which is a measure of the uniformity of the PSE, was also selected in the discriminant analysis. It has a smaller mean value for the EC state than the EO state. As previously suggested, this indicates that topographic maps of EO data have less spatial correlation than do topographic maps from EC data.

Table 5.8 gives the standardized coefficients of the discriminant function. The magnitude of these coefficients indicates the relative importance of the features in the discriminant function. The largest coefficient, -0.853, corresponding to E1, indicates that entropy (ie. the uniformity of the PSE) is the most important indicator when distinguishing between EC and EO PSEs. This is followed by, 0.810, the coefficient for A3, which indicates that activity along the sagittal direction, is next most important for discrimination. The third and fourth coefficients are 0.775 and 0.632, for A6 and A10 respectively, both of which indicate activity primarily in the lateral direction.

The correlations among the features used in the discriminant function may be observed from table 5.5. The table shows that all variables selected are mildly correlated (0.4 to 0.6) with each other, except A6 which is weakly correlated (< 0.3) with both A3 and A10.

### Table 5.7 Classification Results for Training and Test Data Sets for PSEs

Training Data Set

| Actual Group | No. of Cases | Predicted Group Membership EC | EO |
|---|---|---|---|
| EC | 23 | 20<br>87.0% | 3<br>13.0% |
| EO | 20 | 1<br>5.0% | 19<br>95.0% |

Percent of cases correctly classified: 91.0%

Test Data Set

| Actual Group | No. of Cases | Predicted Group Membership EC | EO |
|---|---|---|---|
| EC | 10 | 10<br>100% | 0<br>0.0% |
| EO | 13 | 1<br>7.7% | 12<br>92.3% |

Percent of cases correctly classified: 96.2%

### Table 5.8 Standardized Discriminant Function Coefficients for PSEs

| Feature | Coefficient |
|---|---|
| A3 | .810 |
| A6 | .774 |
| A10 | .632 |
| E1 | -.853 |

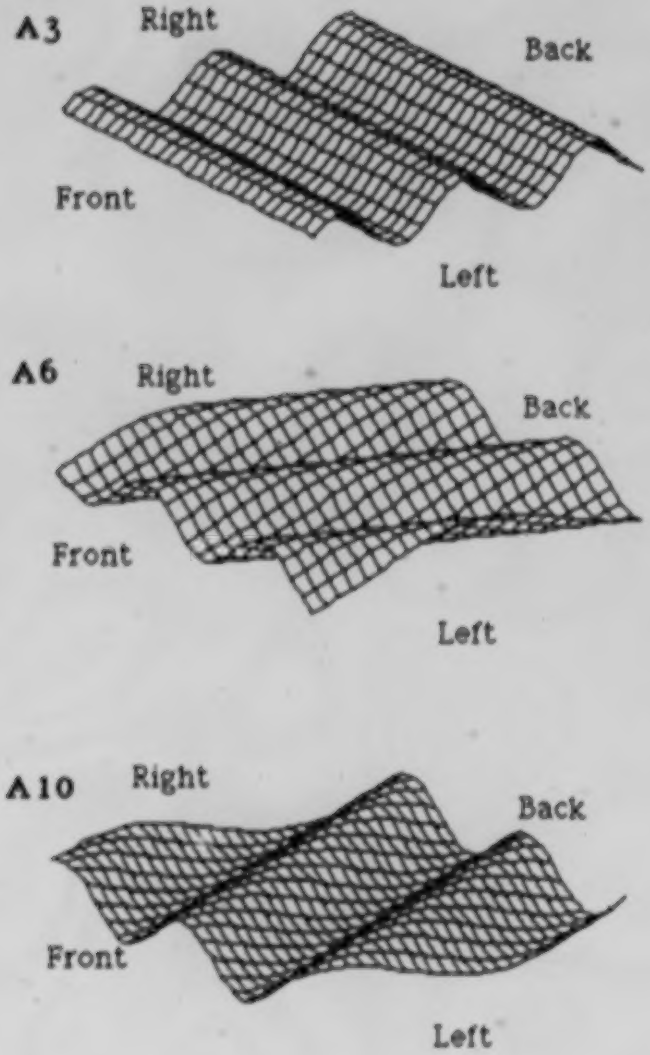
A3
Right
Back
Front
Left
A6
Right
Back
Front
Left
A10
Right
Back
Front
Left

Figure 5.9 Topographic maps of equivalent waves for the A3, A6 and A10 features. These features have large mean values in the EC state than in the EO state.

### 5.2.4.2 Discriminant Analysis of Normalized PSEs

The four variables selected in the stepwise discriminant analysis of features from normalized PSEs were A4, A7, A8, A10. For the training set, 83% of EC FVs were correctly classified and 90% of the EO FVs were correctly classified. On application of the discriminant function to the test set, 100% of the EC FVs were correctly classified and 85% of the EO FVs were correctly classified. Although there was some change in the level of correct classification between training and test sets, it appears that a reasonably consistent classification of normalized PSEs was achieved and a useful classification rule was again developed. These results are presented in table 5.9.

The equivalent waves for the features selected in the discriminant function are: A4 (16.67 cm, -26°), A7 (31.65 cm, +56°), A8 (55.87 cm, 0°) and A10 (20.57 cm, -68°). In figure 5.10 the A7, A10, A8 and A4 features are presented as waves on topographic maps. The mean values of A7, A10, and A4 are negative in table 5.4 for the EC state which indicates that these features have a relatively lower value in the EC state than in the EO state. The mean value of the A8 feature, which defines a sagittal wave, is positive in the EC state which indicates that this feature has a relatively larger value when compared to that found in the EO state.

The coefficients of the standardized discriminant function are given in table 5.10. The order of the coefficient from largest to smallest is: A7, A10, A4, A8. A7 and A10 are the most important to the discrimination as their coefficients are almost 50% larger than the coefficients for A4 and A8.

## Table 5.9 Classification Results for Training and Test Data Sets for Normalized PSEs

Training Data Set

| Actual Group | No. of Cases | Predicted Group Membership EC | EO |
|---|---|---|---|
| EC | 23 | 19<br>82.6% | 4<br>17.4% |
| EO | 20 | 2<br>10.0% | 18<br>90.0% |

Percent of cases classified correctly : 86.3%

Test Data Set

| Actual Group | No. of Cases | Predicted Group Membership EC | EO |
|---|---|---|---|
| EC | 10 | 10<br>100% | 0<br>0.0% |
| EO | 13 | 2<br>15.4% | 11<br>84.6% |

Percent of cases classified correctly : 92.3%

## Table 5.10 Standardized Discriminant Function Coefficients for Normalized PSEs

| Feature | Coefficient |
|---|---|
| A4 | .418 |
| A7 | .766 |
| A8 | -.443 |
| A10 | .608 |

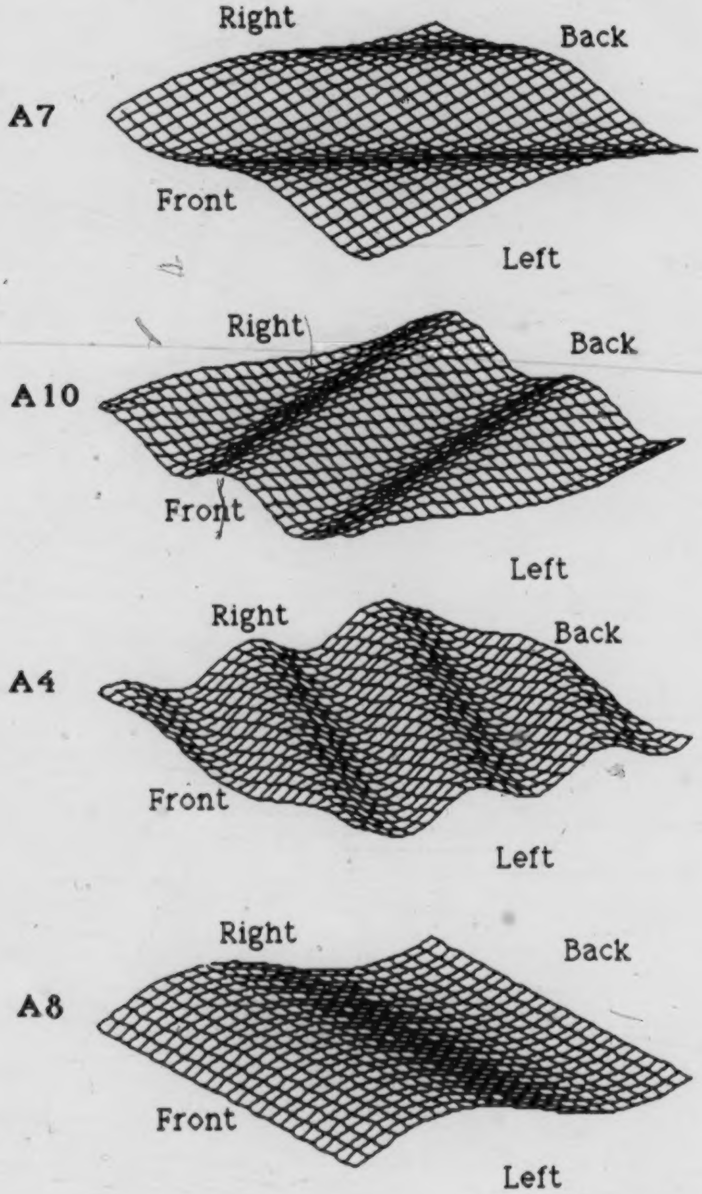

Figure 5.10 Topographic maps of equivalent waves for A7, A10, A4, and A8 features. The A7, A10 and A4 features have larger mean values in normalized EO PSEs and the A8 feature has a larger mean value in the normalized EC PSEs.

## 5.3 Discussion and Conclusions

The paired t-test of features from EC PSEs and EO PSEs showed significant differences in the mean values of A3 and E1. A3 had a larger mean value in the EC state than in the EO state indicating that the associated sagittal wave was larger in EC topographic maps. E1 had a larger mean value in the EO state than in the EC state indicating that EO PSEs are more uniform than EC PSEs and therefore EO topographic maps have less spatial correlations than do EC topographic maps. These results imply that the mean values of certain features can be useful in determining if data is from either EC or EO state. These results support the basic hypothesis examined in this chapter, that spatial PSEs of EEG data are correlated to the functional state of the brain.

A discriminant analysis of FVs was performed in order to determine if EC and EO states could be distinguished for individual cases based on PSEs. The linear discriminant function developed in this analysis transforms multivariate FVs into a univariate space such that there is a minimum overlap between the observation from the two states. The unknown state associated with an individual FV may be predicted from the position in the univariate space to which the FV is transformed by application of the discriminant function.

The discriminant function developed in the discriminant analysis correctly classified about 91% of the FVs in the training set and about 96% of the FVs in the test set. Because the percentage of FVs correctly identified is high, it is concluded that the discriminant function provides a meaningful classification. The classification rule is also useful for classifying records from unknown data since a high percentage of FVs were correctly classified in both the training and the test sets.

An examination of the discriminant function coefficients indicates the relative importance of variables used in the classification. The discriminant function developed in this analysis contained the variables A3, A6, A10, and E1. The coefficient associated with A3 was larger than those associated with A6 and A10. The orientations of the waves associated with these variables suggests the possibility of change in cerebral organization in response to the EC and EO states. The dominance of the A3 wave in relation to A6 and A10 waves suggests a cortical response primarily to visual information in occipital regions with a sagittal wave, followed by an interpretation of spatial information which is reflected in lateral waves. Further research is needed however, to determine fully the spatial wave content of the EEG during tasks which are primarily spatial in nature.

In order to investigate differences in topographic maps from the EC and EO states that are not related to the total power in the maps an analysis of normalized PSEs was performed. Each PSE was normalized so that the volume under its surface was a constant value. Paired t-tests and a discriminant analysis of features from the normalized PSEs was performed.

The paired t-test showed significant differences in the mean values of A3, A4, A7, A9, A10 and E1 implying that certain characteristics of normalized EEG topographic maps are related to the functional state of the brain.

The application of the stepwise discriminant analysis to the training set of FVs from normalized PSEs produced a discriminant function that correctly classified about 86% of the FV and in the test set about 92% of the FVs. Thus a stable and useful classification rule was again developed.

The variables selected in the discriminant analysis were A4, A7, A8, and A10. The coefficients for A7 and A10 were about 50% larger than those for A4 and A8 implying that these features are most important to the discrimination between EC and EO PSEs.

This work has shown that EC and EO states may be differentiated based on features from PSEs. Thus, there are characteristics of the PSEs that are unique to the EC and EO states and a description of these characteristics is made through the features that are selected in these analyses.

# Chapter 6
# Discussion and Conclusions

## 6.1 Discussion

This thesis is concerned with the analysis of electric potentials from the brain in terms of EEG topographic maps. Two basic questions are addressed: (1) is the actual distribution of potential on the scalp accurately and precisely represented by EEG topographic maps, and if the potential distribution can be represented by maps then, (2) is the distribution of scalp potential when decomposed into spatial waves on topographic maps useful in the classification and characterization of functional brain states.

In order to investigate the first question, the basic methodology used was to construct topographic maps without considering the potential at certain test-electrode sites and then to compare the measured potentials with the predicted potentials at the test sites. The electrode sites were specified by the International 10-20 System and topographic maps of instantaneous scalp potentials (called instantaneous EEG) and rms scalp potentials (rms values of EEG over 0.5 sec epochs, called rms EEG) were considered, the former being used primarily in the analysis of event-related potentials and the later being used in the analysis of background EEG. The analysis involved determining: (1) the error signal, the difference between measured and predicted potentials, and (2) the regression line between measured and predicted potentials.

Topographic maps of broad-band (0.5 to 30 Hz), instantaneous scalp potentials showed that the mean value of the error was small indicating that the maps had a low bias. The rms value of the error, however, was large in the maps.

Topographic maps constructed with instantaneous EEG data filtered into the alpha band showed about a 20% decrease in the percentage of rms error over that obtained for broad-band EEG maps. This result suggests that the distribution of electric potential on the scalp is affected by the temporal frequency content of the EEG. It further suggests that the sampling density required to represent the spatial distribution of the scalp potential depends heavily on the temporal frequency content of the EEG and that a higher sampling density than that currently used is required in order to achieve the precision in broad-band EEG maps that is obtained in alpha-band EEG maps. The regression analysis of instantaneous EEG data supports these findings with larger $r^2$ values for the alpha-band maps than the broad-band maps. Other work (Koles and Paranjape, 1988) has given similar results: topographic maps of high frequency (13 to 30 Hz) EEG data were shown to have less precision than maps of low frequency EEG data (<13 Hz). Nuwar (1988a) supports these findings in a review of quantitative EEG methods and topographic mapping in which he states, "Preliminary investigations of spatial features have suggested that high temporal frequency bands (beta and alpha) have high rates of spatial phase change whereas low-frequency bands (eg. delta) have low rates of spatial phase change.".

Topographic maps of the rms value of the EEG calculated over 0.5 sec epochs showed that the rms value of the error was much smaller than that observed for instantaneous EEG maps. Thus, it appeared that maps as estimates of the rms potential distribution on the scalp were accurate and reasonably precise. The difference in accuracy and precision between broad-band and alpha-band rms EEG maps was small. However, the regression analysis of rms EEG data showed greater variability in slope and $r^2$ value for broad-band maps than for alpha-band maps. The alpha-band rms EEG maps were further investigated because the $\chi^2$ goodness-of-fit test indicated a high probability that samples from alpha-band maps were from the same population as samples from the actual potential distribution.

As all methods of interpolation performed similarly in this study, it might appear that little is to be gained by the use of more computationally expensive methods of interpolation such as bicubic-splines. A lack of sensitivity to interpolation method supports Duffy's (1978) observation that electrodes more distant than the nearest three known points have minimal influence on intermediate potentials. Bicubic-spline interpolations, however, do have a distinct advantage over other interpolations in that they provide an estimate of the radial current density. The radial current density on the scalp has been shown to be proportional to the curvature of the potential distribution (Nunez, 1981). Thus, by applying the Laplacian operator analytically to the functional form of the bicubic-spline surface an estimate of the radial current can be obtained (Koles *et al.*, 1989). The triangularly and bilinearly interpolated surfaces, on the other hand, lack the necessary curvature to allow estimations of the radial current density.

The second question examined in this work was: is the distribution of scalp potential, when decomposed into spatial waves on topographic maps, useful in the classification and characterization of the functional state of the brain. Various methods of spectral analysis were therefore investigated. J. G. Ables (1972) when writing about the spectral analysis stated: "The results of any transformation on experimental data shall incorporate and be consistent with all relevant data and shall be maximally non-committal with regard to unavailable data." . The maximum entropy (ME) method of power spectrum (PS) analysis may be viewed as an attempt to select the frequency domain representation of the data that is in closest possible accord with Ables' principle. The maximum entropy approach theoretically provides the best spectral estimate given the available information.

This result was experimentally confirmed through an analysis of power spectrum estimates (PSEs) of simulated EEG data. Using the Bartlett (BA), Blackman-Tukey (BT) and maximum entropy (ME) methods, PSEs of various sinusoidal spatial waves on a finite (5x5) grid were calculated. The ME method consistently produced better PSEs than the BA and BT methods, when compared in terms of the frequency range and the minimum separation in frequency required to distinguish two sinusoidal waves.

The ME method of PS analysis was then applied to data which contained sinusoidal waves and white noise. It showed that acceptable PSEs could be obtained if the signal-to-noise ratio (SNR) of the data was ≥0 dB. The conclusion from experimental and theoretical considerations are that ME PSEs can be used to characterize topographic maps of rms EEG if data is obtained on a regular grid and if it can be modelled as sinusoidal waves in low-amplitude white noise.

A experimental investigation was carried out to determine if rms EEG topographic maps contained systematic variations that were correlated to the functional state of the brain. EEG data was recorded from subjects resting with eyes closed (EC) and also from subjects resting with eyes open and fixed onto a single point (EO). Topographic maps produced from this data were used to calculated PSEs with the ME method. The ME PSEs were reduced to a set of feature vectors with each feature representing the change in the PSE from its mean value. Various statistical analyses were then carried out using the obtained features.

T-tests were applied to feature means and indicated that certain features were significantly different in the EC and the EO states. For example, the mean value of the A3 feature, relating to the power of spatial waves along the sagittal line, was significantly larger ($p < 0.01$) in the EC state than in the EO state. In general, it was observed that EC topographic maps contained signals of greater energy than did EO topographic maps.

The mean value of the entropy feature, E1, was significantly larger ($p < 0.01$) in the EO PSEs than in the EC PSEs. This indicated that EO PSEs were more uniform than EC PSEs. It further indicated that EO topographic maps were more complex than EC topographic maps. This is consistent with the expectation that when processing visual stimuli various regions of the brain become electrically more active than when the brain is purely in a resting state. The potential distributions associated with the active state are more complex than those associated with the resting state.

A discriminant analysis was performed with the features from the PSEs to determine if EC and EO states could be distinguished for individual cases. The discriminant function was calculated using 60% of the features from the PSEs and then applied to the remaining 40% to test the stability of the discrimination. The discriminant function, which contained only 4 features, predicted correctly over 96% of the subject's states in the test set. The features used in the discriminant function were A3, A6, A10 and E1. The A3 feature identified spatial waves at an orientation along the sagittal line with a wavelength of 18.67 cm on the topographic maps. The A6 and A10 features identified a wave oriented primarily along the lateral (left-right) line with a wavelength of 20.75 cm. The mean value of these features was greater in the EC state than in the EO state indicating that the waves have a larger amplitude in the EC topographic map. The E1 feature, the entropy of the PSE, was smaller in the EC PSEs than in the EO PSEs.

To determine if the results thus far obtained were due primarily to differences in the total energy in the maps a further analysis of normalized PSEs was performed. Through the normalization process the total power of spatial waves in the maps for each state was made a constant.

The t-test of feature means from the normalized PSEs indicated that certain features were significantly different between the two states. The features that identify waves in the sagittal direction had larger mean values in the EC state than in the EO state. The EO topographic map on the other hand, contained waves oriented in all directions.

A discriminant analysis of the features from the normalized PSEs showed that in over 92% of cases the state of the subject could be correctly identified in the test set. The features used in the discriminant function were A4, A7, A8 and A10. These features identified waves of various orientations in the topographic maps. A8, which identified a wave in the sagittal direction, was larger in the EC normalized PSEs while the remaining features (A4, A7, A10) which were oriented in other directions were larger in the EO normalized PSEs.

The analysis of features from normalized PSEs shows that not only is the difference in the EC and EO topographic maps characterized by change in the total energy of spatial waves in topographic maps, but also by a change in the spatial frequency content of the maps.

As the analysis of EEG topographic maps is still in its infancy, there are only a few methods to which spatial spectral analysis can be compared. The technique of classification by space constants of topographic maps containing spikes has been used by Matsuo and Gaskin (1986). The space constant is the spatial analogue of the more familiar time constant and indicates distance on the map for the amplitude of a spike falls off to 37% (1/e) of its maximum recorded value (Nuwar, 1988a). Matsuo and Gaskin have used measurements of the space constant to differentiate between superficial and deep spike-generating sources. A spectral analysis for differentiating between these sources would be based on the spatial frequency content in the maps. High spatial frequencies would correspond to rapid amplitude changes in the maps and would suggest superficial sources while lower spatial frequencies would suggest deeper sources.

A statistical method for analysis of topographic maps, made popular by Duffy *et. al.*, (1981), is probability significance mapping. In this method, topographic maps of z scores are formed which represent an individual's deviation away from the mean of a reference set. When z scores are greater than 2-3 a subject's EEG is considered out of the normal range of values. A modification on this approach, carried out to compare two populations, is to use a t-test to identify the regions on maps that differ significantly from one population to the other. This approach is similar to that used in this thesis where t-tests were used to compare regions of spatial PSEs. In this thesis the power of spatial waves on the maps was compared rather than simply map amplitudes.

## 6.2 Further Investigations

This work raises a number of interesting questions that should be investigated further. These questions focus on two areas of EEG research: (1) the physical characteristics of the space-time distribution of scalp potentials, and (2) the relationship between the spatial distribution of scalp potentials and brain function.

The controversy about the density of the sampling electrodes required to adequately sample the spatial distribution of potential on the scalp is not fully resolved by this work. A simple approach to this problem might be as follows. Apply a dense rectangular electrode array to a small region of the scalp and record scalp potentials. If the inter-electrode distance in the recording array is sufficiently small, the 2-dimensional Fourier transform of the recorded data will have relatively low amplitude components at the folding frequency. The inter-electrode distance should then be increased slightly and the 2-dimensional Fourier transform calculated again. If the basic shape of the Fourier transform is not changed, it would indicate that the scalp potential has been adequately sampled in the region of the electrode array.

The approach described above raises the further question of whether the spatial frequency characteristics of the scalp potentials are spatially invariant. This can be determined simply by moving the electrode array to various regions of the scalp and repeating the above procedure.

The results of Chapter 2 indicate that there is a relationship between the spatial and the temporal frequencies of the EEG. It was shown that the precision of topographic maps increased when the temporal frequency of the EEG was restricted to a narrow temporal frequency band. A further investigation of this spatio-temporal relationship is warranted. The methods described in Chapter 2 could be adopted for this investigation. The temporal frequency of the EEG could be restricted to a narrow band and the accuracy and the precision of interpolated maps could be determined. Through an analysis of a series of maps constructed from EEG data filtered into a number of narrow temporal frequency bands, the spatio-temporal relationship could be more completely described.

Another approach to determining the spatio-temporal relationship of the EEG would involve 3-dimensional (space-time) Fourier analysis. The 3-dimensional Fourier transform of EEG data varying in both space and time would indicate the existence of standing spatial waves and travelling spatial waves on the scalp. By observing the effect of temporal filtering on the coefficients of spatial waves a correlation between these domains could be demonstrated.

This thesis indicates that there is a relationship between the distribution of scalp potential and the functional state of the brain. This result implies that the distribution of scalp potential may be useful in the analysis of brain function and pathology. It would be very interesting to determine whether brain states other than EC and EO could be distinguished by spatial patterns. For example, specific patterns may be associated with subjects listening to music or solving mental arithmetic problems. Similarly, in the study of brain pathology, recurring phenomena such as migraine may be characterized by particular spatial patterns. Various drugs, such as halothane (Nunez, 1981), have been shown to induce marked changes in the temporal pattern of the EEG; similar effects may occur in the spatial patterns.

### 6.3 Some Observations on Topographic Mapping

Many researchers are interested in determining correlations between topographic maps and brain function and pathology. As indicated in Chapter 1, these efforts have had only limited success. There may be a number of contributing factors.

(1) Sufficient attention must be given to the projection of scalp potentials to the flat map. In this thesis the Mercator method of projection was used. This is a simple method of projection but has the advantage of being conformal so that angles and directions are preserved through the projection. Recently work has begun in which spherical harmonic functions are used in interpolations. More consistent results may be expected with this approach because it better approximates the true geometry of the head.

(2) The level of error in the maps must be known. In Chapter 2 it was shown that all electric potentials on the scalp are not mapped with equal error. It was shown that the error was dependent on the electrode density and on the temporal frequency content of the

signals to be mapped. In this thesis rms alpha-band EEG data was used after analysis of error levels.

(3) A systematic approach to classification of spatial patterns is required. In this thesis, the approach adopted was to summarize maps in terms of sinusoidal spatial waves. These waves are easy to visualize and can be defined precisely with a small number of parameters.

(4) Since the brain responds to a wide variety of stimuli, the analysis should be highly focused so that variation due only to appropriate factors are considered.

### 6.4 Conclusions and Limitations

The following conclusions from this work are observed.

(1) Broad-band instantaneous EEG topographic maps as estimates of the actual potential distribution have a low bias but have a large variance.

(2) Alpha-band instantaneous EEG topographic maps have a low bias and have a smaller variance than broad-band EEG maps.

(3) Rms EEG topographic maps have low bias and low variance.

(4) There is a relationship between the temporal frequency and the spatial frequency of the EEG. By restricting the temporal frequency to a narrow band the spatial frequency is also restricted.

(5) The method of interpolation does not significantly affect the error in EEG topographic maps.

(6) The ME method of PS analysis consistently produces better PSEs than the BA or the BT methods in terms of frequency range and minimum separation in frequency required for identification of two sinusoidal waves.

(7) In simulations that model analysis of EEG topographic maps, ME PS analysis can be used to characterize sinusoidal waves in white noise if the SNR ≥0 dB.

(8) Rms EEG topographic maps have significant changes that are correlated to the functional state of the brain.

(9) From the study of spatial ME PSEs of EEG topographic maps from normal volunteers in EC and EO states the following is observed.

  (a) EC topographic maps contain spatial waves of greater energy than do EO topographic maps.

  (b) The entropy of EO PSE is greater than that of EC PSEs indicating EO topographic maps are more complex than EC topographic maps.

  (c) EC topographic maps contain a greater proportion of waves oriented in the sagittal direction than do EO topographic maps.

  (d) A discriminant function can correctly classify the state associated with about 96% of the observations from PSEs in test data.

  (e) A discriminant function can correctly classify the state associated with about 92% of the observations from normalized PSEs in test data.

(10) The methodology of topographical analysis of EEG data is verified and further analysis of topographic maps with spatial PS analysis is warranted.

The following limitations of this work are observed.

(1) There is a loss of information associated with the representation of the continuous distribution of potential on the scalp by a discrete sequence.

(2) There is a loss of information associated with representing data by PSEs.

(3) The model of a limited number of spatial sinusoidal waves in low-amplitude, white noise must be appropriate in order that the results of spatial PS analysis to be meaningful in the characterization of the potential distribution on the scalp.

# References

Ables J.G., Maximum entropy spectral analysis, Astronomy and Astrophysics Supplemental Series, 15:383-393, 1974.

Alberts B., Bray D., Lewis J., Raff M., Roberts K., Waston J.D., Molecular biology of the cell, Garland, New York, USA., p. 1105, 1983.

Andrews H.C., Hunt B.R., Digital image restoration, Englewood Cliffs, New Jersey,, Prentice Hall, p. 90-112, 1977.

Baggeroer A.B., Sonar signal processing, in Applications of Digital Signal Processing, Oppenhiem (ed), Englewood Cliffs, New Jersey, Prentice Hall, p. 331-228, 1978.

Berger H., Hans Berger on the electroencephalogram of man, translated by Gloor P., Electroencephalography and Clinical Neurophysiology, Supplemental 28, 2825, 1986.

Burg J.P., Maximum entropy spectral analysis, Proceedings of the 37th Meeting of the Exploration Geophysicists, Oklahoma City, USA., 1967.

Clark D.L., Rosner B.S., Neurophysiologic effects of general anesthetics. I. The electroencephalogram and sensory evoked responses in man, Anesthesiology, 38:584, 1973.

Doyle J., Ornstein R., Galin D., Lateral specialization of cognitive mode. II. EEG frequency analysis, Psychophysiology, 11(5):567, 1974.

Dudgeon D.E., Mersereau R.M., Multidimensional signal processing, Prentice Hall, Englewood Cliffs, New Jersey, USA., 1984.

Duffy F.H., Burchfield J.L., Lombroso C.T., Brain electrical activity mapping (BEAM): A method for extending the clinical utility of EEG and evoked potential data, Annals of Neurology, 5(4):309-321, 1978.

Duffy F.H., Bartels P.H., Burchfield J.L., Significance probability mapping: An aid in the topographic analysis of brain electrical activity, Electroencephalography and Clinical Neurophysiology, 51:455-462, 1981.

Duffy F.H., Topographic display of evoked potentials: Clinical applications of brain electrical activity mapping, Annals of the New York Academy of Science, 388:183-196, 1982.

Duffy F.H., Topographic mapping of brain electrical activity, Butterworth, Stoneham, USA., 1968.

Fisher R.A., The use of multiple measurements in taxonomic problems, The Annals of Eugenics, 7:179-188, 1936.

Gevins A.S., Zeitlin G., Yingling C., Doyle J., Dedon M., Henderson J., Schaffer R., Roumasset J., Yeager, C., EEG patterns during "cognitive" tasks. I.

Methodology and analysis of complex behaviors, Electroencephalography and Clinical Neurology, 47(5), 1979.

Gevins A.S., Schaffer R.E., A critical review of electroencephalographic (EEG) correlates of higher cortical functions, CRC Critical Reviews in Bioengineering, (Oct):113-164, 1980.

Gevins A.S., Analysis of electromagnetic signals of the human brain: Milestones, obstacles, and goals, IEEE Transactions on Biomedical Engineering, 31(12):833-850, 1984.

Gibbs F.A., Davis H., Lennox W.G., Electroencephalogram in epilepsy and in conditions of impaired consciousness, Archives of Neurological Psychiatry, 34:1133, 1935.

Gibbs F.A., Gibbs E.L., Neurological and psychiatric disorders, Atlas of Electroencephalography, Vol 3, Addison-Wesley, Reading, USA., 1964.

Gloor P., Neuronal generators and the problem of localization in electroencephalography: Application of volume conductor theory to electroencephalography, Journal of Clinical Neurophysiology, 2(4):327-354, 1985.

Harris J.A., Bickford R.G., Spatial Display and Parameter Computation of the Human Epileptic Spike Focus by Computer, Electroencephalography and Clinical Neurophysiology, 24:281-294, 1968.

Harvard Committee on Brain Death, A definition of irreversible coma. Report of the Ad Hoc Committee of the Harvard Medical School of examining the definition of brain death, Journal of the American Medical Association, 205:307, 1968.

Haykin S., Introduction, Nonlinear Methods of Spectral Analysis, Haykin S. (ed), Topics in Applied Physics, 34:1-8, 1983.

Haykin S., Kesler S., Prediction-error filtering and maximum entropy spectral estimation, Nonlinear Methods of Spectral Analysis, Haykin S. (ed), Topics in Applied Physics, 34:9-70, 1983.

Hoel P.G., Introduction to mathematical statistics, John Wiley, New York, 1971.

Jaynes E.T., Physical Review, 106:620, 1957.

Jaynes E.T., Probability theory in science and engineering, Colloquium Lectures in Pure and Applied Science, No. 4, SOCONY Mobil Oil Co., 1958.

Jaynes E.T., On the rationale of maximum entropy methods, Proceeding of the IEEE, 70(9):939-952, 1982.

Jaynes E.T., Papers on probability, statistics and statistical physics, a collection of reprints, Dordrecht, The Netherlands, D. Reidel, 1982.

Jenkins G.M., Watt D.G., Spectral analysis and its applications, Holden-Day, San Francisco, USA., 1968.

Jonkman E.J., Poortvliet D.C.J., Veering M.M., De Weerd A.W., John E.R., The use of neurometrics in the study of patients with cerebral ischemia, Electroencephalography and Clinical Neurophysiology, 61:333-341, 1985.

Katada A., Ozaki H., Suzuki H., Suhara K., Developmental characteristics of normal and mentally retarded children's EEG, Electroencephalography and Clinical Neurophysiology, 52:192-201, 1981.

Katznelson R.D., Normal modes of the brain: Neuroanatomical basis and a physiological theoretical model, Electric Fields of the Brain, Nunez P.L. (ed), Oxford University Press, London, UK., 1981.

Koles Z.J., A general purpose physiological-data acquisition system for medical research, Proceedings of Third Mediterranean Conference on Medical and Biological Engineering, Yugoslavia, p. 9.1, Sept 5-98, 1983.

Koles Z.J., Paranjape R.B., Topographic mapping of the EEG: An examination of accuracy and precision, Brain Topography, 1(2):87-95, 1988.

Koles Z.J., Kasmia A., Paranjape R.B., McLean D.R., Computed radial-current topography of the brain: Patterns associated with the normal and the abnormal EEG, Electroencephalography and Clinical Neurophysiology, 72:41-47, 1989.

Kooi K.A., Fundamentals of electroencephalography, Harper Row, New York, USA., 1971.

Koukkou M., Lehmann D., Angst J., Functional states of the brain: Their determinants, Elsevier, Amsterdam, 1980.

Lehmann D., Multichannel topography of human alpha EEG fields, Electroencephalography and Clinical Neurophysiology, 31:439-449, 1971.

Lehmann D., Human scalp EEG fields: Evoked, alpha, sleep and spike wave patterns, Synchronization of EEG Activity in Epilepsies, Petsche H., Brazier M.A.B. (ed), p. 307-326, 1972.

Lehmann D., Skrandies W., Reference-free identification of components of checkerboard-evoked multichannel potential fields, 48:609-628, 1980.

Lehmann D., Principles of spatial analysis, Handbook of Electroencephalography and Clinical Neurophysiology, Gevins A. S. (ed), Elsevier Science Publishers, Amsterdam, p. 309-354, 1987.

Lehmann D., Ozaki H., Pal I., Averaging of spectral power and phase via vector diagram best fits without reference electrode or reference channel, Electroencephalography and Clinical Neurophysiology, 64:350-363, 1986.

Lehmann D., Ozaki H., Pal I., EEG alpha map series: Brain micro-states by spatio-oriented adaptive segmentation, Electroencephalography and Clinical Neurophysiology, 67:271-288, 1987.

Lim J.S., Malik N.A., A new algorithm for two-dimensional maximum entropy power spectrum estimation, IEEE transactions on Acoustics, Speech and Signal Processing, 29(3):401-413, 1981.

Lim J.S., Malik N.A., A new algorithm for one-dimensional and two-dimensional maximum entropy power spectrum estimation, IEEE Conference on Acoustics, Speech and Signal Processing, March 30, 31, April 1, Atlanta, Georgia,1981.

Malik N.A., Lim J.S., Glaser M.J., Properties of Two Dimensional Maximum Entropy Power Spectrum Estimates, IEEE Conference on Acoustics, Speech and Signal Processing, May 2-4, Paris France, 1982.

Matsuo F., Gaskin J.A., Scalp field gradients of focal epileptiform transients, Epilepsia, 27:641, 1986.

McDonough R.N., Application of the maximum-likelihood method and the maximum entropy method to array processing, Nonlinear Methods of Spectral Analysis, Haykin S. (ed), Topics in Applied Physics, 34:181-243, 1983.

Naitoh P., Walter D.O., Simple Manual Plotting of Contours as a Means of EEG Analysis, Electroencephalography and Clinical Neurophysiology, 26:424-428, 1969.

Narayan R., Nityananda R., Maximum entropy - flexibility versus fundamentalism, Indirect Imaging, Proceedings of an International Symposium by International Union of Radio Science and International Astronomical Union, 2 Sept. 1983, Sydney Australia, Cambridge University Press, 1984.

Nunez P.L., Electric Fields of the Brain, Oxford University Press, London, UK., 1981.

Nuwar M.R., Quantitative EEG: I. Techniques and problems of frequency analysis and topographic mapping, Journal of Clinical Neurophysiology, 5(1):1-43, 1988a.

Nuwar M.R., Quantitative EEG: II. Frequency analysis and topographic mapping in a clinical setting, Journal of Clinical Neurophysiology, 5(1):44-85, 1988b.

Oppenheim A.V., Schafer R.W., Digital signal processing, Prentice Hall, Englewood Cliffs, New Jersey, USA., 1975.

Paranjape R.B., Koles Z.J., On the accuracy and precision of topographic maps of the EEG, Proceedings of the 12th Canadian Medical and Biological Engineering Conference, Vancouver, Canada, 1986.

Perrin F., Perinier J., Bertrand O., Giard M.H., Echallier J.F., Mapping of scalp potentials by surface spline interpolation, Electroencephalography and Clinical Neurophysiology, 66:75-81, 1987.

Prier S., Beniot C., Redondo A., Resultat de la cartographic EEG au cour des tumeurs cerebrales configuation aux methodes d'imagerie, Electroencephalograpy and Clinical Neurophysiology, 16:257-267 1986.

Raisz E., General cartography, McGraw Hill, New York, USA., 1948.

Remond A., Cardiac and vascular disease, Handbook of Electroencephalography and Clinical Neurology, 14 (Part A),Van Der Drift J.H.A. (ed), Elsevier, Amsterdam, 1972a.

Remond A., Hereditary, congenital and perinatal diseases, Handbook of Electroencephalography and Clinical Neurology, 15 (Part B), Dreyfus-Brisac C., Ellingson R.J. (ed), Elsevier, Amsterdam, 1972b.

Robinson E.A., A historical perspective of spectrum estimation, Proceedings of the IEEE, 70(9):885-907, 1982.

Spath H., Splines algorithms for curves and surfaces, Utilitas Mathematica, Winnipeg, Canada, 1974.

Shipton H.W., EEG analysis: A history and a prospectus, Annual Review of Biophysics and Bioengineering, 4:1-13, 1975.

Takahashi H., Yasue M., Ishijima B., Dynamic EEG topography and analysis of epileptic spikes and evoked potentials following thalamic stimulation, Applied Neurophysiology, 48:418-422, 1985.

Ulrych T.J., Ooe M., Autoregressive and mixed autoregressive - moving average models and spectra, Nonlinear Methods of Spectral Analysis, Haykin S. (ed), Topics in Applied Physics, Springer Verlag, Berlin W. Germany, 34:73-126, 1983.

Ulrych T.J., Bishop T.N., Maximum entropy spectral analysis and autoregressive decomposition, Reviews in Geophysics and Space Physics, 13:183-200, 1975.

Vogel W., Broverman D.M., Klaiber E.L., EEG and mental activity, Electroencephalography and Clinical Neurology, 24:166, 1968.

Walter D.O., Rhodes, J.M., Adey W.R., Discrimination among states of consciousness by EEG measurements; a study of four subject, Electroencephalography and Clinical Neurology, 22:22, 1967.

Walter W.G., Shipton H.W., A new toposcope display system, Electroencephalography and Clinical Neurology, 3:281-292, 1951.

Walter W.G., The location of cerebral tumors by electroencephalography, Lancet, 2:305, 1936.

Wold H., A study in the analysis of stationary time series, Almquist and Wiksell, Uppsala, 1938.

Wong P.K.K., Gregory D., Bencivenga R., Farrel K., Typical and Atypical Benign Rolandic Epilepsy: Statistical Analysis of Spike Maps, Epilepsia, (27):641, 1986.

Woods J.W., Two-dimensional Markov spectral estimation, IEEE Transactions on Information Theory, 22(5):552-559 1976.

# APPENDIX 'A'

## The Blue Eyed Left Handed Kangaroo Problem

To give some idea of how the ME method can be used in general, a simple problem of probability estimation is considered. The solution to the problem is intuitive and can be easily guessed. This problem was originally proposed by Gull and Skilling (1984) although a complete solution was not provided.

Consider that a visitor to the Australian subcontinent is told the following information about the marsupial wildlife.

(1) 1/3 of all kangaroos are blue eyed.

(2) 1/3 of all kangaroos are left handed.

Then, he is asked the question: What is the probability that a kangaroo drawn at random from the population is both blue eyed and left handed? The visitor, after thinking a minute, would likely answer there is a 1/9 probability that the kangaroo is both blue eyed and left handed.

This answer is somehow intuitively appealing but in fact it is making a rather large statement about the wildlife of Australia. That is, that blue eyes and left handedness are not related in anyway. Having blue eyes for instance neither increases nor decreases the probability that a kangaroo is left handed. This answer is based on the principle that if no relationship is stated explicitly between variables then it is best to assume that no relationship exists between them. This is exactly the ME principle.

In order to apply the ME method to this problem it must be restated in a more mathematical form. The probability distribution function (PDF) can be presented in a tabular form.

|  |  | Blue Eyes T | Blue Eyes F |
|---|---|---|---|
| Left Handed | T | p1 | p2 |
|  | F | p3 | p4 |

$p_1$ is the probability that the kangaroo drawn at random is both blued eyed and left handed. The sum of all the probabilities is one.

(A.1)

$$p_1+p_2+p_3+p_4 = 1$$

The other information about the marsupial wild life can be written in terms of:

(A.2)

$$p_1+ p_2 = 1/3$$

$$p_1+ p_3 = 1/3$$

The entropy of the PDF is defined in the conventional form;

(A.3)

$$H= -\Sigma p_i \ln (p_i)$$

The object is to determine $p_1$. The entropy of the PDF is maximized by using the method of Lagrange multipliers.

(A.4)

$$H = -\sum_{i=1}^{4} p_i \ln(p_i) +\lambda_0(p_1+p_2+p_3+p_4 -1) +\lambda_1(p_1+p_2-\frac{1}{3}) +\lambda_2(p_1+p_3-\frac{1}{3})$$

and set

$$\partial H/\partial(p_i) = 0$$

A system of equations is formed.

(A.5)

$$\partial H/\partial p_1 = 0 = -\ln(p_1) - 1 + \lambda_0 + \lambda_1 + \lambda_2$$

$$\partial H/\partial p_2 = 0 = -\ln(p_2) - 1 + \lambda_0 + \lambda_1$$

$$\partial H/\partial p_3 = 0 = -\ln(p_3) - 1 + \lambda_0 + \lambda_2$$

$$\partial H/\partial p_4 = 0 = -\ln(p_4) - 1 + \lambda_0$$

There are now seven equations and seven unknowns.

(A.6)

(a) $p_4 = \exp(-1 + \lambda_0)$

(b) $p_3 = \exp(-1 + \lambda_0 + \lambda_2) = p_4 \exp(\lambda_2)$

(c) $p_2 = \exp(-1 + \lambda_0 + \lambda_1) = p_4 \exp(\lambda_1)$

(d) $p_1 = \exp(-1 + \lambda_0 + \lambda_1 + \lambda_2) = p_4 \exp(\lambda_1 + \lambda_2)$

(e) $p_1 + p_2 + p_3 + p_4 = 1$

(f) $p_1 + p_2 = 1/3$

(g) $p_1 + p_3 = 1/3$

From (A.6.f) and (A.6.g), and from (A.6.b) and (A.6.c),

(A.7)

$$p_1 + p_2 = 1/3 = p_1 + p_3 \qquad \Rightarrow p_3 = p_2$$

$$p_2 = p_4 \exp(\lambda_1) = p_3 = p_4 \exp(\lambda_2) \qquad \Rightarrow \lambda_2 = \lambda_1$$

Now using only $p_2$ and $\lambda_1$ in (A.6.e):

$$p_1 + 2p_2 + p_4 = 1$$

and (A.6.c) and (A.6.d) become:

$$p_2 = p_4 \exp(\lambda_1) \qquad \Rightarrow p_4 = p_2 \exp(-\lambda_1)$$

$$p_1 = p_4 \exp(2\lambda_1) \qquad \Rightarrow p_1 = p_2 \exp(\lambda_1)$$

Now substituting for $p_1$ into (A.6.g):

$$p_1 + p_2 = 1/3$$

$$p_2 \exp(\lambda_1) + p_2 = p_2 (\exp(\lambda_1) + 1) = 1/3$$

$$\Rightarrow (\exp(\lambda_1) + 1) = 1/(3p_2)$$

$$\Rightarrow \exp(\lambda_1) = -1 + 1/(3p_2) = (-3p_2 + 1) / (3p_2)$$

$$\Rightarrow \exp(-\lambda_1) = (3p_2) / (-3p_2 + 1)$$

Substituting into (A.7) for $p_1$ and $p_4$,

(A.8)

$$p_1 + 2p_2 + p_4 = 1$$

$$p_2 \exp(\lambda_1) + 2p_2 + p_2 \exp(-\lambda_1) = 1$$

$$p_2 \exp(-\lambda_1) (\exp(\lambda_1) + 1)^2 = 1$$

Substituting from above for $(\exp(\lambda_1) + 1)$.

$$p_2 \exp(-\lambda_1) (1/(3p_2))^2 = 1$$

$$(\exp(-\lambda_1))/(9p_2) = 1$$

Substituting from above for $\exp(-\lambda_1)$.

$$(3p_2) / ((-3p_2 + 1)(9p_2)) = 1/(-9p_2 + 3) = 1$$

$$-9p_2 + 3 = 1$$

$$p_2 = 2/9$$

therefore

(A.9)

$$p_1 = 1/9 \quad p_2 = 2/9 \quad p_3 = 2/9 \quad p_4 = 4/9$$

The significant result is;

$$p_1 = 1/9 = 0.1111$$

The ME solution of this problem is coincidental with the intuitive solution. The ME PDF is a smooth and maximally flat while remaining within the constraints of the problem.

# APPENDIX 'B'

## Forms of The Entropy Function

There is some question as to the validity of the various forms of entropy of a signal. This appendix outlines the approach to this problem presented by Narayan and Nityananda (1984). This issue is best dealt with by not assigning any meaning to the entropy function. In this section as the entropy function is presented simply as f, thus the detailed form of the entropy function is hidden. H, the total entropy of the signal B(x) is then define as:

(B.1)

$$H = \int f(B(x))\, dx$$

Let us assume that $B(x)_O$ is a recorded signal and is band limited. $B(x)_O$ is to be the basis of an estimate of the true signal B(x). Because $B(x)_O$ is band limited the fine details in B(x), can not be seen in $B(x)_O$. The FT of $B(x)_O$ is assumed to be identical to that of B(x) until some frequency $f_a$, which is less than the highest frequency in B(x) and is zero for frequencies greater than $f_a$. Another way to state this is, the band limited nature of $B(x)_O$ means that there is an abrupt discontinuity in the FT of $B(x)_O$ and this discontinuity results in ringing and the overshadowing of low amplitude details of B(x) in $B(x)_O$.

B(x) can be estimated from $B(x)_O$ using the maximum entropy (ME) principle. The ME estimate of B(x) is called $B(x)_e$. Frequency coefficients which are greater than $f_a$ are found in $B(x)_e$. The basic procedure to maximize the entropy of $B(x)_e$, $H_e$, is to find $\partial H_e / \partial \rho_{m \notin k}$ and set it equal to zero (where $H_e$ is the entropy of the $B(x)_e$ and $\rho_{m \notin k}$ are the unknown Fourier coefficients of $B(x)_e$). The coefficients $\rho_{m \notin k}$ can then be determined.

This is done as follows:

(B.2)

$$B(x)_0 = \sum_{m \in k} \rho_m \exp(2\pi j m)$$

$$B(x)_e = \sum_{m \in k} \rho_m \exp(2\pi j m) + \sum_{m \notin k} \rho_m \exp(2\pi j m)$$

$$H_e = \int f(B(x)_e)\, dx$$

$$H_e = \int f\left[ \sum_{m \notin k} \rho_m \exp(2\pi j m) + \sum_{m \in k} \rho_m \exp(2\pi j m) \right] dx$$

Note that $\rho_{m \in k}$ are the known frequency coefficients of $B(x)_0$.

To find the $\rho_{m \notin k}$ terms:

(B.3)

$$\frac{\partial}{\partial \rho_{m \notin k}} \left[ \int f\left[ \sum_{m \notin k} \rho_m \exp(2\pi j m) + \sum_{m \in k} \rho_m \exp(2\pi j m) \right] dx \right] = 0$$

(B.4)

$$\int f'(B(x)_e) \exp(2\pi j m)\, dx = 0 \quad \text{for } m \notin k$$

This equation implies that the function $f'(B(x)_e)$ is a band limited function. This is because equation (B.4) can be interpreted as the FT of $f'(B(x)_e)$, and it is equal to zero for $m \notin k$.

The band limited function $f'(B(x)_e)$ is called $G(x)$. $f'$ can then be viewed as a mapping between $B(x)_e$ and $G(x)$ as shown in figure B.1. If this mapping is linear then $B(x)_e$ will be band limited as is $G(x)$. However, if this mapping is non-linear then $B(x)_e$ is not band limited.

The graph of $f'$ versus $B_e$ shown in figure B.1 is such that high ripples in $G(x)$ are attenuated in $B_e$ while broad troughs in $G(x)$ are transformed into sharp peaks. To follow the mapping in detail, consider first the lower-right-hand graph. This graph shows the relationship between $B(x)_e$ and x. For a particular x, say $x^*$ there is a value of $B(x)_e$, called $B(x^*)_e$. From this $B(x^*)_e$ a value of $G(x^*)$ can be determine by moving up to the f' function and then across to the upper-left-hand graph, of the G(x) function.

When using the ME method to estimate $B(x)_e$ these graphs are followed in the opposite direction. The function G(x) is generated by the application of constraints and maximizing the entropy function. Then by moving in the opposite direction to that just shown, the new function $B(x)_e$ can be estimated. In other words, in an application of the ME method, a band limited G(x) plot is first produced and then the $B(x)_e$ function is produced. The transformation from G(x) (band limited) to $B(x)_e$ (non-band limited), is non-linear, and results in high frequency variations in $B(x)_e$.

Now, the critical point in this set of graphs is, it is suggested by Narayan and Nityananda (1984), the transformation using the non-linear profile of $f'(B(x)_e)$ versus $B(x)_e$. Any function with a similar profile, they maintain, can be considered an entropy function. Thus any function f, whose derivative f', has the form of the function shown in the upper-right-hand graph can be used to produce a high frequency content $B(x)_e$ from $B(x)_O$. For example, any of the functions -pln(p), ln(p), $p^{-1/2}$, $p^{-2}$ can serve as the entropy function. Narayan and Nityananda (1984) suggest the choice of the entropy function be based on the application.

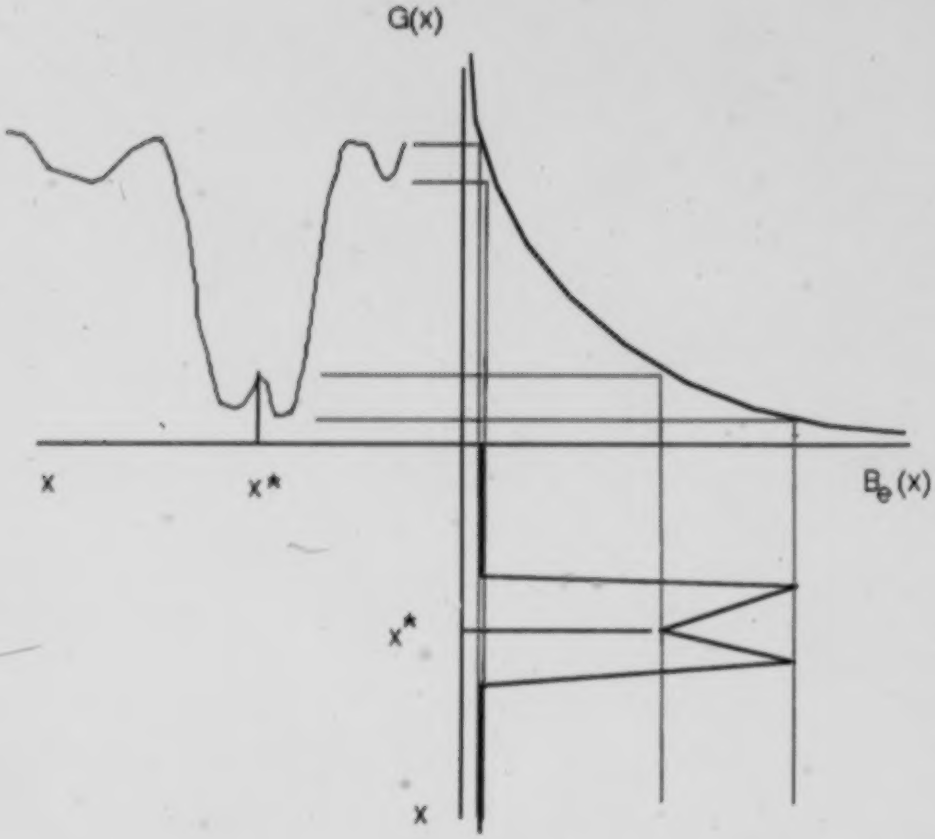

Figure B.1 Non-linear mapping between $B(x)_e$ and G(x).